ON THE NATURE OF WINTERTIME PRECIPITATION IN THE ALPINE REGIONS OF SOUTH-EASTERN AUSTRALIA

by

THOMAS H. CHUBB

A Dissertation Submitted in

Fulfillment of the

Requirements for the Degree of

DOCTOR OF PHILOSOPHY

in

MATHEMATICAL SCIENCES GENERAL

at

The School of Mathematical Sciences

Monash University, Victoria

Australia

July 2011

NOTICE 1

NOTICE 2

Contents

List of Tables

List of Figures

Abstract

Data from a precipitation gauge network in the Snowy Mountains of South-Eastern Australia has been analysed to produce a new climatology of wintertime precipitation and airmass history for the region in the period 1990–2009. Precipitation amounts on the western slopes and in the high elevations (> 1000 m) of the Snowy Mountains region have experienced a decline in precipitation of 19% for annual precipitation, and for wintertime precipitation the amount is about 22%, which is far greater than the decline experienced generally in south-eastern Australia during this period. The contrast in the decline east and west of the ranges suggests that factors influencing orographic precipitation are of particular importance.

A synoptic decomposition of precipitation events has been performed, which demonstrates that about 57% of the wintertime precipitation may be attributed to storms associated with "cut-off lows" (equatorward of 45° S). A further 40% was found to be due to "embedded lows", with the remainder due to Australian east coast lows and several other sporadically occurring events. The declining trend in wintertime precipitation over the past two decades is most clearly seen in the intensity of precipitation due to cut-off lows, and coincides with a decline in the number of systems associated with a cold frontal passage.

Closer investigation of two typical wintertime storms in the nearby Brindabella ranges, using weather station and remotely-sensed data, reveals that the post-frontal period is characterised by shallow, supercooled, orographically forced cloud and sustained, low to moderate precipitation rates. High resolution numerical simulations with the WRF model match the observations remarkably well and have been used to provide a more complete picture of the nature of these storms.

The transport of moisture to the Snowy Mountains during precipitation is investigated by coupling back trajectories with precipitation observations. Two principal "moisture corridors" are revealed, with the most frequent precipitation associated with westerly trajectories and orographic forcing, while heavy precipitation is associated with synoptic ascent ahead of a cold front, whereby trajectories are shown to come from the north.

Finally, a method is proposed to directly evaluate claims that precipitation in the Snowy Mountains has been suppressed by pollution from urban and industrial sources. Back tra-

jectories are used to provide a meteorological link between suspected pollution sources and a Snowy Mountains analysis region, and both satellite-derived cloud microphysics and surface precipitation observations are considered. It is shown that, while there is a clear link between the microphysics observations and surface precipitation rates, no convincing relationship exists between any of the pollution sources and Snowy Mountains cloud or precipitation observations.

Acknowledgements

I would firstly like to thank my supervisors, Steven Siems and Michael Manton for the guidance, enthusiasm, encouragement and support during my candidature. This thesis certainly wouldn't have been possible without their insightful comments and suggestions along the way. Thanks also to Anthony Morrison and Simon Caine, my friends and colleagues, who are also co-authors on chapter 4 of this thesis.

The material presented in this thesis was, in parts, made possible only by the dedicated work of the team at Snowy Hydro, who also provided funding for the project. I thank John Denholm, Loredana Warren, Shane Bilish, Andrew Peace, Suzeanne Kenyon, Karen Kemsley, Gerald Rampart, Phil Boreham and Amanda Johnson for the role they have each played.

Ian Hampton and Warren King encouraged us to look into precipitation in the Brindabella ranges, which was an interesting and fulfilling project. Melanie Wetzel provided support and quality control for the radiometer data used in this thesis.

Thanks also go to my friends and colleagues at Monash University, Melbourne University, the Bureau of Meteorology and CSIRO, to many to name here, all of who have provided support, both technically and socially, during my candidature.

My friends and family have been a constant source of love and support, always encouraging and never doubting. This thesis is dedicated to you.

And finally, mostly of all, my best friend and life partner, Greta. You amaze and delight me more each day. Thank you for sharing the good times, and for putting up with me during the hard times.

Chapter 1

Introduction

Management of worldwide water resources is bound to become one of the major challenges to policy makers of the twenty-first century. Access to clean water for drinking, agriculture and industry has been taken for granted in developed nations for many years, but the limitations of water supplies have begun to become apparent. In south-eastern Australia, for example, the overallocation of water supplies in the Murray-Darling Basin (MDB) has resulted in a host of environmental and ecological crises ranging from soil salinity to river and wetland ecosystem degradation. Future water management policy faces the difficult task of reconciling the needs of present and future users with projected changes in average annual precipitation.

Wintertime storms play a crucial role in the hydrological cycle for mid-latitude regions like the MDB. Precipitation from these storms is needed for cool-season cereal crops and pasture, and provides water storage in the form of reservoir inflow, and in higher elevations, winter snowpack. Irrigation is dependant on good water management, and further understanding of the nature of wintertime storms is important to future water management efforts.

Understanding of wintertime precipitation in mountainous regions is central to water resources management in the MDB. The Great Dividing Range (GDR), which runs along the entire eastern seaboard of the Australian continent, forms the headwaters of all of the major rivers in this agricultural "breadbasket". Annual precipitation amounts are up to four times greater in these uplifted regions compared with the lower lying plains to the west, and the majority of this precipitation occurs in the cooler months of May-September. A decline of about 15% in cool season precipitation in southern Australia since 1958 has been observed

(Nicholls, 2010), and links with sea-level pressure changes have been established (Larsen and Nicholls, 2009), but the impact on alpine precipitation has not been specifically investigated.

This thesis considers the nature of alpine wintertime precipitation in the Australian Snowy Mountains region, where the sources of the Murray and Murrumbidgee rivers are located. The decline in precipitation during the recent drought years of 1997 to 2009 is placed in the context of a 20 year rainfall climatology of the Snowy Mountains in Chapter 2, with focus given to the relationship between elevation and precipitation decline. Chapter 3 presents a synoptic climatology of precipitation events between 1990 and 2009, examining the variability and trends in both the number of events and the contribution to the total wintertime precipitation relative contribution of the two major types identified. Chapter 4 of this thesis presents a comprehensive analysis of two wintertime precipitation events in the alpine region just to the north of the Snowy Mountains, using surface-based microwave radiometer and multi-spectral satellite data to validate numerical simulations of cloud properties.

The final two chapters of this thesis involve the use of meteorological trajectories to represent the history of the airmass during precipitation in the Snowy Mountains. Chapter 5 is a climatology of wintertime back trajectories which focuses on the transport of moisture for precipitation in the mountains. The final chapter of this thesis describes the use of back trajectories to address recently-voiced concerns that precipitation amounts in the Snowy Mountains are prone to suppression from urban and industrial pollution.

1.1 The importance of alpine regions to water resources

The Murray-Darling Basin is the large inland river basin to the west of the GDR in south-eastern Australia (figure 1.1). Named for the two major river systems it contains, it drains more than one million square kilometres, or almost 14% of the Australian continent, and covers significant regions in New South Wales, Victoria, South Australia, Queensland and the Australian Capital Territory.

Most of the region is low-lying, flat terrain in the interior of the continent, and generally receives low annual rainfall amounts. In spite of this, it is enormously important for Australian agriculture, generating 39% of national agricultural revenue (ABS, 2008). Irrigated

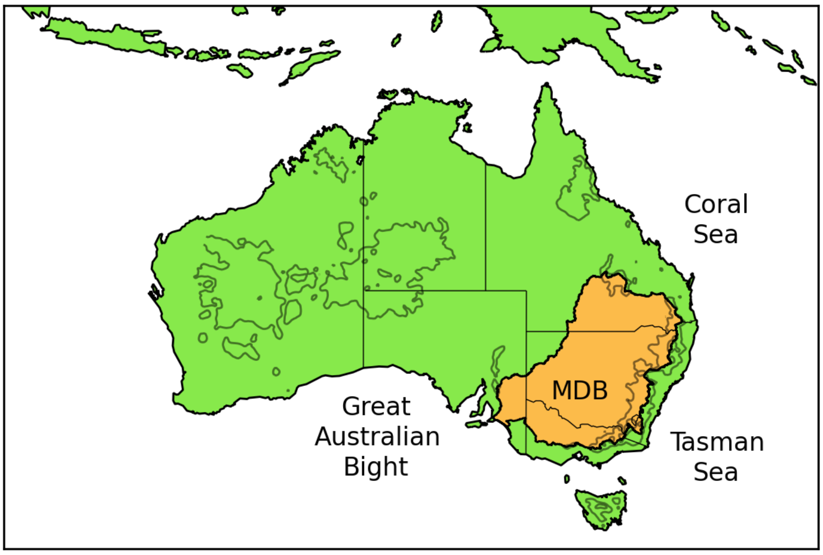

Figure 1.1: Australian continent and surrounding seas, showing topographic contours (grey) at 500 and 1 000 m, and the Murray-Darling Basin (orange).

agriculture in the MDB accounts for about 44% of the gross national irrigated agriculture production, a $9 billion industry in 2009. In addition, water is drawn for urban and industrial use in Melbourne, Canberra and a number of other important regional centres.

Many of the major rivers in the MDB have their origins in the mountains to the south-east of the basin. The Snowy Mountains region is of particular importance, as it is the source of both the Murray and the Murrumbidgee rivers. Precipitation falling in these mountains is captured in a complex of reservoirs and diverted for power generation by the Snowy Mountains Hydro-Electric scheme before flowing downstream, where it is used for irrigation and human consumption. The wintertime snowpack in the Snowy Mountains is the basis of an important tourist industry for the surrounding communities, and also provides a unique habitat for a number of endangered species.

1.2 Precipitation in south-eastern Australia

The climate of south-eastern Australia is dominated by several important features of large-scale atmospheric circulation whose impacts differ in spatial and temporal scales. The most well-known of these are represented in figure 1.2. Some of these factors only affect Australia in certain seasons, such as the monsoon or tropical cyclones, while other semi-permanent

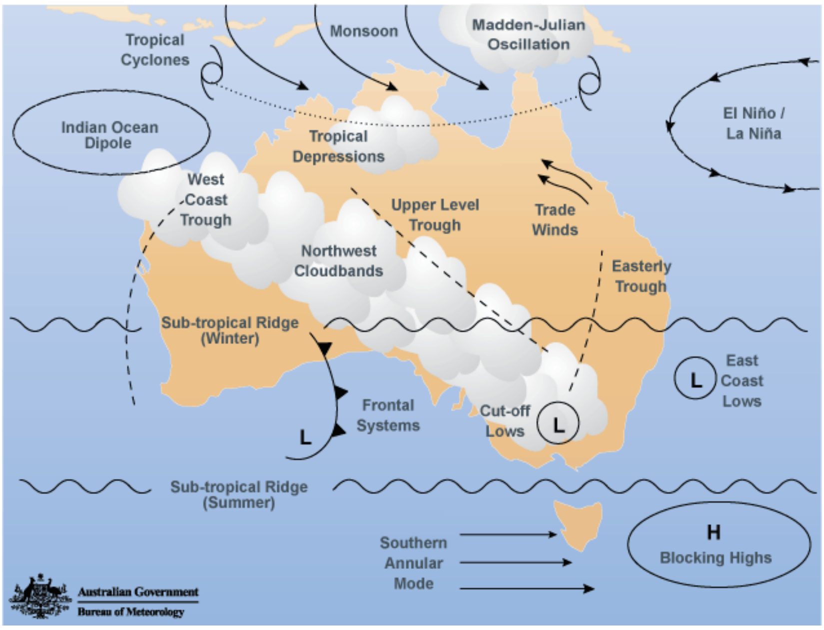

Figure 1.2: Schematic picture showing the major weather and climate drivers in the Australian region. Copyright of the Australian Bureau of Meteorology.

features such as the sub-tropical ridge are present year round, but display seasonal patterns in intensity and position. Transient mid-latitude features such as cold fronts and cut-off lows may likewise impact southern Australia in any season, but are generally more common in the winter months. Several climate modes have been identified as important to south-eastern Australia, in particular El-Niño Southern Oscillation and the Southern Annular mode. This section outlines some of the fundamental aspects of the weather and climate drivers for south-eastern Australia, and presents some of the scientific literature relevant to the research topic.

1.2.1 Synoptic features associated with precipitation

Precipitation is ultimately the result of the ascent of moist air, which cools adiabatically as it rises and eventually condenses to form small droplets. There are a wide range of mechanisms to cause ascent, but the most important mechanisms for the mid-latitudes, especially during the winter months, are the synoptic-scale weather systems that feature in news forecasts and chart discussions.

The decomposition of precipitation in south-eastern Australia into different synoptic types has been the subject of a number of studies. The amount of precipitation brought by individual synoptic systems is highly variable and depends on meteorological and topographical factors. Wright (1989) described five major synoptic types (two frontal, a post-frontal, and two cyclonic low categories) for the south-eastern state of Victoria for the winter period of June–September. The relative contribution to daily precipitation statistics of each type was found to vary substantially in different geographical regions, and in particular notes that the influence of frontal systems was reduced in regions leeward of topographical barriers. Pook et al. (2006) classified daily precipitation in the "cool-season" (April–October) in Western Victoria, according to "frontal" and "cut-off low" categories. This analysis found that at least half of the precipitation, and that 80% of all daily records greater that 25 mm, could be attributed to cut-off lows, emphasising the importance of these systems for precipitation in South-Eastern Australia. Specifically considering precipitation in the Victorian high country, Landvogt et al. (2008) showed that precipitation was produced by a variety of synoptic meteorological conditions; with about half of the precipitation sourced from pre-frontal rainfall and the remaining half almost equally shared between post-frontal rainfall and the passage of low pressure systems over the region.

1.2.2 Recent declines in precipitation

South-eastern Australia has been in an intermittent drought for much of the two decades to 2010 (Murphy and Timbal, 2008; Timbal, 2009), with severe drought in 1991-95, 2002-03 and 2006. The nature of the decline appears to be a shift to lower precipitation amounts between 1997 and 2009, occurring principally in the autumn/winter months. Cool season (April–October) precipitation in southern Australia was found to be related to mean sea level pressure, specifically the intensity/position of the sub-tropical ridge (Larsen and Nicholls, 2009), which has been linked to trends in the southern annular mode (Nicholls, 2010)

1.3 Orographic precipitation

Precipitation in alpine regions is *orographic* in the sense that it is enhanced or modified in some way by the influence of topography on the meteorology of the area. Mountainous barriers such as the GDR impede the flow of moist air, and depending on conditions such as the thermodynamic profile and flow-speed/topography relations (Houze, 1993), a lifting mechanism is provided. Generally this serves to enhance rainfall during widespread precipitation events, but it is not uncommon to observe clouds over the ranges when conditions are clear elsewhere.

Orographic precipitation in Australia has received little attention in comparison to mountainous regions of Europe (e.g. Rotunno and Houze 2007, Volkert and Gutermann 2007), North America (e.g. Stoelinga et al. 2003, Ikeda et al. 2007) and New Zealand (Wratt, 1996), where intensive observational studies have been conducted with the aim of characterising surface precipitation distribution and improving microphysical parametrisations, amongst other things. This is perhaps understandable given that the contribution of orographic precipitation to the Australian annual total is relatively small, owing to the relatively low profile of the GDR and the absence of a nearby warm moisture source upwind of the range. Nevertheless, the importance of orographic precipitation in these mountain ranges to the economy and ecology of south-eastern Australia justifies further consideration.

1.3.1 Supercooled liquid water in orographic clouds

The term "supercooled liquid water" (SLW) refers to liquid-phase cloud droplets that exist at temperatures below freezing. These conditions frequently occur in shallow orographic clouds during wintertime, especially in post-frontal conditions. Using satellite-derived cloud top phase retrievals, Morrison et al. (2011) found that clouds with supercooled liquid tops were by far the most commonly observed cloud types along the GDR during wintertime. Precipitation rates from these clouds are often very low in spite of their extensive lifetimes (Rauber and Grant, 1987). Mossop and Hallett (1974) showed that secondary ice production, which is necessary for the development of precipitation when ice nuclei are scarce, was proportional to the concentration of cloud droplets with radius $> 12\ \mu$m. Supercooled liquid water, despite its inherent instability, can persist for extended periods under certain conditions.

These clouds are of interest to the scientific community for a number of reasons. Firstly, they represent the one of the few environments where cloud seeding activities have produced a detectable impact (Morrison et al., 2009; Manton and Warren, 2011), and conversely, the wide coverage and short life-cycle of hydrometeors within the cloud are hypothesised to render them potentially susceptible to *intentional* modification through glaciogenic cloud seeding practices (section 1.4.1), as well as *inadvertent* modification by aerosol pollution leading to the suppression of precipitation (Levin and Cotton, 2009), discussed further in section 1.4.2

1.3.2 Simulating orographic precipitation

The conceptually simple mechanism for the production of precipitation through forced orographic uplift lends itself well to attempts at numerical simulation. Most realistic orographic precipitation scenarios involve processes that occur at temperatures below freezing; the production of snowflakes, graupel or cloud ice. These sub-grid scale processes are represented in numerical models by microphysical parametrisations. Out of computational necessity, the earliest models (e.g. Cotton 1972) treated the microphysics by external forcing from the larger-scale flow, with no feedback from the microphysics to the larger scales. Improvements in computational capabilities led to the development of two main schools of microphysics parametrisation: the "spectral" (or "bin") schemes (Young, 1974), which explicitly simulate particle size distributions for hydrometeor species, and "bulk" schemes, which predict one or more parameters for each species (Lin et al., 1983), assuming size distributions follow pre-defined functions.

The spectral schemes typically require more computational resources, and even with modern facilities the cost is prohibitive for their use in numerical weather prediction, and is generally limited to specialist applications. The bulk schemes are used in a range of applications, from global climate models to high resolution micro-scale weather simulations. Bulk schemes vary in complexity depending on the application, with the simplest "single-moment" schemes predicting only mass concentrations for each species, whereas "double-moment" schemes also predict number concentration. Higher order schemes also exist, predicting certain features of the hydrometeor size distributions. Field campaigns aimed at improving the parametrisations used by these bulk schemes (e.g. Stoelinga et al., 2003) have resulted in the advancement of modern schemes such as that of Thompson et al. (2004), a quasi-double moment scheme which is available through the Weather Research and Forecasting model used in this thesis. This specialist scheme has been explicitly tuned to wintertime orographic conditions, and is capable of representing SLW and frozen hydrometeors with remarkable fidelity (Thompson et al., 2008).

1.4 Human impacts on cloud microphysics and precipitation

1.4.1 Modification of precipitation through cloud seeding

The efficacy of cloud seeding activities has been a matter of scientific contention for decades. Schaefer (1946), while attempting to discover suitable “ice nuclei” to facilitate ice crystal growth in supercooled liquid clouds, accidentally discovered that the introduction of a small amount of dry ice to the cloud chamber resulted in the rapid conversion of liquid to ice. The sublimation of the dry ice resulted in a sufficiently cold plume of carbon dioxide to instantly freeze cloud droplets, which in turn acted as effective nuclei for the rest of the cloud in chamber. Very shortly after this discovery, Vonnegut (1947) discovered that silver iodide crystals formed effective artificial ice nuclei due to similarities in the lattice constant of the crystalline structure.

These laboratory discoveries were quickly followed by the first cloud seeding trials. Kraus and Squires (1947) describe the successful seeding of clouds in Massachusetts with dry ice from an aircraft. This initial success was followed by the rapid commencement of cloud seeding trials globally. A variety of different hypotheses about the most suitable conditions for seeding were examined, but the goal of establishing a statistically significant increase in surface precipitation was not attained to the satisfaction of the scientific community, with a few notable exceptions.

Ryan and King (1997) describe the experience of cloud seeding in Australia between 1947 and 1994, outlining the various environments and mechanisms tested during this period. The only well-supported positive result occurred in the Tasmanian trials, where both stratiform and cumulus clouds were targeted. These results were recently reviewed by Morrison et al. (2011), who used a double ratio on monthly area-averaged rainfall for the months of May–October to demonstrate statistically significant increases of 5 to 14% in the monthly rainfall for seeded months.

The Australian CSIRO conducted cloud seeding trials in the Snowy Mountains in 1950–1959 (Smith et al., 1963), based on the release of silver iodide smoke from aircraft over a target area, and comparison of surface precipitation with an unseeded control area. The primary analysis compared the ratio of control to target precipitation during seeded and unseeded periods, and found a positive impact, but subsequent analyses and controversy over the conduction of the experiment rendered the results ultimately inconclusive. It was not until the recent Snowy Mountains Precipitation Enhancement Research Project (SPERP; Manton et al., 2011) that a conclusive, positive result was verified.

1.4.2 Aircraft studies of clouds and pollution

The potential for aerosol pollution to modify cloud microphysical structure has been appreciated for some time. Warner (1968) used aircraft observations to investigate cloud condensation nuclei (CCN) below could base, and cloud droplet size spectra just above the lifted condensation level, both downwind and upwind of sugar cane fires in Queensland. Clear differences in droplet size spectra were shown, with elevated droplet concentrations and lower droplet sizes seen within the smoke plume. Warner speculated that these observations could explain reduced rainfall amounts at inland stations coincident with increases in sugar cane production, but was unable to rule out other factors.

Eagan et al. (1974a, 1974b) showed the opposite effects that aerosol pollution of clouds can cause. Emissions of large particles (0.3–8 μm) from a paper mill caused clouds downwind to have a much broader droplet spectrum, containing more large droplets (> 30 μm) than clouds outside the plume. Smoke from forest fires, however, caused narrower droplet size distributions and higher concentrations of droplets. Both observations were speculated to affect precipitation in an opposing manner; the reduced droplet size spectrum due to the forest fire smoke would cause decreased droplet collection and coalescence efficiencies, thus reducing precipitation, and the converse would be true for the paper mill smoke.

1.4.3 Satellite retrievals of cloud microphysics

The advent of multi-spectral satellite-based radiometer data enabled the study of cloud microphysical characteristics on a global scale. Rosenfeld and Gutman (1994) developed a method using visible radiances from Advanced Very High Resolution Radiometer (AVHRR) to retrieve cloud-top effective droplet radius, based on the higher spherical albedo of smaller droplets.

Combined with satellite-borne precipitation observations (TRMM precipitation radar), these were used by Rosenfeld (2000) to establish the hypothesis of rainfall suppression due to aerosol pollution. "Pollution plumes" were identified from satellite imagery downwind of urban and industrial centres. Examples were shown from around the world but particular focus was given to south-eastern Australia, noting that the relatively pristine background environment made the impacts more clear. Regions identified as "polluted" were found to have r_e values consistently below the precipitation threshold of 14 μm, while outside the plumes the values were generally higher. Precipitation radar echoes were of lower magnitude and less spatial coverage within the plumes than outside. Both warm and ice processes are supposed to be affected, with the smaller droplets being less likely to coalesce with one another, as well as leading to slower depositional growth (riming) of existing snowflakes (Mossop and Hallett, 1974).

This research has been controversial, with Ayers (2005, 2009) showing that the weather systems originally explored by Rosenfeld were not typical of precipitating systems affecting South-Eastern Australia, so any effect on such clouds would be negligible in terms of seasonal precipitation. Levin and Cotton (2009) reviewed the status of research into the impact of pollution on clouds and precipitation, finding that while in-situ observations of clouds verify the link between atmospheric aerosol loading and cloud droplet number concentration, the effect of pollution on surface precipitation observations has not been established. A lack of observational studies linking aerosol pollution to changes in precipitation, and the failure of these studies to rule out meteorological factors were identified as obstacles to ascertaining this effect. It was noted that "orographic clouds are the most susceptible to modification in precipitation by pollution owing to the modest liquid water contents in them, the relatively short time the drops and ice crystals spend in the clouds and the large areal coverage", which has some resonance with the hypothesis of Rosenfeld (2000).

Considering surface precipitation to be a key indicator of any impact of pollution, Givati and Rosenfeld (2004) considered the impact of urban and industrial air pollution on the "orographic enhancement factor" *Ro*, which was defined as the ratio of hill-top to upwind low-land precipitation. Decreases of *Ro* were found on the order of 28% downwind of San Diego in California, and no such trend was shown for the relatively clean comparison site in northern

California. Comparable results were reported for polluted/clean regions of Israel. Changes in cross-barrier flow were rejected as an alternative hypothesis to explain the observed trends in *Ro* through the use of a radiosonde regression model. The strongest decreases were found to be mid-slope on the windward side of the mountains, and a corresponding, but smaller, increase was identified on the leeward slopes.

The findings of Givati and Rosenfeld (2004) have been disputed by Alpert et al. (2008), who re-evaluated the trends in *Ro* for *all* potential hill-top/low-land station pairs. About 50% of these were found to show a *positive* trend in *Ro*, and due to the high variability of precipitation in the mountains, statistically significant trends of both positive and negative signs were possible. Alpert et al. (2008) recommended that *Ro* be defined using a cluster of seaside stations to avoid urban impacts on inland data, and using this definition found results that contradicted those of Givati and Rosenfeld (2004), showing "no evidence of any suppression of rainfall over the mountains due to pollution". Givati and Rosenfeld (2009) responded by performing a more robust analysis, again using gauge pairs but requiring that the annual precipitation amounts of the gauge pairs met certain correlation criteria. For gauge pairs with $R \geq 0.90$, 94% had a negative trend in *Ro*, for $0.80 \leq R < 0.90$ the fraction was 62% and for $R < 0.80$, half of all gauge pairs showed a negative trend.

The disagreement over how to choose gauges to perform the analysis does not appear to have been resolved by this debate, but certainly the comparison of gauges that are well correlated improved the robustness of the analysis performed by Givati and Rosenfeld (2009).

1.5 Summary of research goals in this thesis

The research goals of this thesis are summarised by chapter as follows:

Chapter 2

To present a long-term precipitation record for the Snowy Mountains, and to place the recent drought in the context of this record. Also, to investigate the relationship between station elevation and precipitation decline during the period 1990–2009 for a network of gauges operating in the Snowy Mountains.

Chapter 3

To identify synoptic scale features associated with wintertime precipitation during the years 1990–2009, and to perform a climatology of these events. Also, to evaluate whether declines in precipitation during the analysis period can be attributed to the systems of interest.

Chapter 4

To perform an in-depth analysis of two precipitation events which occurred to the north of the Snowy Mountains, in the nearby Brindabella Ranges. Also, to enhance the understanding of the precipitation processes through the use of high resolution numerical simulations (WRF). Finally, to assess the importance of the post-frontal period in terms of total precipitation amounts received by mountainous areas during these storms.

Chapter 5

To perform a climatology of back trajectories arriving in the Snowy Mountains during winter for the years 1990–2009. Also, to couple the trajectory simulations with precipitation observations in order to evaluate how moisture is transported to the Snowy Mountains during precipitation. Finally, to use the back trajectories as a means of describing the general circulation, and how this relates to precipitation, during different years in the analysis period.

Chapter 6

To directly address the hypothesis that precipitation in the Snowy Mountains has been affected through urban and industrial pollution, through combining surface precipitation observations, satellite-based observations of cloud microphysics and back trajectory techniques.

Chapter 2

Wintertime precipitation in the Snowy Mountains

This chapter outlines the historical precipitation data available for the Snowy Mountains region and examines the nature of the decline in the Snowy Mountains by comparing precipitation amounts in the "drought" period 1997–2009 to the WMO recommended reference period of 1961–1990. The most recent two decades (1990–2009), when more dense precipitation are available, are investigated in some depth to examine the relationship between elevation and precipitation decline.

This chapter will demonstrate that precipitation amounts during 1990–2009 on the western slopes and in the high elevations (> 1000 m) of the Snowy Mountains region have experienced a decline in excess of the general decline in South-Eastern Australia. The contrast in the decline east and west of the ranges suggests that factors influencing orographic precipitation are of particular importance.

2.1 Historical precipitation data

The observational record for precipitation in the Snowy Mountains begins in the 1950's, with the commencement of construction for the Snowy Mountains Scheme. Daily precipitation data was collected continuously and quality controlled by the Bureau of Meteorology for two sites, Cabramurra (CAB) and Guthega Power Station (GPS), until the 1990's (Gauge

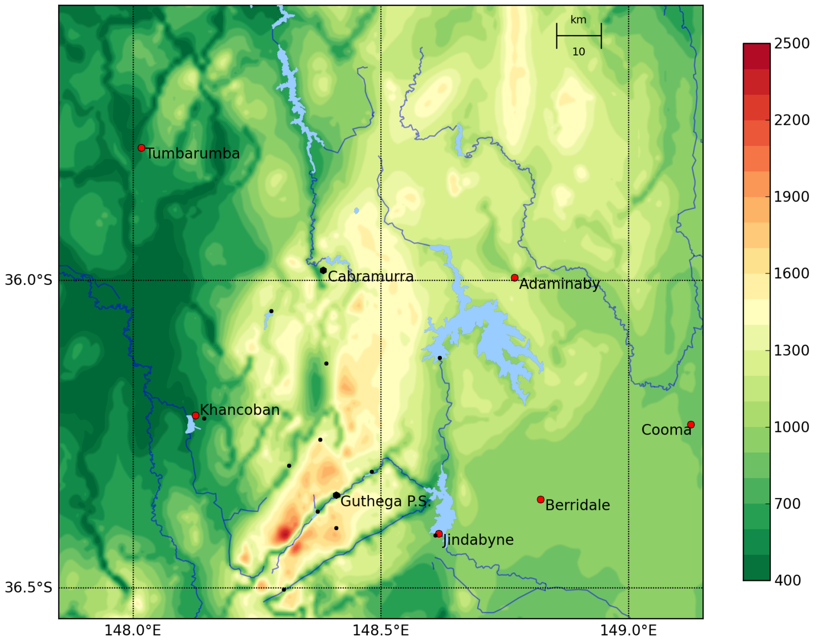

Figure 2.1: Map of the Snowy Mountains region, showing terrain height in metres, localities and major rivers. Also shown are the locations of the two long-term precipitation gauges (black hexagons) and the other gauges discussed in this chapter (small markers; see table 2.1).

locations shown in figure 2.1). Following the installation of automatic tipping bucket gauges at these sites by Snowy Hydro, the daily observations were discontinued.

The timing for this discontinuation was somewhat unfortunate, as it occurred just before the beginning of the 1997–2010 extended drought period in south-eastern Australia. As a result, there has not to date been an assessment of the impact of the drought on Snowy Mountains precipitation amounts (although Nicholls (2005) considered declining snowpack depths in the region). This section considers the extension of the daily precipitation record at these two sites until 2010.

2.1.1 Overlapping precipitation data

At CAB, BOM daily observations (Bureau of Meteorology site number 072091) were recorded from 1955 until 1999. The SHL automatic precipitation gauge was first installed at the same site in 1993 (an overlap period of about six years) and operates to the present date. At GPS (071034), BOM daily observations were taken between 1952 and 1994, and the SHL gauge was installed in 1993. Only about a year of overlap exists for this gauge.

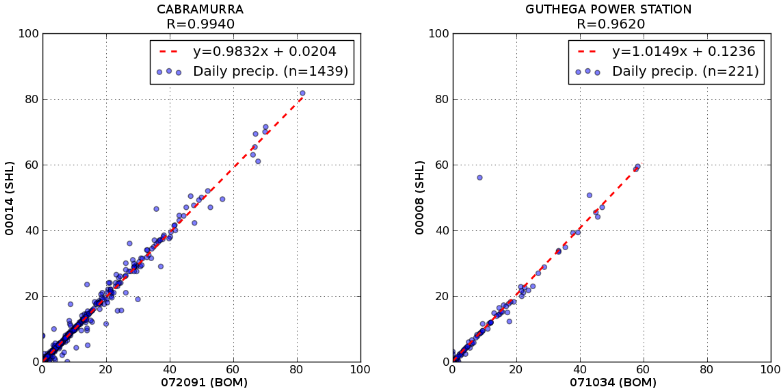

Figure 2.2: Regressions for daily precipitation between BOM and SHL gauges at CAB (left) and GPS (right). The precipitation amounts for the SHL gauges are the accumulated hourly values to 9:00 am each day for the period where both gauges were in operation. Correlation coefficients R are shown above each plot, and the number of observations n is also indicated.

The overlap period was used to compare the precipitation gauges by means of a linear regression, where daily precipitation amounts for all days when both gauges were in operation were used to calculate regression coefficients. Scatter plots of the precipitation recorded at each site and the resultant regression are shown in figure 2.2. This analysis allows us to determine whether the extension of the daily precipitation record at these sites is a valid exercise. The high correlations should not be surprising, as the gauges were co-located, but the near-identity regressions show that there are no systematic differences between using the manual daily and accumulated automatic observations.

The BOM and SHL precipitation records were combined to make a continuous daily record to 2009. During the overlap period, for days on which only one of the observations was available, this value was used, and where both observations were available the average of the observation was used.

The daily precipitation amounts were accumulated to estimate annual and wintertime precipitation amounts. To maintain consistency between the manual and automatic observations, quality control criteria that were applicable to both were devised. For the daily observations, multiple-day accumulations (Viney and Bates, 2004) were rejected, and for the automatic totals, all observations for a given day were required to be of “good quality”, which includes minor edits performed by SHL technicians to correct spurious tips. A total was calculated only if at least 85% of the required daily observations were available. To estimate the seasonal

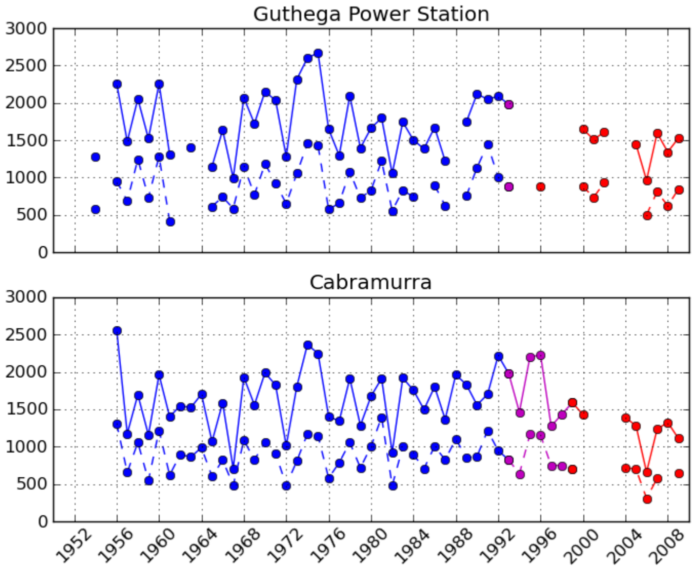

Figure 2.3: Annual and wintertime precipitation time series composites for GPS (upper) and CAB (lower). Solid lines represent annual totals, and dashed lines are the wintertime (May–September) totals. Blue lines indicate that the totals were summed from manual daily observations, red indicates accumulated automatic data and magenta indicates the overlapping period.

or annual totals, the average precipitation per observation day was multiplied by the number of days in the averaging period, that is:

$$P_s = N_s \frac{\sum_{i=1}^{n_{\mathrm{obs}}} p_i}{n_{\mathrm{obs}}}, \tag{2.1}$$

where P_s is the seasonal/annual precipitation amount, N_s is the total number of days in the season (153 for May–September), p_i are the daily precipitation observations which meet quality control criteria and n_{obs} is the total number of these observations. In general, the daily precipitation record was much more complete at CAB than at GPS, with 99% of manual daily records compared to 82%, and 73% of automatic observations compared to 69%. Wintertime completeness for the manual observations was about the same, but for the automatic totals the values were lower at 71% and 62% respectively.

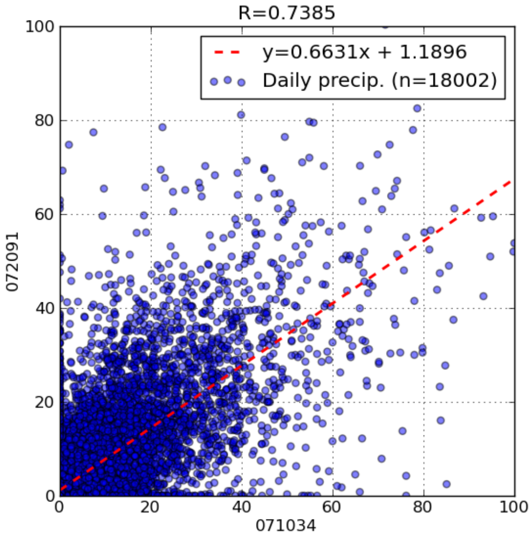

Figure 2.4: Regression between merged daily precipitation records at CAB (vertical axis) and Guthega Power Station (horizontal axis).

2.1.2 Estimating missing values

The effect of the missing data on the annual totals can be seen in figure 2.3. Both sites show multiple years where there was insufficient data to estimate a total, particularly during the later years where the automatic daily totals were used. To generate a single reasonably complete daily record, the absent daily precipitation at CAB was in-filled with values from GPS. Regression coefficients were calculated from all days with observations at both sites, as shown in figure 2.4. The CAB record was used as is was generally more complete, and had a longer overlap period between the manual and automatic observations.

Figure 2.4 shows a good deal of variability between the two sites. The correlation coefficient between the two records is about 0.74, and there are a number of days on which substantial precipitation is recorded at one site while nothing is recorded at the other. This is most likely because the two sites are located a reasonably large distance apart (46 km), and on opposite sides of the range, so GPS is far from an ideal predictor for CAB daily precipitation. Nevertheless, the resultant daily precipitation record is very nearly complete, with 97.5% of days recorded, and due to the smoothing effect of averaging, the annual and wintertime totals should not be overly affected by the poor correlation between the sites. This method is preferable to estimating seasonal totals from the incomplete data sets, as nearly all of the

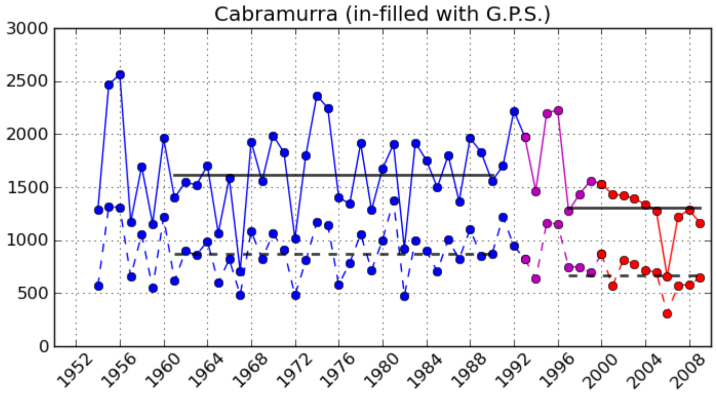

Figure 2.5: Annual and wintertime precipitation time series composite for CAB, with missing values estimated from GPS data. The black solid (dashed) lines show average annual (wintertime) precipitation amounts for 1961–1990 and 1997–2009.

days are accounted for by precipitation observations.

2.1.3 The long-term precipitation record

Figure 2.5 shows the annual and wintertime precipitation amounts for CAB, using GPS daily observations to predict precipitation amounts for missing days. The period 1997–2009 has been recognised as a period of significant drought in south-eastern Australia (Timbal, 2009), and the average annual and wintertime amounts during this period are shown in black. For comparison the average amounts in the period 1961–1990 are also shown. A decrease from 1613 to 1307 $\mathrm{mm\,yr^{-1}}$, or 19% is evident in the annual amounts, and for the wintertime amounts the decrease was from 866 to 672 $\mathrm{mm\,yr^{-1}}$, or 22%.

The decline in precipitation was calculated in the same way for south-eastern Australia, using all of the BOM “High Quality” gauges (Lavery et al., 1997) south of 33° S and east of 135° E, which was the analysis region used by Murphy and Timbal (2008). The annual and wintertime declines are 14% and 15% respectively. The difference in the amount of decline is substantial and is discussed in some detail in the following section.

The analysis of the historical precipitation data is completed by considering the average monthly amounts in the two periods indicated in figure 2.6. This figure shows on a month by month basis the decline in precipitation in CAB during the recent drought. This figure corresponds closely to Murphy and Timbal (2008, Fig. 4), which uses all precipitation data in the south-eastern region but was created in 2006. Appendix A.1 shows the analysis of Murphy

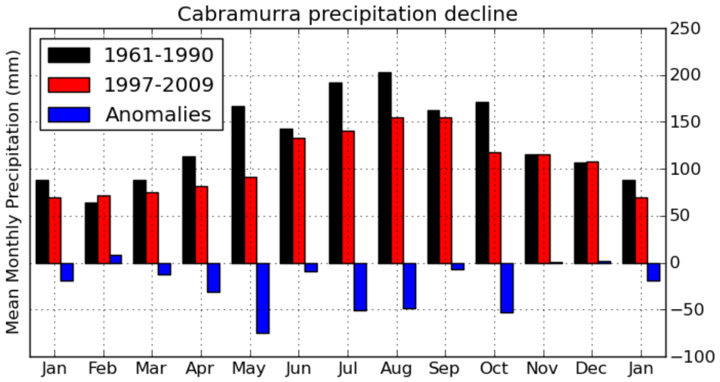

Figure 2.6: Average monthly precipitation amounts for CAB (with missing days estimated from GPS data) for the periods 1961–1990 and 1997–2009, with differences shown by the blue bars.

and Timbal (2008) updated to cover the period 1997–2009, using the “High Quality” BOM monthly data.

A decline is noted in all months from March–October with the strongest declines in May, as found in the whole of south-eastern Australia (the decline in the so-called “autumn break”).

The decline in precipitation in June, August and October is relatively more substantial in CAB than for the south-eastern average, and the autumn months of March and April relatively less important. However, the use of only one gauge raises questions about the representativeness of this pattern of precipitation decline. Although the pattern for Guthega Power Station is qualitatively similar, these patterns need to be more thoroughly examined. The remainder of this chapter takes a closer look at the last two decades of precipitation data from a more dense network of gauges that have been operating in this period.

2.2 Precipitation in 1990–2009

The Australian Bureau of Meteorology (BOM) has a number of daily (manual) precipitation observation sites and an increasing number of Automatic Weather stations (AWS) in the wider Snowy Mountains region, but the density of the network in the high elevation regions above 1000 m is very low. Only two AWS operate for the period 1990–2009, with an additional two manual observation sites at the major ski centres.

Furthermore, the measurement of precipitation in this environment is notoriously difficult.

Especially in the winter months (May–September), high winds and frozen hydrometeors frequently result in under-reporting of precipitation amount, and the remote nature of the Snowy Mountains region makes access for equipment maintenance challenging. It is not uncommon to find extended periods of missing data in the observational records, and there may be substantial disagreement, even between gauges that are closely located. To address the shortcomings of the existing alpine precipitation data, the primary purposes of this section is to present and discuss an augmented precipitation dataset spanning the period 1990–2009, consisting of the established BOM daily precipitation observations and an independent network of precipitation gauges maintained by the operators of the Snowy Mountains Scheme.

2.2.1 The Bureau of Meteorology precipitation gauge network

Precipitation records from all BOM gauges between 35° and 37° S and east of 146.5° E (figure 2.7) were quality controlled to ensure an adequate number of observations were available. At least five years of data during each of which more than 85% of daily wintertime observations were required for each site, and the span of these data was further required to be at least ten years. In order to overcome the effect of missing data on monthly and seasonal totals, precipitation accumulations for each gauge were estimated from the average daily precipitation amounts for a given month. At least 85% of days were required to make each estimate, with months and seasons rejected if this criterion was not met.

2.2.2 Snowy Hydro legacy gauges

The Snowy Hydro Ltd. (SHL) gauges form a network of heated tipping bucket gauges in the alpine regions of the Snowy Mountains, with locations and data availability for these gauges provided in table 2.1. The first gauge was established in 1989, and the network grew to twelve gauges providing hourly precipitation from 1995 to the present date. The hourly data was quality coded to indicate manual corrections and equipment faults, and has been cumulated for each 24 hour period to 9 am Local Standard Time (23 UTC) on each day in the analysis period. About 90% of the combined daily record for these gauges was available once days with missing or QC-flagged data were rejected. At two sites (Cabramurra and Guthega Power Station) a BOM manual gauge had previously been maintained, and the precipitation record

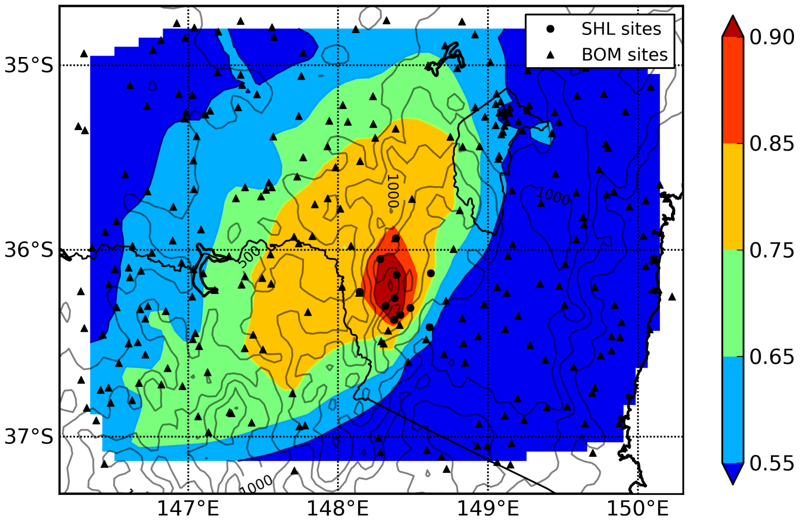

Figure 2.7: All precipitation gauges in the Snowy Mountains region in operation during the analysis period. Filled contours show correlation coefficient with the *alpine daily average* precipitation calculated from the high-elevation SHL gauges. Contours of topographic elevation shown at intervals of 250 m, with the highest contour shown at 1500 m.

was extended back to 1990 using a conversion based on regression of the daily precipitation values during the overlapping period.

Daily precipitation amounts were accumulated to give monthly and seasonal totals in the same manner as for the BOM gauges.

2.2.3 Grouping of precipitation gauges

Daily precipitation records from the gauges with the highest elevations were found to be generally very well correlated with one another. A group of ten "high elevation" gauges from both the BOM and SHL networks (table 2.1) was chosen based on elevation, location near the main range and completeness of data to form a *daily precipitation observation* for the alpine region. This observation is the best available indication of precipitation amount in the high elevation regions, with at least three gauges contributing to the average on any given day.

All of the precipitation records were correlated with the alpine daily precipitation observation to determine their comparability, with correlation coefficients contoured in figure 2.7. Gauges with correlation coefficient R of greater than 0.7, generally located along the lower slopes and to the west of the Snowy Mountains region, were selected to form a "western slopes" group of

Site	Lon.	Lat.	Elev.	An. Pr.	An. %	M-S %	Avail.
The Kerries	148.38	-36.26	1740	1358	80	72	1995
Jagungal	148.39	-36.14	1659	1705	92	97	1990
Guthega Dam	148.37	-36.38	1558	1457	90	92	1994
Tooma Dam	148.28	-36.05	1221	1775	96	91	1992
Island Bend	148.48	-36.31	1221	1061	90	89	1995
Geehi Dam	148.31	-36.30	1175	1656	96	96	1992
Perisher Ski Centre*	148.41	-36.40	1735	*1696*	75	88	1976
Thredbo Village*	148.30	-36.50	1380	*1684*	89	78	1971
Guthega P.S. †	148.41	-36.35	1320	1479	88	87	1952
Cabramurra †	148.38	-35.94	1482	1373	97	97	1955
Khancoban‡	148.14	-36.23	328	863	98	99	1993
Jindabyne§	148.61	-36.42	927	587	94	93	1992
Eucumbene§	148.62	-36.13	1180	793	86	84	1992

Table 2.1: The precipitation gauges introduced for this analysis. The first group are the nine gauges that form the "High Elevation" group, including six SHL gauges, two manual BOM gauges (*) and the two merged manual/automatic datasets (†). The SHL Khancoban gauge (‡) is added to the network of 37 BOM gauges on the lower western slopes, and the remaining SHL gauges (§) are included with 19 BOM gauges to the east of the ranges. Annual precipitation, percentage of daily precipitation available (annual and May–September) and year of commission are also shown. Values in italics are not quality controlled in any way and are calculated from monthly accumulations available on the Australian Bureau of Meteorology website.

38 gauges (including one SHL gauge). To the east of the mountains, daily precipitation was generally poorly correlated to the alpine average, as these regions are generally located within the rain shadow cast by the mountains during the predominant westerly systems. Indeed, the high gradient in R is seen to coincide with the approximate location of the GDR watershed.

A selection of 21 nearby gauges located to the east (including two SHL gauges) form the "eastern slopes" group. These were selected manually based on their proximity to the Snowy Mountains and non-inclusion in the other groups.

2.2.4 Precipitation averages for the period 1990–2009

Figure 2.8 shows monthly precipitation averages for the 20 year analysis period. The high elevation and western slopes gauges have a clear June–September maximum, with precipitation amounts roughly double for the high elevation gauges. Precipitation to the east of the ranges follows a substantially different pattern, with winter precipitation amounts substantially lower than for the western group despite the higher average elevation of the eastern group (about 860 m) compared to the western group (about 645 m). The summer values for

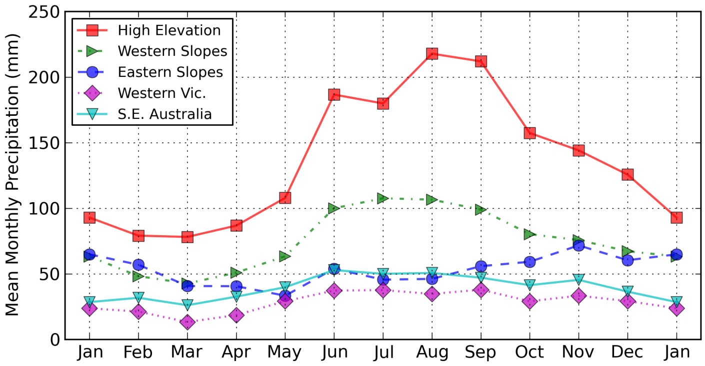

Figure 2.8: Monthly precipitation averages for groups of Snowy Mountains region gauges (see text) for the years 1990-2009. Included for comparison are the means for south-eastern Australia ("High Quality" gauges used by Murphy and Timbal (2008)), and the western Victoria gauges used in the climatology of Pook et al. (2006), except for Bendigo Prison station, which closed in 1992.

the eastern and western groups are essentially the same, suggesting that topographic effects play a much more important role in wintertime. For comparison, the precipitation amounts for the gauges used by Murphy and Timbal (2008) and Pook et al. (2006) have also been included, demonstrating that precipitation amounts are about a factor of four times those of south-eastern Australia, and up to six times that for the upwind plains of western Victoria.

2.2.5 Wintertime precipitation and elevation

May–September precipitation amounts are of particular relevance to this research for a number of reasons, as discussed in the introductory sections. Rain gauge elevation has been shown to have a clear influence (Houze, 1993) on precipitation amounts, in particular for the wintertime. To formally examine the dependence of precipitation amounts on elevation, the mean wintertime precipitation for all gauges during the analysis period is plotted against station elevation in figure 2.9. Symbols are assigned according to which of the three groups ("eastern","western" or "high elevation"), and which of the two networks (BOM or SHL) the gauge belongs to.

It is natural to treat the western slopes and high elevation gauges together, and a strong relationship between station elevation and winter precipitation (35.6 mm per 100 m) is evident, in spite of a paucity of gauges between 800 and 1200 m. There is a degree of variability which should be expected in a complex topographic environment. The outliers in this figure have

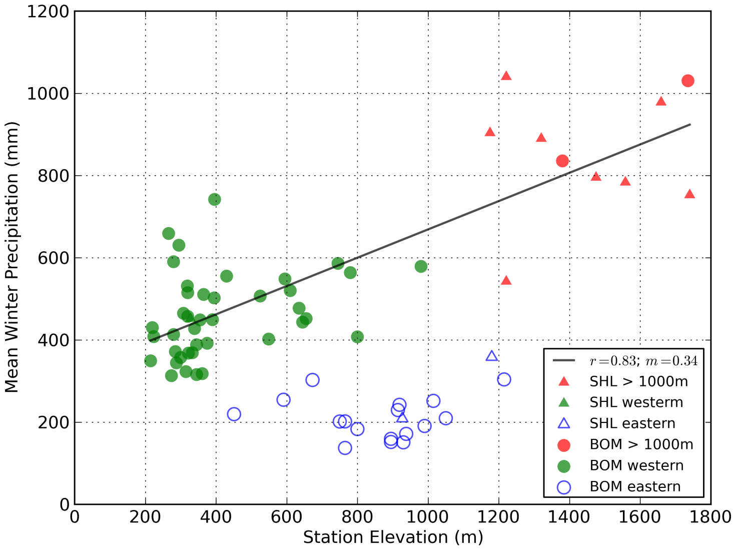

Figure 2.9: Mean winter precipitation plotted against station elevation for all gauges. Eastern slopes gauges plotted with open symbols, western slopes in green shade and high elevation groups in red shade, with different symbols used for gauges from the two networks. Eastern slopes gauges were not used in regression.

been investigated and have reasonable environmental explanations. The three highest wintertime precipitation values from the "western" group are all located in similar environments at the upper ends of major river valleys on the western slopes of Victorian Alps. Interestingly, the lowest and highest precipitation amounts in the "high elevation" group (Island Bend and Tooma Dam) are recorded at gauges with precisely the same elevation, but on opposite sides of the main range. These gauges are also both located within river valleys, but the effect appears to be contrasting on the windward (western) and leeward sides of the range.

The eastern gauges show generally lower precipitation amounts and very little dependence on elevation; despite a spread of 800 m there is only about 200 mm of range in wintertime precipitation amounts.

2.2.6 Precipitation trends and elevation

Precipitation in South-Eastern Australia has been demonstrated to have declined from long-term values during the analysis period, with cool season precipitation affected by a shift towards lower values from about 1997 (Murphy and Timbal, 2008). This type of shift can not be verified in a 20 year time-series, so instead linear trends over the analysis period

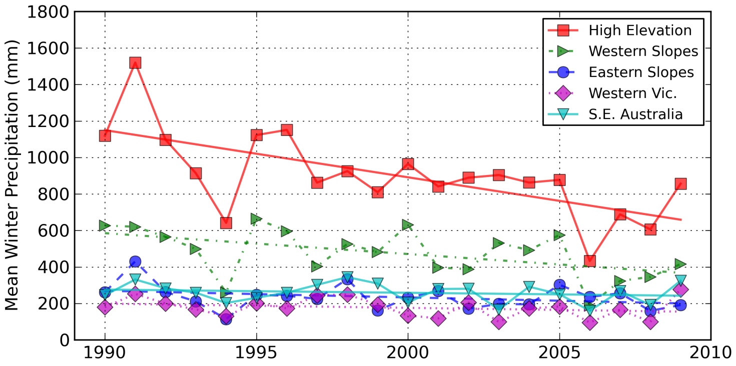

Figure 2.10: May–September precipitation averages for the Snowy Mountains gauge groups. The linear fits have slopes of -23.18, -11.44 and -3.30 respectively. Trends for the high elevation and western slopes are statistically significant with $P < 0.02$.

are used to characterise the decline for the Snowy Mountains region. Figure 2.10 shows the May–September average precipitation accumulation for each of the three groups. Of note are the particularly dry periods in 1994 and 2006 for all groups, which are associated with extended El-Niño conditions (Meyers et al., 2007). Wintertime precipitation for the high elevation gauges correlates quite closely with the western slopes gauges ($r = 0.89$), but as expected, is less clearly related to the eastern regions ($r = 0.66$). Incidentally, the correlation coefficient between May–September precipitation with the mean for all of the 117 mainland BOM "high quality" gauges (Lavery et al., 1997) south of 30° S and east of 135° E is also very high ($r = 0.85$), suggesting that the same drivers are affecting wintertime precipitation overall in South-Eastern Australia.

Strong negative trends are evident in the wintertime precipitation amount for both the high elevation and western slopes. The value of the trend for the high elevation sites is -26 mm per year, amounting to 520 mm (-43%) over the analysis period, and for the western slopes it is -11 mm per year, or about -37%. Both of these declines are substantially stronger than that reported by Murphy and Timbal (2008) (-14% between 1997 and 2006 compared to the long-term average), as well as that apparent in the south-eastern "high quality" BOM network, which experienced an average May–September decline of 28.3% over the same period. The nearby eastern slopes, in contrast, have a rate of decline of slightly less than 26%, suggesting that possibly orographic influences for both the lower western slopes and the high elevation sites have been impacted.

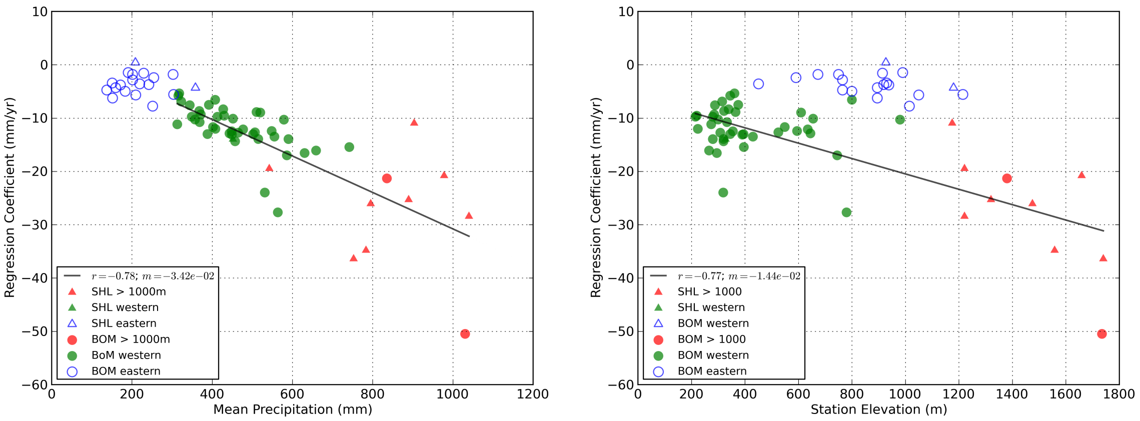

Figure 2.11: Regression coefficient for 20 year trend plotted against mean wintertime precipitation (left), and station elevation (right). Symbols and regressions as for figure 2.9.

When considered on a gauge-by-gauge basis, some subtle features of the precipitation decline become apparent. The first panel of figure 2.11 shows the regression coefficient for the 20-year decline plotted against the mean wintertime precipitation for each site. An across-the-board reduction in precipitation by some fraction of the long term average would result in a good linear fit. This appears to hold well for the eastern and western slopes, where there are very few outliers. However, the high elevation data are very scattered, suggesting that the decline is not simply proportional to the precipitation amount for these gauges.

Plotting the decline against station elevation (second panel of figure 2.11), gives a fit that is better overall, and the scatter for the high elevations is substantially reduced. The linear fit for this relationship has a slope of −1.45 mm per 100 m per year, and with a correlation coefficient of 0.79 it is a highly significant trend ($P < 0.001$). When the *relative* decline is plotted against station elevation, the resulting trend (−0.057% per 100 m per year with $r = 0.32$) is much less significant, so the relationship between precipitation decline and elevation is best described in absolute terms. In terms of snowpack depth and catchment inflows, it is the absolute decline that is of most interest. The Snowy Mountains catchments rely heavily on high elevation precipitation, and as a result have been badly affected by the precipitation declines.

Figure 2.11 highlights an important outlier in the data. Perisher Ski Centre, the highest elevation site, shows a decline in excess of 50 mm per year. This point is treated with a high degree of scepticism, as such values were not reproduced at any other site in the Australian alpine region. The infrastructure at the ski centre developed substantially during the analysis period, and changes in gauge location and/or instrumentation have not been ruled out. It was noted that if this gauge was excluded from the group, the decline for the other gauges decreased to a value of -36%.

In summary, a strong decline in precipitation is evident in the Snowy Mountains region on the western slopes as well as at high elevation. While the nature of the decline at lower elevations is consistent with an overall reduction in precipitation, this is not so clear for higher elevations, where the most significant relationship is between the absolute decline and elevation. This suggests that orographic factors are controlling both the enhancement of precipitation over the lower gauges, as well as the decline during the analysis period. This is supported by the fact that the near-by eastern gauges, which do not depend as much on orographic influence, have a much lower rate of decline.

Chapter 3

Synoptic decomposition of wintertime precipitation

The water catchments in the Snowy Mountains region are fed primarily from snow-melt following the accumulation of winter precipitation at high elevations, and have been particularly badly affected by this decline. The availability of new precipitation data in this hydrologically important area for South-Eastern Australia provides a context to examine synoptic factors which affect precipitation on a day-to-day basis.

Wintertime precipitation in South-Eastern Australia is essentially dominated by mid-latitude systems that form as a result of baroclinic instability (Ryan and Wilson, 1985). Some features that are commonly associated with these systems are surface and upper level depressions in pressure/geopotential fields, troughs in 1000–500 hPa thickness, and cold fronts. All of these features have served as the basis for synoptic climatologies of South-Eastern Australia in the past (Wright 1989, Pook et al., 2006, Landvogt et al. 2008).

A confounding aspect of such synoptic climatologies is that systems may at times show aspects of different synoptic types, or one type may develop into another, even when as few as two primary categories are considered. For instance, cold fronts are conceptually associated with a circulatory system, even if cyclonic flow is not apparent. Conversely, the criteria for cut-off lows in the climatology of Pook et al. (2006) do not preclude the existence of a cold front in association with the circulatory system.

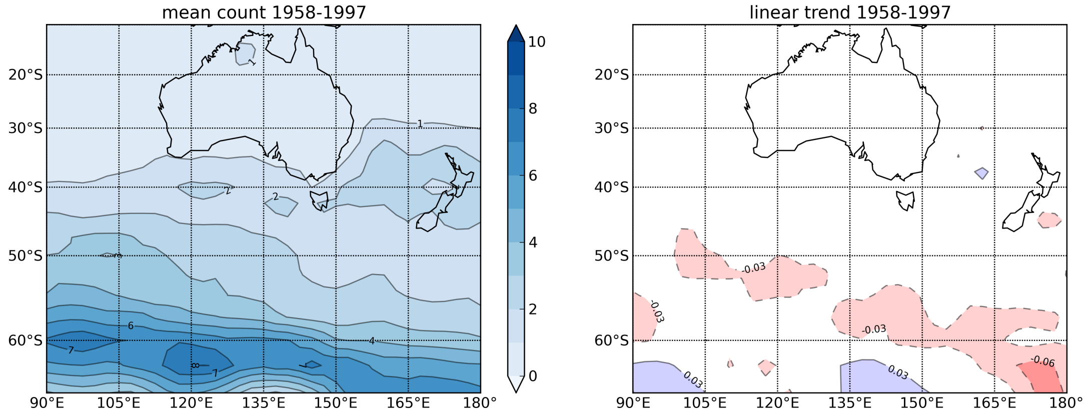

Figure 3.1: Density of lows (left) and linear trend (right) in the Australian region for June–August, 1958–1997. Statistics obtained from the University of Melbourne cyclone tracking web page (http://www.earthsci.unimelb.edu.au/tracks/cychome.htm) using the automatic cyclone tracking scheme of Murray and Simmonds (1991a, 1991b) and NCEP reanalysis-I data.

There is merit in classifying systems by the location of the parent low, as both the proximity to and intensity of the depression centre have a controlling influence over the precipitation recorded at a given location. A climatology of southern hemisphere cyclone density (number of cyclones per degree latitude squared) has been performed by Simmonds and Keay (2000), using the NCEP reanalysis data for the 40-year period between 1958 and 1997. During winter (June–August) a “split” is apparent in the Great Australian Bight region (the large open bay to the south of the continent), where few cyclones are found between 45° and 55° S, and higher numbers are found to the north and south (these results have been reproduced in figure 3.1 for reference). The 45° S parallel is thus a convenient and natural boundary to discern between systems “cut-off” from and “embedded” in the westerly belt.

3.1 Precipitation events and synoptic data

The average daily precipitation record for the high elevation gauges was used in combination with synoptic data to identify “precipitation events”, which were defined as being one or more consecutive days of precipitation with an average daily value of at least 0.2 mm, and a total of at least 1.0 mm, under the influence of a single synoptic feature. The precipitation events were classified with the use of mean sea level pressure/1000–500 hPa thickness, 500 hPa height data and satellite imagery from the following sources:

- The Australian BOM synoptic charts,
- NCEP-NCAR climate reanalysis dataset (Reanalysis-II) gridded data,
- GMS/GOES/MTSAT geostationay infra-red imagery.

The BOM manual MSLP analyses are publicly available from 2000, and the upper level charts from 2004. For the preceding years (1990-1999), MSLP/thickness and 500 hPa height charts were plotted from the NCEP reanalysis data. The manual analyses were used in preference to the automatically generated images where possible, since there are a number of additional observations, such as wind direction and satellite-derived cloud fields, which are incorporated into these charts. Satellite imagery was used explicitly to identify frontal cloud bands in determining whether a frontal passage had occurred, especially when the manual analyses were unavailable. Cross validation using the NCEP reanalysis data and satellite imagery for the years 2001, 2003 and 2004 showed no systematic differences in the classification decisions.

3.2 Classification scheme

Figure 3.2 shows the main categories used in this classification, which were "cut-off lows" and "embedded lows", with an "other" category included to account for the precipitation events which could not readily be attributed to either of the primary categories. This approach recognises that cold fronts are a common feature of both "cut-off" and "embedded" lows, and specifically records whether a frontal passage (as diagnosed by the path of the frontal cloud band and the geopotential thickness gradient) occurs for both types of system. The authors recognise the difficulties of defining the precise location of the front, especially with regard to passages over complex terrain, and the statistics generated from this definition have been used with caution.

The classification scheme ultimately resembles the scheme used by Pook et al. (2006) quite closely, except for a longitudinal shift in the analysis region and the replacement of the "cold front" category with the more general "embedded low" category. Cold fronts are analysed as an additional feature which may or may not be present (i.e. "frontal"/"non-frontal") in both of the major synoptic types.

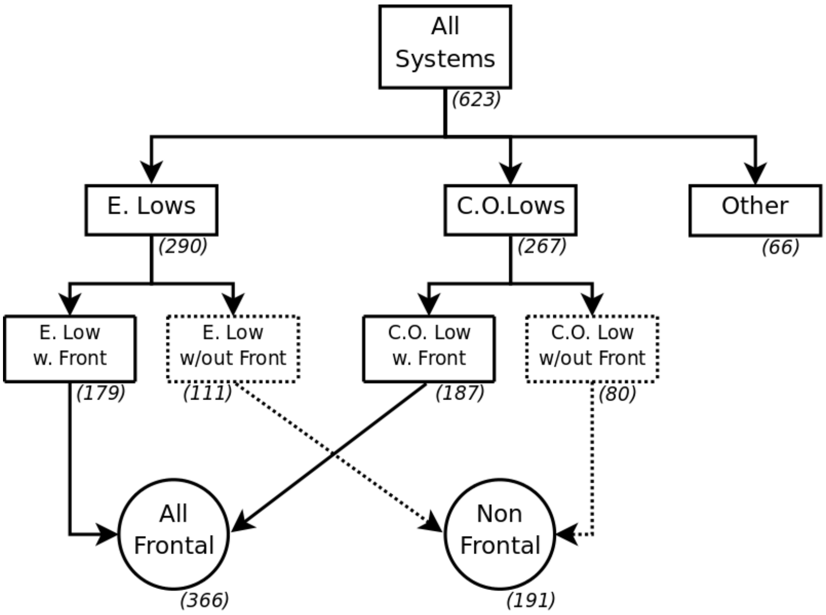

Figure 3.2: Schematic of classification procedure, including total number of each event type classified for winter months in the period 1990–2009.

3.2.1 Cut-Off Lows

Wintertime cyclones propagating over the Great Australian Bight may make landfall over the Victorian coast, pass through the Bass Strait or divert over or to the south of Tasmania. All of these storm paths may be associated with significant precipitation on the mainland. The systems are generally associated with a cold anomaly aloft that is "cut-off" from the Southern Ocean westerly belt (figure 3.3). Precipitation during an event was attributed to a cut-off low if a minimum in either the MSLP or the 500 hPa geopotential field was present east of 135° E, west of 150°, E and north of 45° S. Several previous studies of cut-off lows in the Australian region have required the presence of a closed low at 500 hPa or at the surface, or both (e.g. Qi et al., 1999; **?**, **?**), but Wright (1989) included local minima within clearly defined upper troughs in his 'cold lows' synoptic type. Recently Fuenzalida et al. (2005) employed an objective identification technique which accepted open depressions in order to compile a climatology of cut-off lows for the Southern Hemisphere. In this study it was also decided that circulations around the minima were not required to be closed in order to be included in the cut-off category. Complex systems (with more than one pressure minimum) were only classified as "cut-off" if the major centre of circulation fell within the prescribed region.

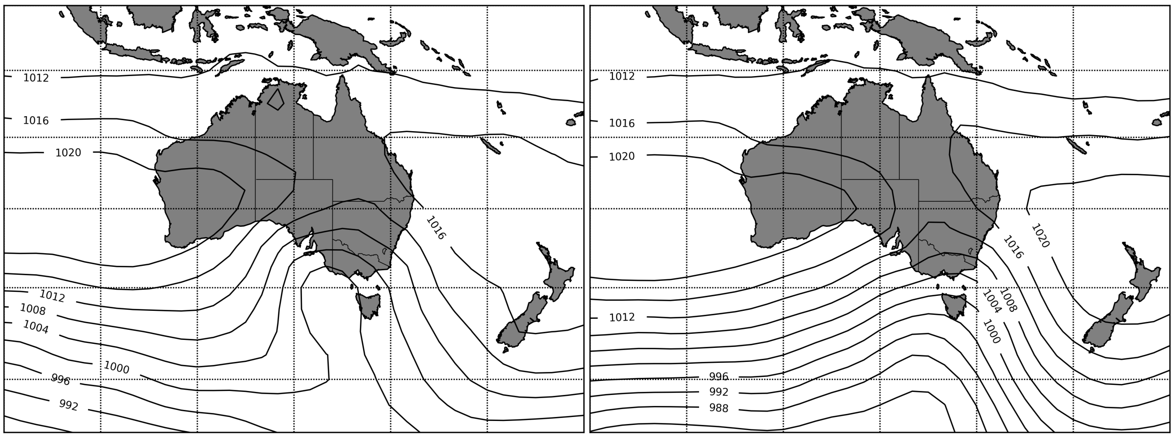

Figure 3.3: Composites of the mean sea level pressure for the 20 cut-off lows (left) and 20 embedded lows (right) bringing the most precipitation to the Snowy Mountains. The intensity of the composite cut-off low is somewhat understated due to the variability of the position of individual lows in the NCEP re-analyses.

3.2.2 Embedded Lows

The circumpolar storm track in the Southern Ocean is a region of high cyclone density, located year-round to the south of 50° S (Trenberth, 1991). Though distant from South-Eastern Australia, cyclones "embedded" in this westerly belt can have a strong influence over weather in the Snowy Mountains, as the frontal bands and large amplitude troughs associated with these systems can extend for more than a thousand kilometres across the Southern Ocean. Precipitation during an event was attributed to an embedded low if it occurred during the passage of a front or trough that could be linked to a cyclone or wave in the westerly belt.

3.2.3 Cold Fronts

Meteorological fronts are characterised by a moving boundary which marks a region of sharp transition in thermodynamic properties between different airmasses. In particular, a cold front moves so that colder, denser air replaces warmer air. Forced uplift of the warmer air in this process result in patterns of precipitation that can be related to finer details of the frontal structure (Browning, 1986). Of particular importance to precipitation in mountainous regions is the "warm conveyor belt" (more recently termed "atmospheric rivers" by Zhu and Newell (1994)) mechanism, where a narrow, low-level jet within the boundary layer just ahead of the surface cold front carries large quantities of moisture poleward. Cold fronts are always associated (at least in a system-relative sense) with cyclonic circulation, and are commonly found in association with both of the above categories.

3.2.4 Other systems

Although the two major systems were found to account for nearly 90% of precipitation events, a number of events were attributed to "other" systems. In particular, it was found that easterly conditions seldom brought substantial precipitation, as they tended to rain out on the rugged coastal ranges.

- *East Coast Lows* (Holland et al., 1987), are potentially destructive, heavily precipitating systems that typically develop from upper level disturbances over the enhanced sea surface temperature gradients near the east coast of the continent.
- *Easterly dips* are characterised by a weak trough along the east coast of the continent. They are a regularly occurring phenomenon in Australian meteorology and signify a tropical-subtropical interaction. These systems are a common precursor for the formation of east coast lows, and are more commonly associated with summertime precipitation in the region.
- *Indeterminate precipitation events* are unable to be associated with any synoptic-scale features. Small-scale convective events may account for considerable precipitation amounts at one or more gauges.
- *Erroneous precipitation recordings* can occur due to a number of reasons, including blowing snow, heavy dew/frost or equipment malfunction.

3.3 Climatological features for the period 1990–2009

A total of 623 precipitation events were classified according to the above scheme, with the full list of events given in appendix A.2. Summary results are shown in table 3.1, where the mutually exclusive categories of "embedded low" and "cut-off low" are further subdivided

	Events	**Total Precip.**		**R. Days**	**Precip. per Event**		
	per yr.	*per yr.*	%	*per yr.*	Q_1	$\tilde{x}$	Q_3
All types	31.1	916.3	(100.0%)	69.0	8.1	20.5	42.4
E. Lows	14.6	364.8	(39.8%)	28.2	6.5	17.2	34.7
E. Lows w. front	9.0	317.9	(34.7%)	20.2	16.0	27.2	49.6
E. Lows w.o. front	5.5	46.9	(5.1%)	8.0	3.1	6.0	13.3
C.O. Lows	13.3	510.9	(55.8%)	35.3	14.9	31.3	52.9
C.O. Lows w. front	9.3	407.9	(44.5%)	25.4	17.8	34.9	59.2
C.O. Lows w.o. front	4.0	103.0	(11.2%)	9.8	8.6	19.4	33.1
All w. front	18.4	725.8	(79.2%)	45.7	17.1	31.9	54.4
All w.o. Front	9.6	149.9	(16.4%)	17.8	4.1	8.9	20.0
Other	3.2	40.6	(4.4%)	5.5	2.5	6.1	14.8

Table 3.1: Summary of statistics from the synoptic decomposition of wintertime precipitation in the Snowy Mountains region during 1990–2009. The mutually exclusive categories of "embedded low" and "cut-off low" are further subdivided into "frontal" and "non-frontal", and the combined "frontal" and "non-frontal" events are also shown. Here, Q_1 and Q_3 represent the first and third quartiles, and $\tilde{x}$ is the median value of precipitation per event.

into "frontal" and "non-frontal". The combined "frontal" and "non-frontal" events are also shown. The median and quartile values of precipitation per event are also given in table 3.1.

3.3.1 Statistics for entire analysis period

Embedded lows account for 47% of all precipitation events, occurring slightly more frequently than cut-off lows (43%). However, embedded lows bring considerably less precipitation on a seasonal basis, accounting for about 40% of precipitation compared to 56% for cut-off lows. Precipitation generally persists for longer during a cut-off low (2.7 days) than for an embedded low (1.9 days).

Cold frontal passages in the Snowy Mountains, as diagnosed by the position of the frontal cloud band and the geopotential thickness gradient, account for around 79% of all precipitation in the winter months. They are slightly more frequent for cut-off lows (occurring in 70% of cases) than for embedded lows (62% of cases). The proximity of the parent low to the region clearly plays an important role in this statistic, with numerous "near misses" as a cold front associated with an embedded low slips southward of the mountainous regions. Cut-off lows without a cold frontal passage near the Snowy Mountains are usually either in a decaying phase, or pass to the north of the region, but may still bring considerable precipitation.

Total precipitation per event is shown in probability distribution histograms in figure 3.4.

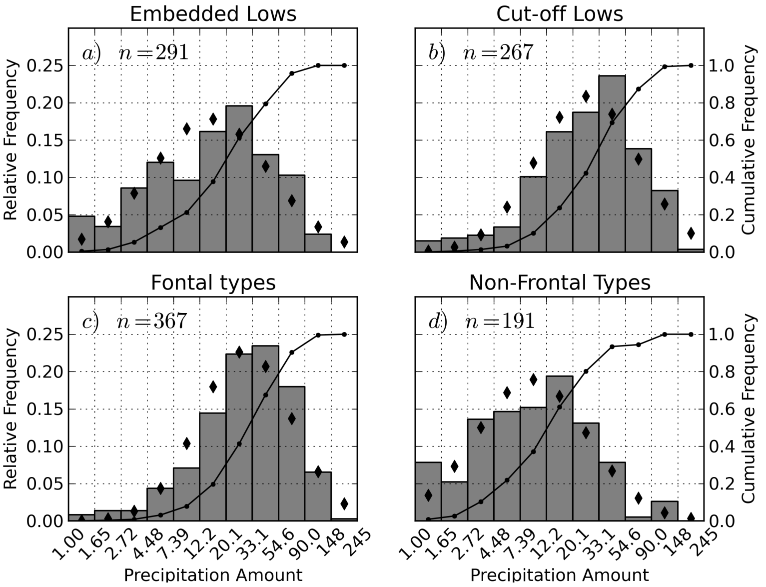

Figure 3.4: Probability histogram of precipitation amount (note logarithmically spaced bins), for the major synoptic types. The sigmoid shows the cumulative contribution of the bins, and the diamonds depict the log-normal distribution corresponding to the mean and standard deviation of precipitation amount.

The distributions are similar to log-normal distributions, which are shown by diamonds for distributions of the same mean and standard deviation as the precipitation totals. Negative skewness is especially evident in the distribution for frontal types, indicating that precipitation heavier than the mean amount is more important to the winter totals than light precipitation.

Cut-off lows tend to bring the heaviest precipitation, with one in four bringing more than 50 mm and one in ten bringing more than 100 mm. A cold frontal passage has significant impact on both the intensity and duration of precipitation. The median precipitation amount during a frontal passage is about 32 mm over 2.5 days, compared to 8.9 mm over 1.85 days for precipitation events in which a frontal passage does not occur.

Monthly contributions of each of the different system types are shown in figure 3.5. Cut-off lows show a peak in both frequency and total precipitation contribution in July, while embedded lows systems have a frequency peak in August–September and a precipitation contribution peak (relative and absolute) in August. In contrast, Pook et al. (2006) find the highest relative contribution of cold fronts in July, but the variability within the samples is very high for both studies.

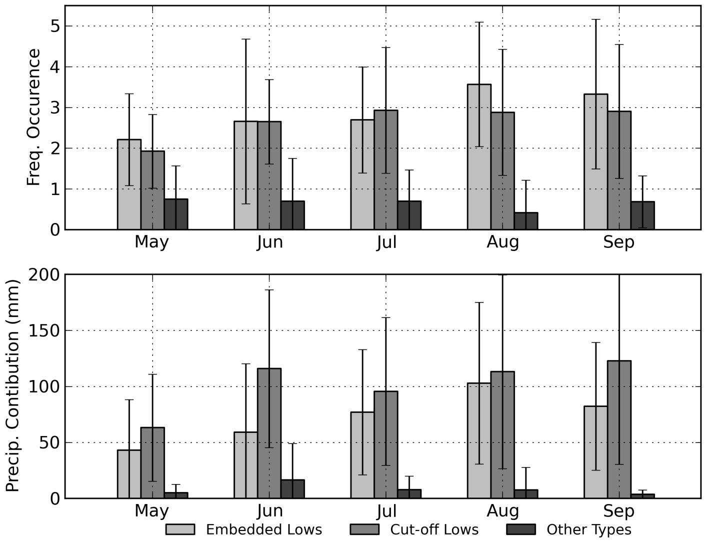

Figure 3.5: Frequency of occurrence (above), and precipitation contribution (below) of each type of precipitation event occurring during the winter months of 1990–2009. Error bars show one standard deviation.

3.3.2 Annual variability and trends

Year-to-year variations in the frequency of precipitation events and the total amount of precipitation brought by these are shown in figure 3.6 (Pook et al., 2006, c.f. figure 8). The attribution of precipitation to the two major synoptic types is reasonably consistent throughout the analysis period. More cut-off lows were diagnosed than embedded lows in eleven of the twenty years, and cut-off lows brought more precipitation in all but four years.

The number of precipitation events clearly plays a role in the amount of precipitation brought in a given year; of the three years with the least number of precipitation events, two of these (1994 and 2006) are the driest years on record. The correlation between the number of systems and the total wintertime precipitation is moderate ($r = 0.51$), but there is a weakly positive trend (not statistically significant) in the number of precipitation events per season, so the hypothesis that the declining trend in precipitation is caused by less frequent storms must be rejected.

The magnitude of the downward trend in total winter precipitation (discussed in the previous section) is the sum of the decline for both of the major synoptic types. The decline in precipitation due to cut off lows was found to be 18.1 mm per year, which in relative terms is

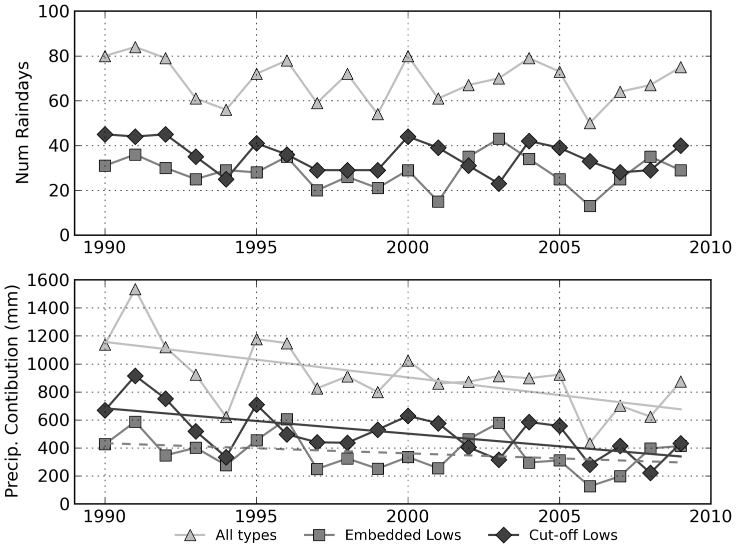

Figure 3.6: Number of occurrences (above) and contribution to wintertime precipitation amount (below) for the two major synoptic categories. Statistically significant trends are shown with solid lines.

about twice the value of the decline due to embedded lows. Only the decline in precipitation due to cut-off lows was statistically significant.

No trend in the frequency of cut-off lows was identified in the analysis, so it may be inferred that the amount of precipitation per event must have decreased to make up the decline. A slight, non-significant decline in the number of rain days per event was noted for both cut-off and embedded lows of -0.4 and -0.1 rain days respectively. However, the amount of precipitation per rain day (a measure of intensity) was noted to have declined by 0.34 mm and 0.20 mm, significant at the 1% level. These results clearly indicate that precipitation intensity has declined in the Snowy Mountains region, especially so for cut-off lows.

The same decomposition has been performed for the average daily precipitation from the network of 38 gauges on the lower western slopes, where a similar pattern was seen. For both synoptic types, the ratio of low-elevation to high-elevation decline was very close to 2.7; that is, the relationship between elevation and overall precipitation decline does not appear to depend on the synoptic types investigated.

The frequency of occurrence of frontal types was found to have decreased by 0.17 per year, amounting to a decline in 18% over the analysis period. Recent work (since the completion of this climatology) on the objective identification of fronts in global reanalysis data (Berry et al., 2011) verifies the high frequencies of fronts in the Southern Ocean storm track, but the trends in south-eastern Australia are positive (Berry, 2011), so the inference that frontal systems have slipped further to the south over the past two decades is not supported. However, the results of Berry et al. (2011) are not necessarily conflicting with the results of this climatology, which requires that precipitation be recorded for an event to be defined, and may in fact include more than one frontal passage in an event lasting several days. The occurrence of more frequent dry fronts would be a candidate explanation for the inconsistency here.

Chapter 4

Case studies of orographic influence on clouds and precipitation in south-eastern Australia

Wintertime precipitation in alpine regions makes a considerable contribution to water resources in south-eastern Australia, but the nature of the storms that bring this precipitation has not been extensively studied. Two typical wintertime precipitation events over the Brindabella Ranges, just to the north of the Snowy Mountains, are presented in this chapter to illustrate the potential importance of the role of orography in the life cycle of clouds and precipitation in the alpine environments. Surface observations from automatic weather stations operated by the Australian Bureau of Meteorology, as well as rain gauge data from an independent network, are used to characterise precipitation during these storms. Dual-channel microwave radiometer retrievals provide column-integrated liquid water and water vapour amounts at a mountain-top location, which are compared with MODIS level 2 cloud product data. High resolution numerical simulations are performed with the Weather Research and Forecasting (WRF) model to enhance the interpretation of the observations.

These events from the winter of 2008 have been chosen to coincide with available radiometer observations from Mt. Ginini,the location of a BOM AWS in the Brindabella Ranges. In section 4.1, the two precipitation events are defined within the context of a limited climatology

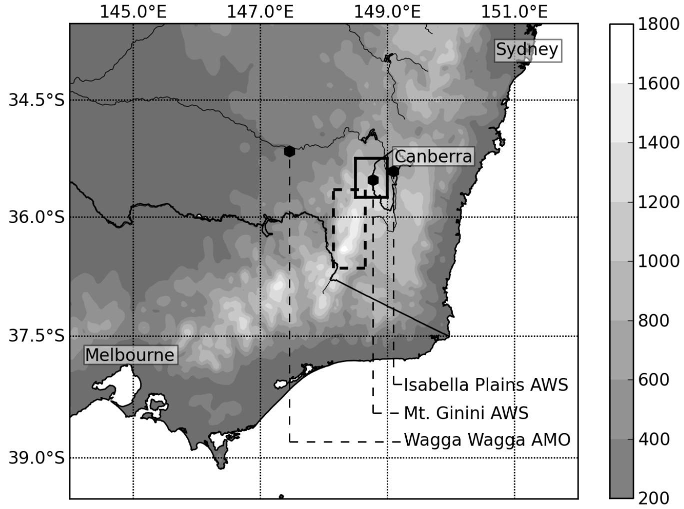

Figure 4.1: Map of south-eastern Australia showing topography of the GDR. The rectangle indicates the location of the Brindabella analysis region (see figure 4.2). For reference, the Snowy Mountains analysis region (chapter 6) is shown with dashed lines. The three AWS locations discussed in text are indicated by the black markers.

of south-eastern Australia. In section 4.2 the observations are presented with specific focus on cloud cover and surface precipitation. In section 4.3, numerical simulations of these events made with the WRF code are discussed and evaluated against the earlier observations.

4.1 Analysis region, data and methods

4.1.1 The Brindabella Ranges and catchment area

The Brindabella ranges lie some 30 km to the west of Canberra and form the northern end of the Australian Alps (figure 4.1). The mountain range forms the western border of the Australian Capital Territory, and the catchment areas in the region supply about 85% of the water of Canberra's water. The highest point of this range is Mt Bimberi, reaching 1912 m above sea level, and the ranges are somewhat less elevated than the Snowy Mountains to the south west. Nevertheless, the terrain in the region is interesting for the study of orographic precipitation, as a substantial section of the main range is oriented north-south and is raised above the surrounding area (figure 4.2).

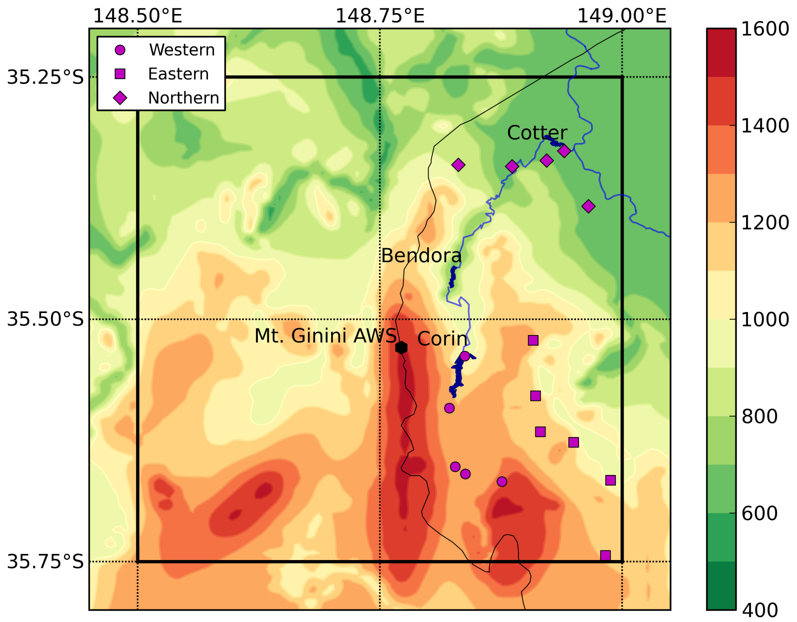

Figure 4.2: Map of Brindabella region (expanded section from figure 4.1), from gridded topography used to force the numerical simulations. The ACTEW AGL precipitation gauges are shown by small markers, and locations of the Canberra reservoirs are also shown.

4.1.2 Surface meteorological measurements

Measuring precipitation in an alpine region is highly challenging given its sensitivity to the local orography. This challenge is even greater during the winter when the precipitation falls as snow or ice in strong winds, especially in alpine environments where precipitation gauges networks tend to be too sparse to adequately represent the spatial patterns in precipitation. A Bureau of Meteorology AWS is located atop Mt Ginini (148.77° E, 35.53° S; 1760 MSL), and is equipped with a heated tipping bucket precipitation gauge, providing measurements of both frozen and liquid precipitation. In addition to the AWS, an independent network of 16 unheated rain gauges is operated by ActewAGL to estimate catchment inflows. These are broken into three groups based on location, as depicted in figure 4.2.

To characterise broader-scale development of precipitation during the case study events, AWS data from Wagga Wagga AMO (125 km to the west), and Isabella Plains (31 km to the east in suburban Canberra) are also presented.

For the winter of 2008, a dual channel microwave radiometer (Westwater, 1978) providing one-minute column integrated liquid water and water vapour measurements was intermittently operated by ActewAGL at a site co-located with the Mt Ginini AWS.

4.1.3 Upper air data and remotely sensed measurements

The closest regular upper-air soundings are made twice daily from Wagga Wagga, some 125 km west of Mt Ginini. These data are presented below to show the atmospheric profile during the case study events, and to evaluate the timing of the WRF numerical model results.

The Moderate Resolution Imaging Spectroradiometer (MODIS) instrument is located on two of the NASA Earth Observing System satellites in sun-synchronous orbit, and passes over the Brindabella region about four times per day. The MODIS Level 2 Cloud Product (Platnick et al., 2003) includes a cloud water path variable derived from visible and infra-red radiances. To compare with the microwave radiometer column-integrated liquid water path, statistics of values in a small domain ($0.25° \times 0.25°$) centred on Mt Ginini are presented in this analysis.

4.1.4 Back trajectory modelling

Back trajectories are a useful tool in identifying the source of the air mass affecting a given region, and can give insight into the dynamics and the aerosol loading of the atmosphere. Trajectories arriving above the radiometer site at Mt Ginini (35.53° S, 148.77° E) were computed at hourly intervals with the use of the NOAA Air Resources Laboratory Hybrid Single-Particle Lagrangian Integrated Trajectory (HYSPLIT) model (Draxler and Hess, 1998a). These back trajectories were computed using three-hourly Mesoscale Limited Area Prediction System (MLAPS) forecast output over a 0.125° latitude-longitude grid, produced by the Australian Bureau of Meteorology.

4.1.5 Numerical simulation of case studies with the WRF model

Numerical meteorological model output, carefully interpreted, can give a richer understanding of physical processes that may not be directly observed. In particular, observations of cloud structure are limited during these case study periods. The microwave radiometer gives high frequency point values for column-integrated liquid water, whereas the MODIS instrument provides spatially dense observations of this parameter very infrequently. One of the motivations of this modelling study is to reconcile the observational paucity of cloud variables with simulated data.

The model was forced by boundary and initial conditions derived from the Global Forecast System operational analysis, which were obtained on a $1^\circ \times 1^\circ$ grid, and processed with the standard WRF preprocessing system (WPS).

Numerical simulations of the meteorology for the case study were performed using the non-hydrostatic Advanced Research WRF (ARW) version 2.2.1. The model configuration was of five telescoping domains, with the outermost domain (approx 110 km grid spacing to match the resolution of the initial condition data) covering the Australian continent and a large portion of the Southern Ocean north of 50° S, so as to directly simulate the large-scale synoptic features driving the weather in the Brindabella Ranges. The innermost nest was centred on Mt Ginini and had a grid spacing of 1.35 km, with a model time step of three seconds. There were 64 model levels, using the hybrid σ coordinate, which follows terrain at low levels and pressure levels higher in the atmosphere.

The physics options selected for these simulations are typical choices for mid-latitude meteorology in complex topography. Notably, the planetary boundary layer scheme used was the Mellor-Yamada-Janjic scheme (Mellor and Yamada, 1982), and the cloud microphysics scheme used was the Thompson microphysics (Thompson et al., 2004). Cumulus parametrisations which represent convection on sub-grid scales, were not used on the inner domains of the simulation as the resolution was sufficient to explicitly model these processes.

The choice of microphysics scheme probably has the largest impact on simulations of precipitation in complex terrain during wintertime storms such as the two case studies selected. The Thompson scheme has been developed specifically to perform well in these conditions (Stoelinga et al., 2003). It is a bulk microphysics scheme, in that it does not directly predict distributions of hydrometeor size. It is double moment for cloud ice, predicting both mass and number concentrations for these hydrometeors, and single moment for cloud water, rain, snow and graupel, predicting only mass concentration. To represent aerosol loading of the atmosphere, the user specifies a Cloud Condensation Nuclei (CCN) concentration at compile time. The value selected for this parameter was 150 cm^{-3} reflective of the generally cleaner nature of the southern hemisphere airmass (Boers and Krummel, 1998)

The simulations were initialised at 12:00 UTC on the first day of each of the case studies, leaving a spin-up period of at least 6 hours before the first precipitation observations. They were run for a total of 60 hours, although only the first 36 hours of simulation are presented here. The diagnostics performed from the model output include:

- Simulated surface precipitation measurements in the Brindabella region at the model grid points closest to the physical locations of the gauges; Simulated soundings for comparison with Wagga Wagga upper air data;
- Diagnosis of total liquid water path at the grid point nearest Mt Ginini for comparison with microwave radiometer observations, as well as with MODIS cloud water observations.

4.2 Description of case studies

4.2.1 19-21 July case study

The July case study is largely defined by a strong cut-off low that travels quickly across south-eastern Australia. The cut-off low has a strong cold front associated with it that passes over the Brindabella catchment early on 20 July. The heading of the surface wind shifts strongly with the frontal passage but it takes roughly a day before the post-frontal air mass may be characterised as having an origin over the Southern Ocean. During most of this transition period substantial orographic precipitation is observed at the highest elevations.

Synoptic description and satellite imagery

The cold-cored cyclone in the Great Australian Bight 4.3 moves eastward and passes just to the south of the continent, reaching a minimum central pressure of 990 hPa. The surface minimum stays within the latitude band of 35°–45° S, and closed circulation is apparent throughout the lower troposphere, making this storm a classic example of a “cut-off low”, as

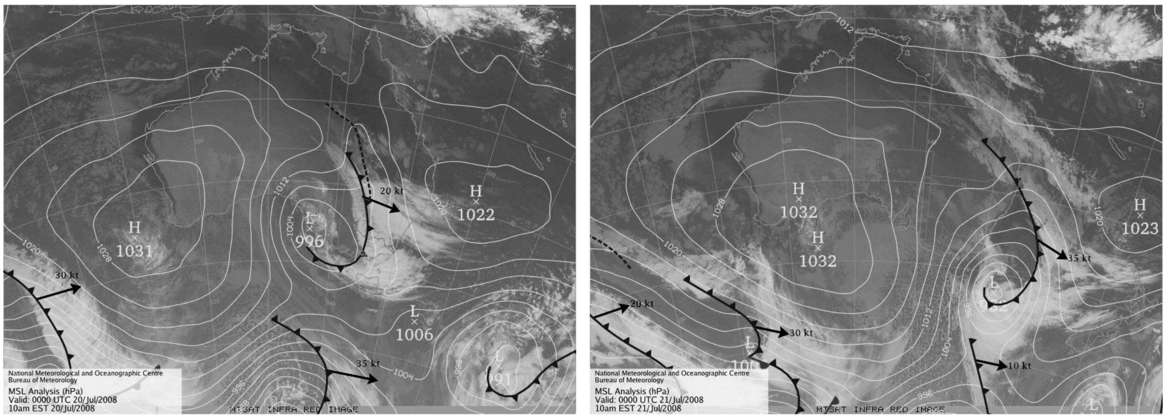

Figure 4.3: Mean Sea-Level Pressure (MSLP) manual analyses, overlaid on MTSAT-1R infrared imagery, for July case (00 UTC on 20 and 21 July 2008). Images are copyright of the Australian Bureau of Meteorology.

described by Pook et al. (2006). A well-defined frontal cloud band extending into the subtropics, and a dry slot can clearly be seen in the GMS IR satellite imagery (figure 4.3). A pre-frontal trough is apparent in the MSLP analysis while the front passes over south-eastern Australia. Following the passage of the front over the GDR, persistent low-level cloud is apparent in the satellite image for 00:00 UTC on 21 July. The low pressure centre does not make landfall, but weakens considerably as it approaches the southern coast of the continent. It subsequently re-intensifies as it passes over the warmer Tasman Sea to the south-east.

Surface observations

Mountain-top AWS observations at Mt Ginini show a gradually increasing temperature overnight on 19 July, reaching a maximum of 3.5° C at 01:00 UTC (11:00 AEST; figure 4.4), with sustained wind speeds of up to 12 $\mathrm{m\,s^{-1}}$ from the north. The structure of the frontal system is quite complex as it passes the Brindabella region. The wind strength and direction observations for Mt Ginini (not shown) do not display a distinct change as they do for the lower sites. A gradual decrease in surface temperature begins after about 01:00 UTC, coinciding with a lull in wind speed but not a perceptible shift in wind direction. Precipitation commences at about 04:00 UTC, but the main wind and temperature changes do not occur until 07:30-09:30 UTC. These changes are still relatively gradual, with surface temperatures decreasing by 3.0° C over nearly four hours, accompanied by a similarly gradual decrease in wind speed to about 7 $\mathrm{m\,s^{-1}}$ and south-westerly shift in direction. Precipitation moderates

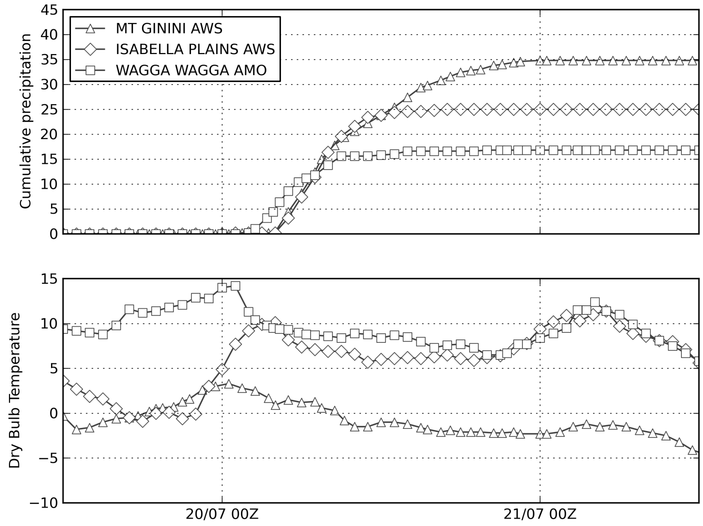

Figure 4.4: Cumulative precipitation amount (above) and temperature (below) from AWS observations during the July case.

to about 1.5 mm hr^{-1} after the frontal passage and persists until 23:00 UTC. A total of about 35 mm is recorded at the Mt Ginini AWS.

Figure 4.4 also shows the development of precipitation across the ranges during the case study period. Precipitation is first recorded at Wagga Wagga at about 02:00 UTC, and the onset of precipitation at Mt Ginini occurs two hours later, almost simultaneous with the first recorded precipitation at Isabella Plains. The precipitation rates for the first four hours after onset are quite similar, with about 12 mm recorded at Wagga Wagga and 18 mm and 16 mm recorded at Mt Ginini and Isabella Plains respectively. Wagga Wagga receives intermittent precipitation, totalling about 16 mm after this time, while at Isabella plains precipitation continues to a total amount of about 25 mm by 13:00 UTC, or nine hours after precipitation commenced. The precipitation during the 12-15 hours after the frontal passage is significant at Mt Ginini. A total of 35 mm was recorded over about 20 hours, with roughly half of this amount falling in the first four hours and the remainder at a slower rate during the extended post-frontal period. As the accumulations during the initial period were about the same at each of the three AWS sites, orography did not play a substantial role in governing the precipitation amounts during the frontal passage, but dominated in the post-frontal period.

The onset of precipitation at Wagga Wagga and Isabella Plains roughly coincided with the

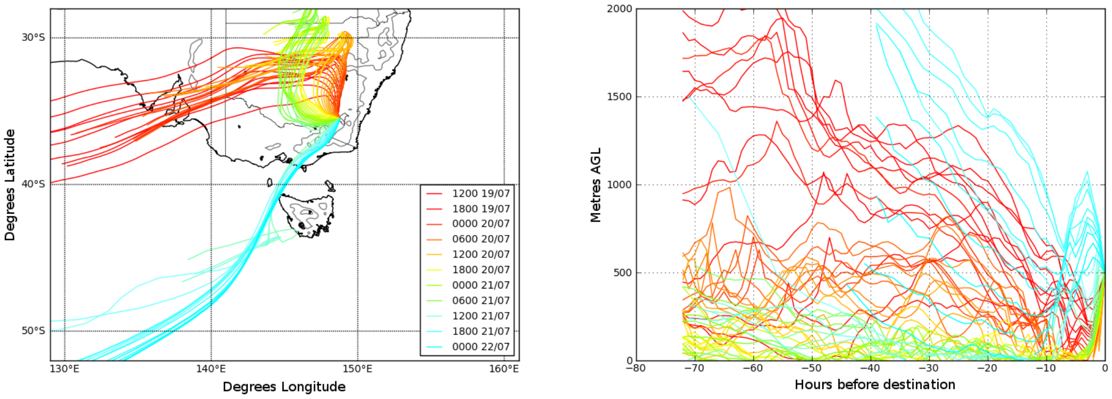

Figure 4.5: 72 hour HYSPLIT Back Trajectories at hourly intervals for the August case (12 UTC 19 July onwards). The back-trajectories arrive at Mt. Ginini at an elevation of 500 m AGL, and are coloured according to arrival time at Mt Ginini (warm colours earliest). Grey contours are terrain elevations at 500 and 1000 m.

passage of a distinct surface front, as diagnosed by the other surface variables, but surface variables at Mt Ginini suggest a much more gradual change. This gives some insight into the vertical structure of this cold front, which very likely has a more gently-sloping profile at the elevation of the Brindabella ranges.

Back trajectory analysis

The back trajectories depicted in 4.5 for the July case are coloured by arrival time, with the earliest arrivals in warm colours. The first air parcels to arrive during the case study period had been transported inland after the previous frontal system on 18 July (note the subsidence in the profiles). These are directed southward in a jet-like fashion with the approaching frontal system of the July case study. The air mass history does not change immediately with the passage of the cold front. The direction of arrival at Mt Ginini shifts from northerly to westerly with the frontal passage, and arriving parcels have spent their recent history low in the atmosphere. The majority of the recorded precipitation is associated with these trajectories, which have also spent most of their time over western New South Wales. It is not until nearly 24 hours after the frontal passage, and well after the cessation of precipitation, that the history of the air mass becomes truly “maritime“ in nature. By 06:00 UTC on 21 July, parcels are approaching quickly over the Southern Ocean, and subsiding strongly.

4.2.2 09-12 August case study

The August case study is largely defined by a weak cut-off low that travels quickly across south-eastern Australia. A weak, poorly defined frontal system is associated with this low and produces a relatively weak precipitation event. The slow moving front passes over the Brindabella catchment between 21:00 UTC 09 August and 01:00 UTC 10 August. The wind and temperature changes are quite weak during the passage. Much of both the pre-frontal and post-frontal air has spent recent time over the Southern Ocean.

Synoptic description and satellite imagery

The August case study begins with a much weaker cut-off low (figure 4.6) with a central pressure of 1012 hPa, located at about 42° S below the western border of Victoria, with a strong ridge over the centre of the continent. The low pressure system is complex in nature, with multiple short-lived pressure centres and weaker cold fronts appearing in the preceding analyses. Closed circulation is evident at the 500 hPa level, but is less distinct than for the previous case study. As in the previous case, the cyclone becomes more coherent and deepens rapidly once it reaches the Tasman Sea. The frontal cloud band associated with this system is much less well-defined than for the July case study, and does not extend nearly so far north. Extensive low cloud is again apparent over the elevated regions of the Great Divide well after the passage of the front. Patchy cumuliform clouds are apparent in the region behind the frontal systems.

Surface observations

A weak change is evident in the AWS observations (figure 4.7). Short-lived precipitation at Wagga Wagga commences at about 19:00 UTC on 09 August (05:00 AEST 10 August), probably with the passage of a weakly-defined front, and the main front passes shortly after 00:00 UTC on 10 August, bringing intermittent precipitation to a total of about 5 mm. This sequence of events is mirrored by Mt Ginini, where a brief period of precipitation (bringing about 6 mm) occurs at 22:00 UTC, coinciding with a weak wind direction change of about 30° (not shown). A later cool change and another brief period of precipitation start at about

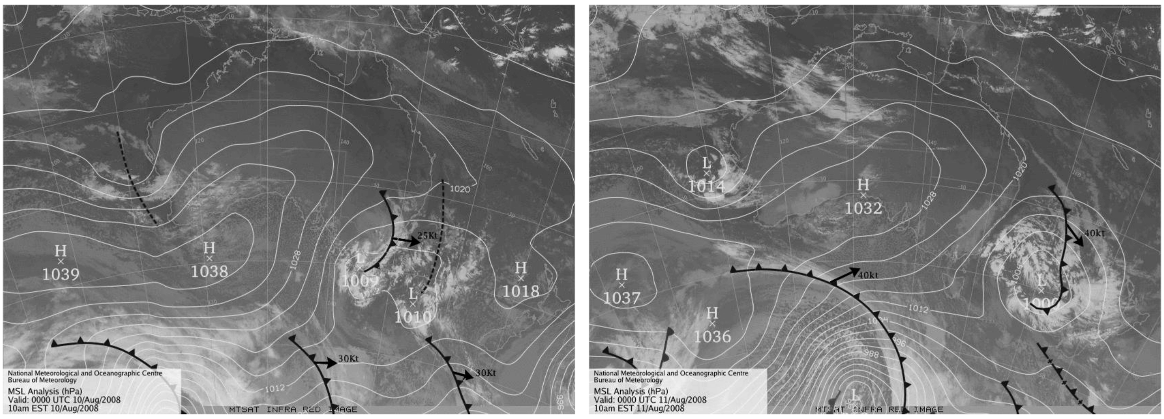

Figure 4.6: As for figure 4.3, but for August case (00 UTC on 10 and 11 August 2008). Images are copyright of the Australian Bureau of Meteorology.

03:00 UTC, bringing a further 7 mm of precipitation. Intermittent precipitation occurs for the following 10 hours or so, bringing a further 3 mm of precipitation to a total of 16 mm for the event. Only trace precipitation is recorded at Isabella Plains, coinciding with the initial wind change, and the eastern region is apparently cloud-free for much of the case study (note the distinct diurnal cycle for temperature at Isabella Plains in figure 4.7).

Conditions during the August case were substantially cooler than for the July case. Ambient temperatures atop Mt Ginini were in the region of −4.0 to −6.0° C for the August case, as compared to the range +3.0 to −2.0° C for the July case.

Back trajectory analysis

HYSPLIT back trajectories during the weaker frontal passage (figure 4.8) display a very different picture from the July case study. There is little variation between pre-frontal and post-frontal trajectories due to the presence of a strong, well-defined ridge across central Australia. Pre-frontal trajectories have arrived relatively slowly over the previous three days, passing over south-western NSW. Following the frontal passage, the trajectories become longer as the average speed increases, and air parcels have histories over the Great Australian Bight. As the low pressure centre progresses and passes to the south of the region, the air mass history becomes more southerly in nature, and remains so for the duration of the case study period. Air parcel elevations remain low for all trajectories, except for a brief period during the transition between the westerly and southerly regimes.

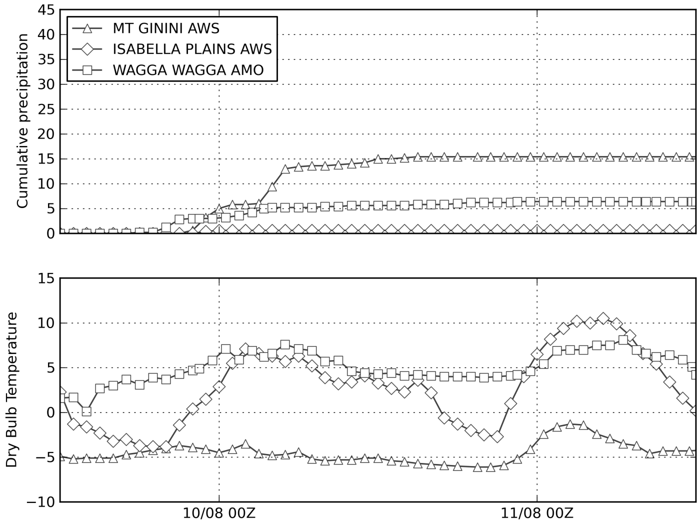

Figure 4.7: As for figure 4.4, but for the August case.

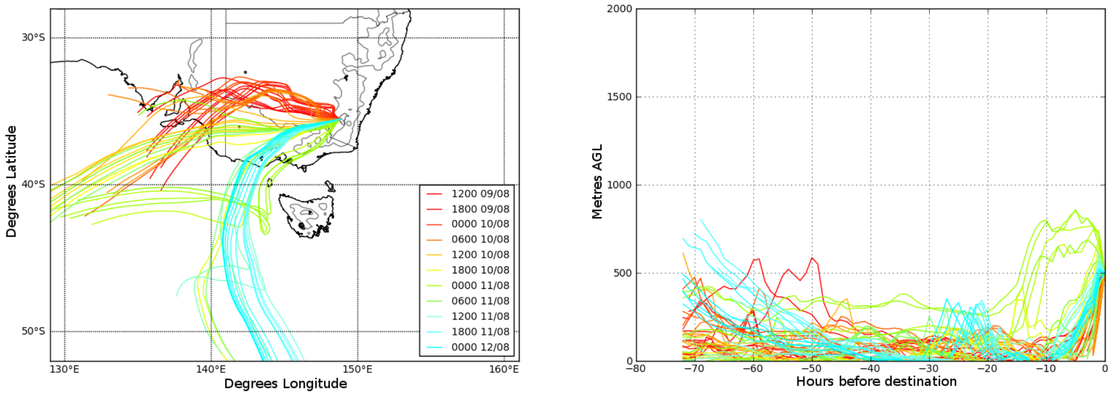

Figure 4.8: As for figure 4.5, but for the August case (12 UTC 09 August onwards).

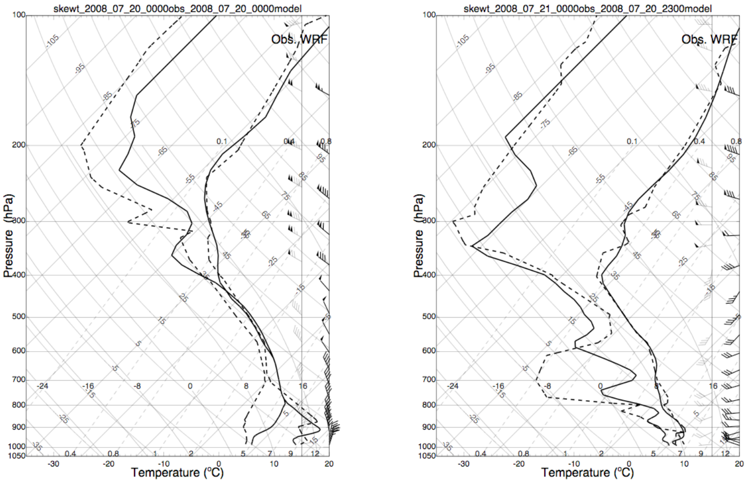

Figure 4.9: WRF simulated upper air soundings (solid lines) alongside the observations (dashed lines) for the July case. Soundings are taken at 00 UTC on 20 and 21 July. The WRF soundings are at 00 UTC on 20 July and 23 UTC on 20 July.

4.3 Evaluation of numerical simulations

4.3.1 Upper air comparisons

The representation of the atmospheric profile simulated by the WRF model is compared directly to the 00:00 or 12:00 UTC Wagga Wagga soundings (depending on availability) for the July case in figure 4.9, and the August case in figure 4.10. To identify any lag or lead in the simulations, the best-matching simulated soundings are selected for comparison. The sounding for 21 July is most closely matched by the simulation time 23:00 UTC on 20 July, indicating a lead of about an hour at this time. For the August case, the best-matched profile for the 12:00 UTC sounding on 10 August is about two hours ahead.

The simulated profiles are otherwise very similar to the Wagga Wagga sounding for both cases, both in the temperature profile and the wind profile. The simulations capture a realistic Eckman-type spiral in the lowest layers, and wind speeds are generally well represented in the upper levels. The 00:00 UTC sounding on July 20, launched while the deep frontal band was overhead, is well-represented by WRF, with very similar wind and moisture profiles. By 00:00 UTC on 21 July, the clearly different air mass (note the wind barbs and temperature changes) is also well-represented, although the sounding indicates drier air in the mid-levels. The low- to mid-level (below 700 hPa) dryness and stable temperature profile at this stage

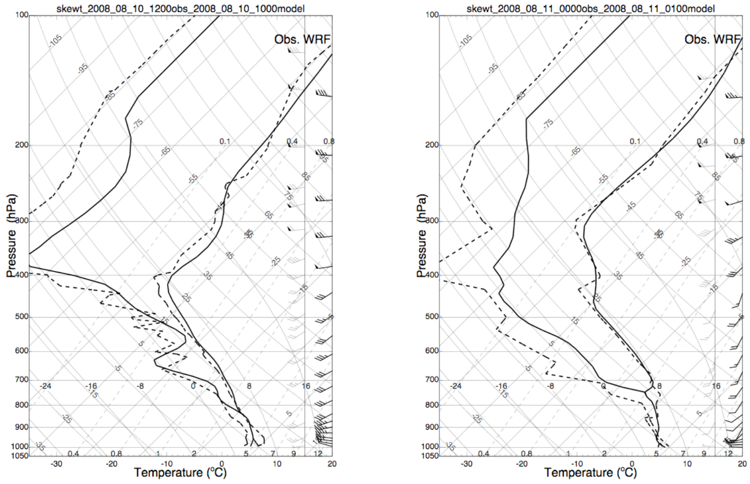

Figure 4.10: As for figure 4.9, but for the August case. Soundings are taken at 12 UTC 10 August and 00 UTC 11 August. The WRF soundings are at 10 UTC 10 August and 01 UTC 11 August.

are inhibitive to cloud development, so orographic forcing is the dominant mechanism for cloud and precipitation formation.

The most interesting sounding for the August case is the 12:00 UTC sounding on 10 August. This sounding is released some 12 hours after the frontal passage, and the air mass is of moist, post-frontal character, with moderate-strength south-westerlies, and a dry band above 700 hPa. The subsequent sounding (00:00 UTC on 11 August) suggests drying of the mid-troposphere, but cloud development is still possible up to 700 hPa. Both of these are remarkably well represented by the WRF simulations, albeit with a two hour lead and a one hour lag, respectively.

4.3.2 Surface precipitation

Direct comparisons of modelled precipitation with point observations is a fairly hopeless task, especially in situations with complex topography. High spatial variability of precipitation is commonplace, necessitating dense networks of gauges, and even at model resolutions approaching 1 km, the terrain is not adequately represented in mountainous regions. Further still, reliable observations of precipitation in alpine regions are difficult to perform, requiring specialised equipment to record frozen precipitation and to minimise under-catch due to high winds. It is difficult to even begin to assess the errors associated with such measurements.

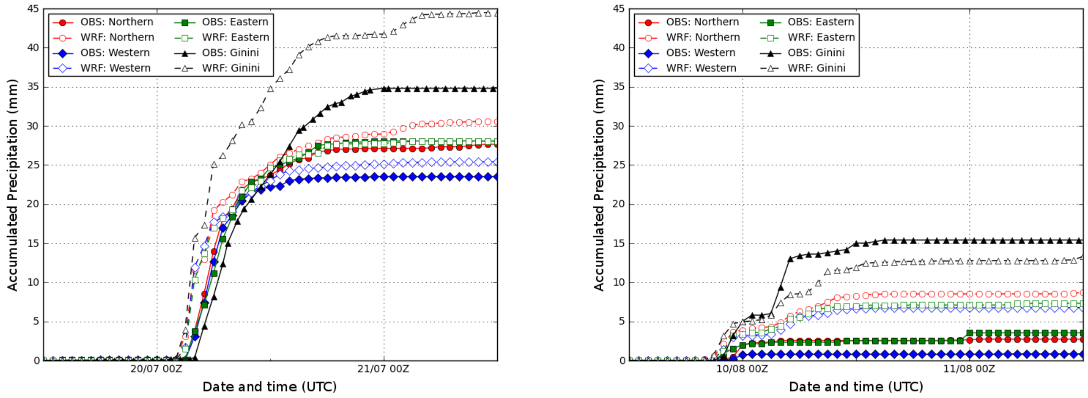

Figure 4.11: Observed and simulated precipitation for the Mt Ginini AWS and the three groups of gauges operated by Actew AGL. July case (left) and August case (right).

The comparisons made between the modelled and observed surface precipitation for these case studies (figure 4.11) are, in this light, quite favourable. The network of 16 precipitation gauges operated by ActewAWL has been divided into three groups based upon location (Northern, Western and Eastern) for these comparisons, and the average of each group is presented. Observations from the Mt Ginini gauge are compared directly to the model output from the closest grid point.

For the July case study, modelled precipitation commences up to two hours ahead of the observations, consistent with the lead identified in the upper air structure. Precipitation is slightly overestimated for all three groups, and especially so at Mt Ginini, where 44 mm of precipitation is predicted over the course of the event. Most of the over-prediction occurs during the initial heavy precipitation; the post-frontal precipitation rates are about the same.

In the August case, simulated precipitation again leads the observations at Mt Ginini consistently with the upper air comparisons. Precipitation simulations for the initial showers are close, but in this case the WRF model under-predicts the post-frontal precipitation. For this case, none of the three ActewAGL groups record substantial precipitation, whereas WRF predicts at least 7 mm for all groups. This is most likely due to snow accumulation in the gauges; conditions were much colder during this event and precipitation falling at these sites would have been primarily frozen during this period. Examination of the precipitation record for the individual gauges shows accumulations at several gauges around 00:00 UTC (10:00 AEST) on 11 August (not seen at Mt Ginini), which are most likely snow melting with the

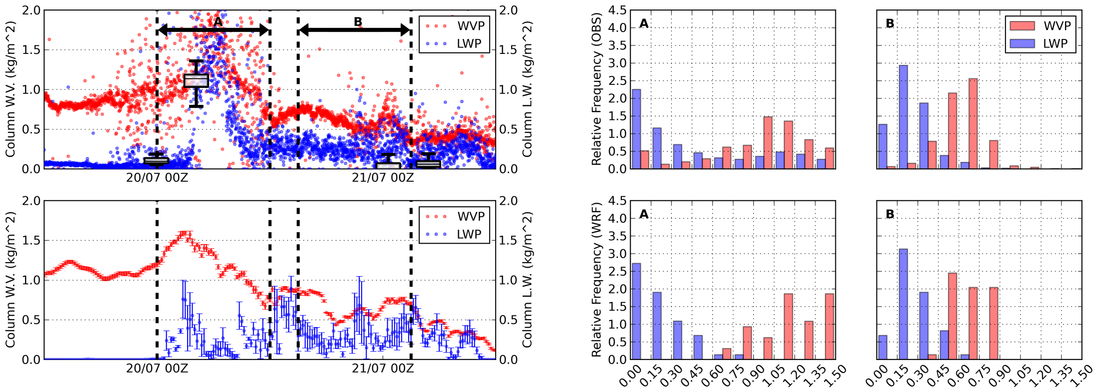

Figure 4.12: Observed (top row) and simulated (bottom row) radiometer measurements. The leftmost panels are time series values, and the histograms on the right show probability distributions for different observations/simulations for the indicated 12-hour intervals. Statistics for MODIS observations of cloud water path for a 0.25° box centred on Mt Ginini are represented by the box plots over the observed time series (90th percentiles shown by whiskers).

onset of solar heating.

4.4 Insights into cloud structure during wintertime storms

Cloud liquid water path (LWP) and water vapour path (WVP) can be evaluated by measuring atmospheric brightness temperature at a pair of frequencies in the microwave band (Westwater, 1978). These are selected to coincide with the peak absorptivity and the window region for water vapour (around 22.2 and 30 GHz respectively), and from the differences in the absorptivity at these frequencies the column integrated values can be determined. Cloud LWP and WVP above Mt Ginini have been calculated in this manner and are displayed for the two case studies in the upper panels of figures 4.12 and 4.13. Also plotted over the time series are box plots of the available data from the MODIS overpasses, showing the cloud LWP median and interquartile range, as well as the 90th percentiles, for the 0.25° box centred on Mt Ginini.

For the simulations, vertically integrated values for liquid water and water vapour are calculated for liquid hydrometeors (cloud water and rain), and water vapour at the nearest grid point, and are shown in the lower panels of figures 4.12 and 4.13. The values were calculated from both the model terrain elevation (about 1440 m) and from the lowest grid cell above

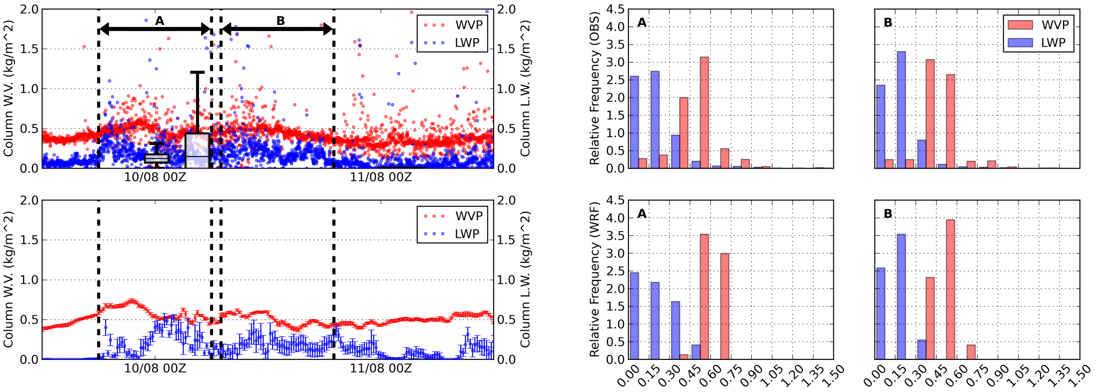

Figure 4.13: As for Figure 4.12, but for the August case.

the actual elevation of the radiometer location (1760 m), to give the lower and upper bounds shown. Finally, the distributions of observations and simulated values of WVP and LWP for two 12-hour periods are shown in the right hand panels of figures 4.12 and 4.13.

4.4.1 July case study

For the July case, increasingly high values of WVP are observed until shortly after the frontal passage, coinciding with a period of high LWP values (around 1.4 $\mathrm{kg\,m^{-2}}$), as well as the highest surface precipitation rates at Mt Ginini. Droplet collection on the radiometer microwave window during heavy rainfall is a known cause of erroneously high values for LWP, but good agreement is nevertheless shown between the surface-based and MODIS retrievals for this period. However, this comparison is treated cautiously as the MODIS-retrieved value is for total cloud water (ice and liquid), and high concentrations of ice are expected within the frontal band.

An alternative explanation for the discrepancy between the observed and simulated LWP values is that the microphysics scheme of the WRF model may be simulating the production of precipitation too rapidly during this period through conversion of liquid water to ice hydrometeors, which would explain both the lower LWP amounts as well as the higher precipitation rate during the onset of precipitation.

The statistics during the two indicated 12-hour intervals differ in accord with the different dynamic phases of the storm. The first period is roughly centred on the time of the frontal

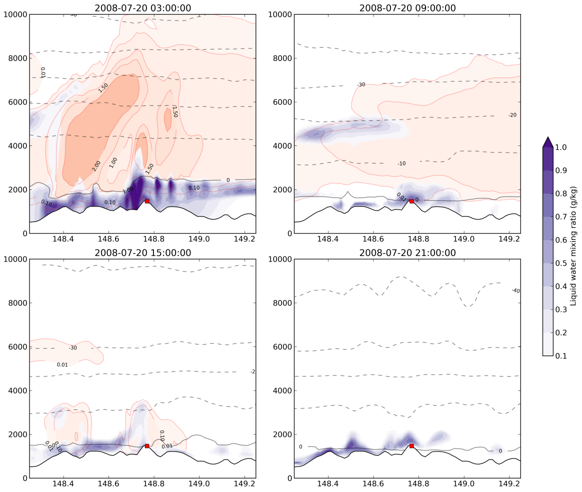

Figure 4.14: Cross sections along a parallel through Mt Ginini (small square) showing modelled cloud structure for the July case study. The total liquid water content (cloud water and rain) is shown by shades according to the scaling on the right of the image. Frozen water content (ice, graupel and snow) are contoured at 0.01, 0.1, 1.0, 1.5 and 2.0 $\mathrm{g\,kg^{-1}}$ (red filled contours). Altitude is shown by the y-axis, and air temperature in 10°C intervals (dashed contours are negative values).

passage, and the modal value for observed WVP is about 1.0 $\mathrm{kg\,m^{-2}}$. There is a bi-modal characteristic to the observed LWP due to the high values observed during the frontal passage. During the second 12-hour interval, LWP values in the region of 0.15–0.3 $\mathrm{kg\,m^{-2}}$ are the most frequently observed. In general, the WRF simulations of WVP show a good temporal relationship with the observations. The statistics for the simulations show that the WRF model tends to overestimate WVP and underestimate LWP in the earlier interval, most likely because of the discrepancies near the frontal passage. Later in the simulation the values for both WVP and LWP show relative agreement. The tails of the distributions are generally not well-represented, but this is likely to be caused by under-sampling from the model as the cloud fields are only output on 15 minute intervals.

The complexities of the mountainous terrain and the subtleties of orographic cloud formation make it extremely difficult to represent individual clouds in numerical simulations, but the similarities in the cloud field statistics in the second interval suggest that the WRF model is at least simulating the same "population" of clouds. This result, combined with the generally good representation of surface precipitation, suggests that the Thompson et al. (2004) microphysics is well-tuned for the simulation of orographic precipitation in this environment, an encouraging result for further research in Australian alpine precipitation.

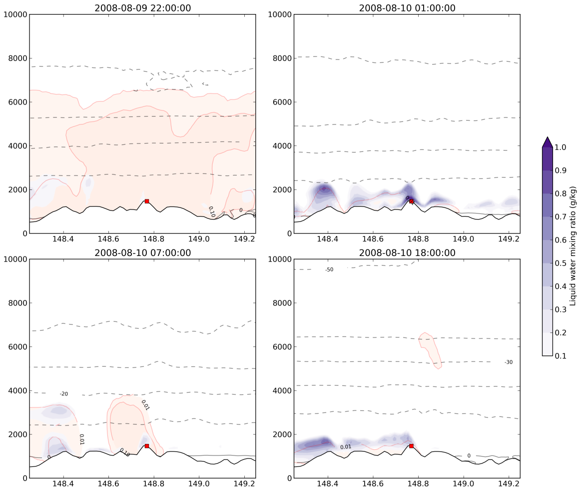

Figure 4.15: As for figure 4.14, but for the August case study.

Vertical cross sections of the simulated cloud fields, showing total mass concentration of liquid and frozen hydrometeors, are shown in figure 4.14. Near the frontal passage at Mt Ginini (cross sections at 03:00 and 09:00 UTC), very little liquid water exists above the 0° C isotherm, suggesting that ice processes are dominating, as might be expected from such a deep, mature frontal band. Later in the simulation (15:00 and 21:00 UTC), where the LWP values are better matched to the observations, simulated cloud fields are clearly orographic in nature with the highest LWP amounts linked to the most prominent peaks.

4.4.2 August case study

The August case study is characterised by lower observed WVP values (typically 0.3–0.5 $\mathrm{kg\,m^{-2}}$), which, together with the lower wind speeds for this event, suggest that the water vapour flux for this case was lower. There is little variation over the course of the case study period, corresponding to the weaker dynamical forcing in this case. Cloud LWP values are lower than for the July case, but also highly variable, reaching above the background level of 0.05 $\mathrm{kg\,m^{-2}}$ shortly before the frontal passage, and persisting for about 30 hours. MODIS retrievals again show very good agreement with the radiometer near 00:00 UTC, but for 04:00 UTC there is very high spread in the satellite data, reflecting the variability on small scales of the cloud in this mountainous region.

The simulated WVP again tracks the observations quite closely, although there is a systematic bias of about 0.1 $\mathrm{kg\,m^{-2}}$, or about 20%, corresponding to the rightward offset between the observed and simulated distributions in figure 4.13. The simulated cloud LWP values do not follow the observations temporally, but the cloudy duration at Mt Ginini is about the same, and the distribution of simulated values is quite good for both of the 12-hour periods, so it may be inferred that the cloud "populations" are again well-represented.

Cross sections through the simulated data for the August case (figure 4.15) show a much less intense frontal band over Mt Ginini at 22:00 UTC (about the time of the onset of precipitation). By 01:00 UTC, the deep cloud has moved eastwards, and the remainder of the simulation is characterised by shallow cloud with tops below 4000 m. Liquid water persists below 0°C to the west of the ranges for a significant portion of the simulation, with a clear correspondence between cloud water maxima and topographic peaks during this later period.

4.5 Summary

A detailed interpretation of the available observations during two typical wintertime storms has been presented. High resolution numerical simulations with the WRF model match the observations remarkably well and have been used to provide a more complete picture of the nature of these storms. The two events offer some contrast in that the July event was characterised by a strongly dynamic cut-off low, while the August event was a weaker, less well-organised system with a complex of frontal bands. Both events were followed by an extended post-frontal period, characterised by shallow, liquid phase clouds and light precipitation sustained for at least 12 hours.

In both of the case studies, total precipitation amounts recorded at Mt Ginini were approximately double those recorded at Wagga Wagga, consistent with the climatology of monthly precipitation for these sites for winter (May–September) of the years 2004–2010. The duration of precipitation was longer at the mountain-top site, where post-frontal orographic uplift plays an important role. Precipitation at Isabella Plains appears to be controlled by the orography upwind of the site, as it is located in the rain shadow of the Brindabella ranges.

4.5.1 Frontal precipitation

The majority of precipitation in both cases is coincident with the approximate time of the cold frontal passage. Differences in the timing of the frontal passage can be identified by the onset of precipitation at the three AWS sites. For the stronger front (the July case), initial precipitation rates at each of the three AWS sites were very similar, indicating that the role of orography was negligible. This is contrasted with the August case, where the precipitation rates at Mt Ginini were at least twice those at Wagga Wagga for both periods of substantial precipitation, and only trace amounts of precipitation were recorded at Isabella Plains. More precipitation was recorded at Mt Ginini than at Wagga Wagga in the August case as a result of orographic enhancement of precipitation intensity during the frontal passage.

4.5.2 Post-frontal precipitation

For both events, the duration of post-frontal precipitation was found to be considerably longer in the Brindabella ranges than either the upwind or downwind lower-lying regions. For the July case, moderate precipitation rates (~ 1 mm hr^{-1}) persisted for up to 20 hours after the onset of precipitation, compared to 5–6 hours at Wagga Wagga, and 6–8 hours for Isabella Plains. During this extended post-frontal precipitation period, precipitation at the lower sites was negligible, while at Mt Ginini a further 10 mm (nearly 30% of the total) was recorded. The additional precipitation was clearly also orographically forced, but the mechanism appears in this case to be the forced uplift of stable moist air over the mountain range.

In the August case, the extended post-frontal precipitation at Mt Ginini brought only an additional 2 mm of precipitation, or about 15% of the total, and was apparently less important to the total precipitation amount. Very little precipitation was recorded at the ActewAGL gauges after the frontal passage, but these data were considered unreliable for this case study as snow was deduced to have accumulated in the unheated gauges. The WRF model, on the other hand, simulates gradual accumulation of precipitation at Mt Ginini, as well as for the other sites, for some 10–12 hours after the frontal passage to account for about half of the total accumulate precipitation. No post-frontal precipitation was recorded at Isabella

Plains, suggesting that the Brindabella effectively casts a rain-shadow during these post-frontal westerly conditions.

4.5.3 Cloud structure

Path integrated values of water vapour and liquid water were measured from the surface with a dual band microwave radiometer, and from space with the MODIS instrument. The microwave radiometer technology has been available for some time, and was used in the nearby Snowy Mountains during a field campaign to assess the region's suitability for conducting a cloud seeding experiment (Warburton and Wetzel, 1992), as well as for a range of case study analyses of wintertime orographic precipitation in other regions (for example Politovich and Bernstein (1995), Kusunoki et al. (2004)). The LWP observed in the two Brindabella case studies are generally comparable in both persistence and magnitude to those found by Kusunoki et al. (2004), but it is difficult to establish how representative such values actually are from case-study approaches.

The case study analysis presented here enriches the observations with comparisons to simulated values from the WRF model, as well as to satellite-derived values from the MODIS instrument. Although limited in number, the satellite-surface comparisons presented here suggest that MODIS gives a satisfactory picture of cloud integrated values. The persistence of these clouds observed by the radiometer adds support to the findings of Morrison et al. (2011) that supercooled cloud-tops are frequently observed along the Great Dividing Range. Diagnostics of water vapour path from the WRF model tend to follow the observed values quite closely, and statistically the LWP values are also quite good, suggesting that the model is simulating similar cloud "populations" overall.

The cross sections through the simulated cloud fields show that clouds simulated by the WRF model are qualitatively orographic in nature, contrasting with the nature of the Southern Ocean clouds over Tasmania (Morrison et al., 2010). Mapping of LWP amounts during the storms has not been presented as part of this analysis as direct comparison with the sporadic MODIS retrievals was not found to be informative; such an approach would be more valuable over seasonal time scales.

4.5.4 Back trajectories

It is interesting to note from these case studies that the passage of the surface front does not imply an instantaneous change in airmass history. In the July case, while the frontal passage is clear in the back trajectories, the air behind the front has spent the majority of the previous 72 hours in the lower atmosphere over the Murray-Darling Basin. It is not until around 03:00 UTC on 21 July, some 24 hours after the frontal passage occurred, that the trajectories resemble the typical south-westerly subsiding stream that is typically associated with post-frontal conditions. Precipitation at Mt Ginini has stopped by this time, probably as a result of the development of a rain shadow over the region, as the higher Victorian Alps and Snowy Mountains become upstream in the south-westerly flow.

The August case shows dynamical changes that are much less marked, with a slight change in wind direction seen in the trajectories associated with a weakly declining temperature. The trajectories do not form a coherent stream until about 12:00 UTC on 10 August, by which time precipitation had ended at Mt Ginini. The trajectories during this case spend most of their 72-hour history well below 500 m, with the exception of a handful that appear to circulate and descend with the passage of the low pressure system through the Bass Strait.

4.5.5 Summary and future work

The two case studies provide an in-depth picture of the nature of wintertime storms in the Brindabella Ranges, and it is likely that the insights gained from this work are applicable more broadly in the alpine regions of south-eastern Australia. The predominance of supercooled liquid phase clouds in winter as observed by the MODIS instrument is supported by both surface-based microwave radiometer observations and WRF model simulations. To establish the relationship between these cloud conditions and surface precipitation, additional work should be performed. Consideration of a large number of precipitation events over several winters would be necessary, and data from a more reliable precipitation gauge network is essential to making more general conclusions.

Chapter 5

Back trajectories during wintertime precipitation events

Meteorological trajectories represent the path of an infinitesimally small parcel of air by advection due to large scale winds, and are typically calculated by integration of wind fields from archived meteorological data. They are a useful representation of the airmass history at the point of termination and can be used to identify moisture sources during precipitation events, and are an attractive analytical tool because they are computationally inexpensive to produce and software to calculate them is readily available, and the inaccuracies associated with trajectories may be accounted for by the use of a statistical approach. Trajectory calculations for this analysis were performed using the Hybrid Single-Particle Lagrangian Integrated Trajectory (HYSPLIT) modelling system (Draxler and Hess, 1998a). The meteorological data used was the European Centre for Medium-Range Weather Forecasts (ECMWF) Interim Re-analysis (ERA-Interim) data (Simmonds et al., 2007), projected onto a 180 × 180 polar stereographic grid and processed into a format suitable for ingestion into HYSPLIT.

5.1 Calculation of meteorological trajectories

The path, or trajectory, of an infinitesimally small "parcel" of air through the atmosphere is calculated by the integration of the three dimensional wind from an initial position $\mathbf{X}(t)$. The parcel is assumed to travel at the same velocity as the background flow at all times, so the velocity $\dot{\mathbf{X}}(t)$ is generally obtained by interpolation of meteorological wind fields on a pre-defined grid. For all but the most simple of flows, this must be done by finite-differencing.

5.1.1 Trajectory equations

Evaluation of the Taylor series for $\mathbf{X}(t)$ about t_0 for $t_1 = t_0 + \Delta t$ gives:

$$\mathbf{X}(t_1) = \mathbf{X}(t_0) + \left.\frac{\mathrm{d}\mathbf{X}}{\mathrm{d}t}\right|_{t_0} \Delta t + \frac{1}{2}\left.\frac{\mathrm{d}^2\mathbf{X}}{\mathrm{d}t^2}\right|_{t_0} \Delta t^2 + ... \tag{5.1}$$

To first order, this may be expressed as:

$$\mathbf{X}(t_1) \approx \mathbf{X}(t_0) + \dot{\mathbf{X}}(t_0)\Delta t. \tag{5.2}$$

This is an explicit Eulerian (first order) integration, and is exact only for *zero acceleration* conditions (Stohl, 1998), but accuracy is lost as the integration time step is increased. Additional accuracy may be gained by expanding $\mathbf{X}(t)$ about t_1 and evaluating at $t = t_0$, i.e.:

$$\mathbf{X}(t_0) = \mathbf{X}(t_1) - \left.\frac{\mathrm{d}\mathbf{X}}{\mathrm{d}t}\right|_{t_1} \Delta t + \frac{1}{2}\left.\frac{\mathrm{d}^2\mathbf{X}}{\mathrm{d}t^2}\right|_{t_1} \Delta t^2 - ... \tag{5.3}$$

Combining equations 5.1 and 5.3 and solving for $\mathbf{X}(t_1)$ gives:

$$\mathbf{X}(t_1) = \mathbf{X}(t_0) + \frac{1}{2}\left[\left.\frac{\mathrm{d}\mathbf{X}}{\mathrm{d}t}\right|_{t_1} + \left.\frac{\mathrm{d}\mathbf{X}}{\mathrm{d}t}\right|_{t_0}\right]\Delta t + \frac{1}{4}\left[\left.\frac{\mathrm{d}^2\mathbf{X}}{\mathrm{d}t^2}\right|_{t_1} - \left.\frac{\mathrm{d}^2\mathbf{X}}{\mathrm{d}t^2}\right|_{t_0}\right]\Delta t + ... \tag{5.4}$$

Again using only first order terms, the above equation reduces to

$$\mathbf{X}^n(t_1) \approx \mathbf{X}(t_0) + \frac{1}{2}\Big[\dot{\mathbf{X}}(t_0) + \dot{\mathbf{X}}^{n-1}(t_1)\Big]\Delta t, \tag{5.5}$$

the *constant acceleration* equation (Stohl, 1998), which is an implicit scheme which must be solved iteratively, as $\dot{\mathbf{X}}(t_1)$ is not known beforehand. Successively solving equation 5.5 with sufficiently small time steps and low rates of change in acceleration will lead to convergence in $\mathbf{X}(t_1)$. Equation 5.5 is accurate to second order in Δt. It has been used for many years in trajectory calculations and is attributed to Petterssen (1940).

"Back trajectories", the path of a parcel of air to a point of interest, are calculated in exactly the same way by using a negative value of Δt. These are a useful tool in air quality studies, for example, to explain variations in concentrations of various tracers over time at a fixed monitoring site.

5.1.2 Accuracy of trajectories

There are a number of factors which impact the accuracy of trajectory calculations. This section provides a discussion of the literature regarding the accuracy of meteorological trajectories.

Limitations of the numerical scheme

The discarding of the higher order terms in equation 5.1 result in inaccuracies termed *truncation errors.* As expected, the integration error that arises from the finite difference schemes is related to the time step Δt. Walmsley and Mailhot (1983) showed that the first order scheme in equation 5.2 deviates in direct proportion to Δt, whereas the iterative scheme (equation 5.5) diverges with Δt^2 by comparing these schemes to trajectories calculated using high order numerics with very short time steps. It is possible to retain higher-order terms in equation 5.4, but the gains in accuracy are offset by the need to calculate accelerations by taking derivatives of the (usually rather coarse) gridded wind fields.

Impact of meteorological data resolution

Due to the limited availability of computational resources and data storage facilities, earlier research using meteorological trajectories was more adversely impacted by the low resolution of meteorological archives. The earlier trajectory calculations were performed based on horizontal winds derived from radiosonde networks, but these measurements were of limited resolution both temporally (typically 12 hours between soundings) and spatially. Objective analysis techniques provided a means to both minimise the errors of measurement and represent smaller scale features of the wind fields.

Data resolution		Travel time		
Spatial	Temporal	24 h	48 h	72 h
Coarse	12 h	210	285	350
Coarse	6 h	185	280	335
Fine	12 h	180	245	300
Fine	6 h	150	230	275

Table 5.1: Horizontal transport errors (km) at 24, 48 and 72 hours with a 50% chance of exceedance. From Kahl and Samson (1986, table 2).

Radiosonde releases additional to the regular US National Weather Service (NWS) soundings during the Cross Appalachian Tracer Experiment (CAPTEX) provided a means to analyse the impact of interpolating low resolution wind fields on trajectory accuracy. Kahl and Samson (1986) showed that the mean *absolute* errors in the horizontal winds introduced by the interpolation techniques were on the order of 2-4 ms^{-1}. Artificially applying normally distributed errors based on this result to the pre-calculated position along a trajectory, a Monte Carlo experiment was performed to evaluate the propagation of error throughout the trajectory calculation.

Table 5.1 shows the horizontal error values for which there was a 50% chance of exceedance for the experiment outlined by Kahl and Samson (1986). Here “Coarse” and “Fine” denote the use of the NWS and CAPEX radiosonde networks respectively, and note that the regular sounding frequency for the NWS upper air locations is 12 hours. The results indicated that the greatest gains in trajectory accuracy were to be made by increasing the spatial resolution of the radiosonde network, but the gains made by increasing the frequency of soundings was likely to be more cost effective.

The results of Kahl and Samson (1986) were most likely an underestimate of the propagation of error (Stohl, 1998), as they did not account for the growth of error due to the difference in the wind fields at the perturbed trajectory locations (most likely due to computational constraints). The limited period of analysis used in this study meant that the trajectories used were of a single synoptic type, to the representativeness of these results to general climatologies of trajectories has also been questioned.

Rolph and Draxler (1990) artificially degraded the spatial and temporal resolution of especially prepared NWS model data to test the sensitivity of three dimensional trajectories (i.e.

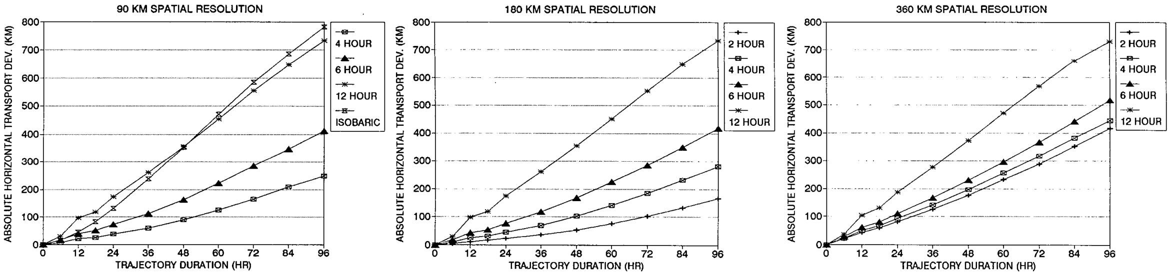

Figure 5.1: Absolute horizontal transport deviation for three different data resolutions. From Rolph and Draxler (1990, figures 2-4).

those where vertical winds are explicitly used) on wind field resolution. Trajectories were calculated on a grid over the USA using the NWS data on a 90 km grid, output every two hours. A total of 63 starting locations were used, and trajectories were calculated twice daily over a period of 74 days, resulting in a collection of 9324 "truth" trajectories. Twelve sets of "experimental" trajectories were calculated with the same meteorological data sampled at 90, 180 and 360 km every two, four, six and 12 hours, and a thirteenth set was calculated from the control conditions, but with vertical winds not modelled (isobaric transport assumed).

The difference between N pairs of "truth" and "experimental" trajectories was expressed as the mean absolute horizontal transport deviation (AHTD):

$$\mathrm{AHTD}(t) = \frac{1}{N}\sqrt{\sum_{n=1}^{N} \left|\mathbf{X}_a^n - \mathbf{X}_b^n\right|^2}, \tag{5.6}$$

where $\mathbf{X}_a$ and $\mathbf{X}_b$ are the horizontal coordinates of the point along the "truth" and "experimental" trajectories at time t respectively. Absolute vertical transport deviation (AVTD) was expressed similarly, except using pressure coordinates. The results for horizontal deviation from Rolph and Draxler (1990) for the entire collection of trajectories are shown in figure 5.1.

Horizontal deviations of less than 200 km were found for all configurations at 24 hours of travel time, whereas deviations of greater than 700 km were found by 96 hours. The deviations increased linearly with time after about 24 hours of travel for all experiments. If expressed in terms of *relative* deviations (the deviation divided by the distance from the source), it was found that deviation did not grow strongly with time, suggesting that travel distance is an important factor.

Decreasing the spatial density of the meteorological fields from 90 to 180 km had a negligible impact on the trajectories, indicating that the temporal density of the meteorological fields used was the most important factor at these spatial resolutions. Further decreasing the spatial density to a resolution of 360 km was found to degrade all trajectories except those calculated from the 12-hour fields. At this resolution, the similarity in the deviation for the 2-, 4- and 6-hour trajectories suggests that the temporal resolution is less important.

Vertical motion

One of the major difficulties in the calculation of meteorological trajectories is the representation of vertical motion. A number of factors influence the vertical motion of the atmosphere, including topography, synoptic forcing and moist convection. Routine observations of atmospheric vertical motion are not made, leaving two choices for representing the vertical motion in trajectory calculations; the assumption of “two-dimensional” motion, such that some height coordinate is conserved, or the use of simulated or analysed vertical winds to calculate a “three-dimensional” trajectory.

Isobaric trajectories remain on surfaces of constant pressure and are among the most straightforward to calculate, reducing the need for interpolation as wind fields are often provided on pressure levels. However, they are unrealistic as they do not account for vertical motions due to synoptic forcing and may intersect the terrain. Isosigma trajectories (which follow the terrain more closely near the surface) are a preferable choice.

Isentropic trajectories lie on surfaces of constant potential temperature and more accurately reflect the motion of air in adiabatic conditions. These conditions hold for dry air in the free troposphere, but problems are encountered in the boundary layer or in regions of saturation (Stohl and Seibert, 1998), where direct and latent heat fluxes are more important.

The vertical winds are generally analysis products deduced from the divergence of two dimensional wind fields, or explicitly predicted outputs from NWP models. Both of these sources have their drawbacks; in particular the noise level in the horizontal divergence fields is typically on the same order as the signal (Sardeshmukh and Liebmann, 1993), and the use of convective parametrisations causes difficulties in the explicit prediction of w. Nevertheless, if accurate three dimensional wind fields are available, these provide the highest degree of accuracy for trajectory calculations (Stohl and Seibert, 1998).

Wind field analysis errors

One of the major sources of error for trajectories, over and above the effects of interpolation and representation of vertical motion, are errors in the wind fields themselves. Especially in the vicinity of strongly dynamic systems, where large changes in the wind fields may be experienced over relatively short distances, small analysis errors in the placement of the feature can lead to amplification of errors in the trajectory position. Stunder (1996) found that trajectories were most accurately represented in conditions of strong steady flow, such as those that occur behind a cold front.

Sub-grid scale processes

There are a number of processes that are not represented by wind field data that can nonetheless have substantial bearing on the accuracy of trajectories. Turbulence in the boundary layer is one such example; when vertical motions vary on a scale much smaller than represented by the wind fields, what is the appropriate vertical velocity to use? The answer depends on the application; for transport of moisture in the boundary layer, the small scale motions are not of much concern, as the concentrations vary slowly in a spatial sense. On the other hand, the stability of the boundary layer can have a profound effect on the transport of a pollutant from a localised source.

5.1.3 Employment of the HYSPLIT model

Model overview

The Air Resources Laboratory (ARL) Hybrid Single Particle Lagrangian Integrated Trajectory (HYSPLIT) model (Draxler and Hess, 1998a) is a system for predicting atmospheric transport and dispersion in a wide range of applications, from calculating trajectories to simulating plume dispersion and deposition. The modelling system was initially developed in

1982 (Draxler and Taylor, 1982) and since then has undergone a series of updates to incorporate a variety of features, most notably the inclusion of semi-Lagrangian dispersion and a series of improvements to the vertical mixing schemes.

A full description of the HYSPLIT model features is given by Draxler and Hess (1998b) which is available on the Air Resources Laboratory website.

Numerical scheme

A discussion of the numerical schemes used to integrate the position of an air parcel was given in section 5.1.1. HYSPLIT uses equation 5.5 with a single iteration (that is, not requiring convergence with successive iterations), referring to the result of equation 5.2 as a "first guess" location. The use of linear interpolation to evaluate the wind fields at $\mathbf{X}(t)$ means that further iteration or higher order schemes are redundant (Draxler and Hess, 1998b).

Meteorological data

In general, meteorological fields can not be used directly by the HYSPLIT model. The standard format for the meteorological data is the *ARL packed binary file*, which contains a time series of fixed length records, including upper air and surface variables. The ARL data is recorded on terrain-following (σ) coordinates, with model levels generally spaced quadratically from the surface upwards. The ARL provides a suite of utilities packaged with the HYSPLIT model to facilitate the conversion of a range of standard meteorological products into the required format.

A number of meteorological data archives are maintained on the ARL website[1], but these have a primary focus on the North American region. The global products are either of very coarse resolution (e.g. the NCEP reanalysis, which is available on a 2.5° × 2.5° grid), or do not have sufficient historical data for the requirements of this project. Two alternative data sets were used:

1. ECMWF Interim Reanalysis (ERA-Interim): This reanalysis product, which is archived locally, provides six-hourly meteorological fields on a 1.5° latitude-longitude grid from

---

[1] ARL website, viewed May 9, 2011: http://ready.arl.noaa.gov/archives.php

1989–present. The required fields were extracted using the Climate Prediction Center `wgrib` program and converted into ARL compatible format using the utility programs provided with HYSPLIT (see appendix A.3 for detailed instructions and python source code). The archive developed to support the current research is most suitable for the investigation of flow patters associated with synoptic scale features.

2. Australian Mesoscale Limited Area Prediction System (MLAPS): The Australian Bureau of Meteorology routinely converted three-hourly MLAPS (Puri et al., 1998) output into ARL compatible format for use in air-quality monitoring. The MLAPS output is provided on a 0.125° degree grid and was archived locally for dust transport research. This archive is better suited to source-receptor type studies due to the higher resolution of the wind fields.

The main content of this chapter discusses trajectories calculated with the ERA-Interim data to investigate synoptic flow from the perspective of the Snowy Mountains region, while the MLAPS data was used to calculate trajectories to investigate the impact of pollution on precipitation in chapter 6.

Running HYSPLIT in batch mode

Python scripts were written to automate and monitor the calculation of trajectories. To calculate a climatology of trajectories for a given location, a temporary configuration file was written for each start time (for example, each hour between two dates). This was fed to the HYSPLIT executable from within Python, and the trajectory calculation output was monitored automatically. The output file is named according to the start time and archived, and all temporary files are removed. The Python source code is included as a supplement to this thesis in appendix A.3.

5.2 Airmass history during wintertime in the Snowy Mountains

There are several motivations for performing an airmass climatology of the Snowy Mountains. The airmass origin provides insight to the dynamic processes behind the observed meteorology at a location of interest. Trajectories can provide a physical link between hypothesised remote moisture sources and precipitation in the mountains. In light of the discussion of wintertime precipitation declines in chapter 2, the identification and interpretation of changes in the airmass history is of considerable interest.

5.2.1 Trajectory database

Moisture is transported by advection in all levels of the troposphere, but water vapour mixing ratios are highest near the surface, implying that the bulk of moisture is transported in the lower levels. Trajectories arriving at a set of levels below 5000 m AGL (above ground level) above Mt Blue Calf (148.39° E, 36.39° S; a central mountaintop location) were calculated on three-hourly intervals for the months of May–September in the period 1990–2009. The wind fields used to perform the calculations were derived from the ECMWF ERA-Interim Reanalysis as described in section 5.1.3.

Trajectories arriving at two primary levels are presented for comparison in this section. Trajectories arriving at 500 m AGL are typically within the planetary boundary layer, particularly for the windy conditions that accompany wintertime storms in mountainous terrain. These lower-level trajectories are of interest because they are of particular importance for orographic clouds. To represent the airmass above the boundary layer, trajectories arriving at 3000 m AGL are discussed. Figure 5.2 shows moisture fluxes derived from the daily Wagga Wagga soundings (the nearest regular sounding, some 150 km to the north-west) at the pressure levels corresponding to these arrival heights in the Snowy Mountains.

For each of these levels, a database of 24 480 trajectories was calculated using HYSPLIT with ERA-Interim data in batch mode on a Linux PC.

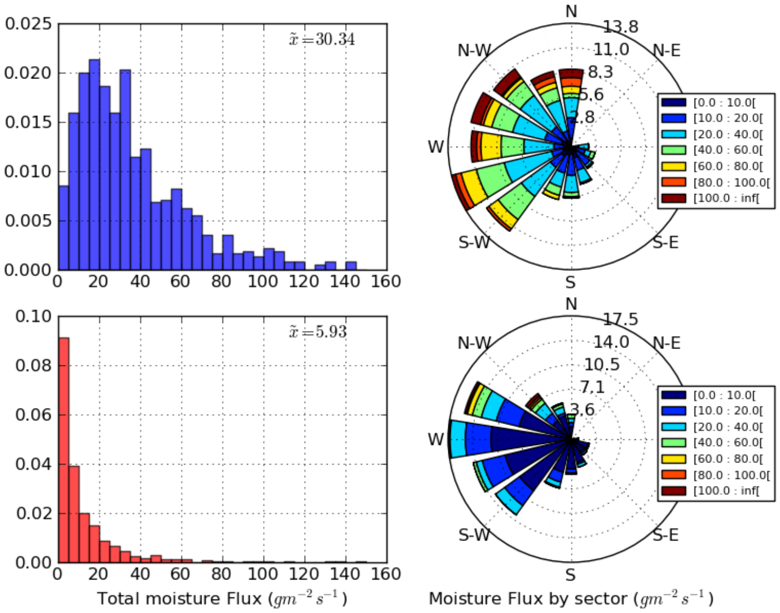

Figure 5.2: Moisture fluxes calculated from the Wagga Wagga sounding for May–September in 2005–2009. Fluxes were calculated at the 900 hPa (above) and 650 hPa (below) pressure levels, which are the approximate levels for the 500 and 3000 m AGL trajectories respectively. Note the different scales on the histograms, and the median moisture flux amount indicated in the upper right.

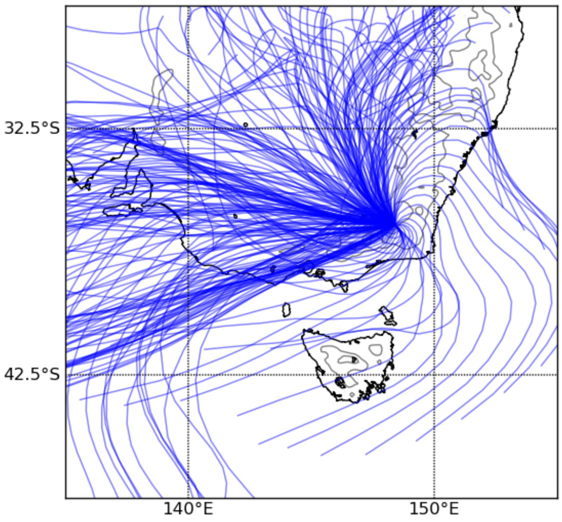

Figure 5.3: One month (July 2010) of three hourly trajectories arriving at 500 m AGL in the Snowy Mountains.

5.2.2 Climatological representation of trajectories

Individual trajectories may be presented graphically by mapping hourly positions or heights. This is a useful representation for limited-duration examples or case-study approaches, but to represent a climatology this becomes cumbersome. Figure 5.3 shows one month's worth of trajectories arriving in the Snowy Mountains. While some important features may be identified from this figure, for example the westerly and south-westerly streams and the northerly component, objective comparisons with other trajectory subsets is difficult with this type of representation.

Instead, the hourly position (ϕ_k, λ_k) of each trajectory (where k is in hours before the "end time") was binned on a $20° \times 20°$ latitude-longitude grid at 0.5° resolution over the domain shown in figure 5.3. The grid was binary in the sense that multiple counts in one bin were not represented, and trajectories that left the domain were truncated from the hour of departure. This was performed for each of the N trajectories in a given collection to form a binary array Δ. If the meridional and zonal bin edges of the grid are denoted by the sets $\{\Phi\}$ and $\{\Lambda\}$ respectively, while i and j represent the grid indices in the corresponding sense ($0 \leq i, j \leq 39$ for this configuration), the elements Δ^n_{ij} of this matrix are expressed as follows:

$$\Delta^n_{ij} = \begin{cases} 1, & \text{if } \Phi_i \leq \phi^n_k < \Phi_{i+1} \text{ and } \Lambda_j \leq \lambda^n_k < \Lambda_{j+1} \\ 0, & \text{otherwise} \end{cases} \tag{5.7}$$

The index k does not appear on the left of equation 5.7, reflecting that information about the time before arrival is lost in this representation. The superscript n relates to the arrival time of each trajectory represented by the three dimensional array. In practice, Δ is constructed by iterating over n and k to identify which ordered pairs (i, j) to "set" in the matrix.

The position probability distribution $\mathcal{P}$ of air parcels arriving at a given site is estimated by summation and subsequent normalisation over these binary arrays:

$$\mathcal{P}(\phi, \lambda) \simeq \frac{\sum_n \Delta^n}{\sum_{n,i,j} \Delta^n_{ij}} \tag{5.8}$$

Figure 5.4 shows the PPD for all trajectories arriving at 500 and 3000 m in the winter months during the 20-year analysis period. At the lower levels, the shape of the distribution is axially

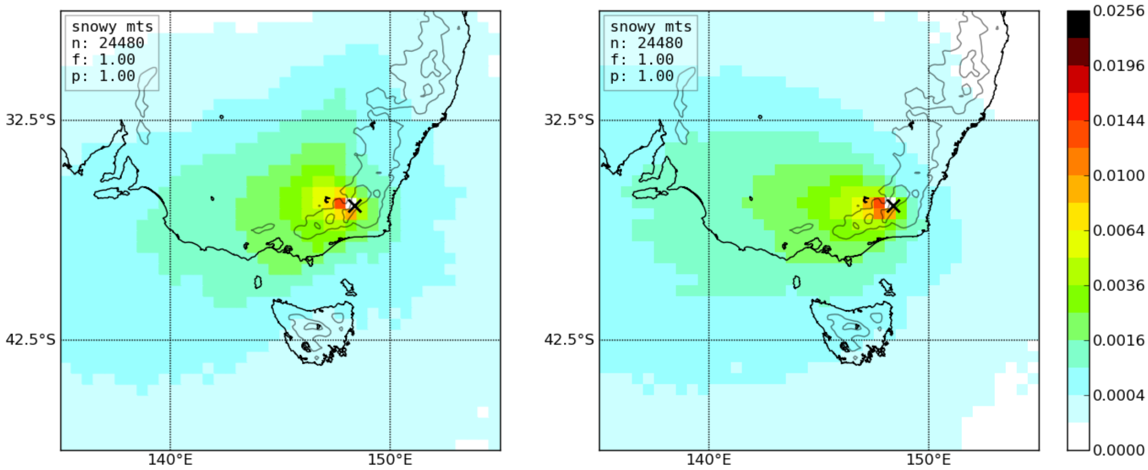

Figure 5.4: Position probability distribution for all trajectories arriving at 500 m (left) and 3000 m (right) in the Snowy Mountains between 1990 and 2009 in the months May–September. The annotations in the box are n, the number of trajectories represented, f, the proportion of all "wet" trajectories (see text), and p, the proportion of precipitation accounted for by these trajectories (unity in this figure because all trajectories are represented). Note the quadratically spaced colour map.

non-symmetric, with the majority of trajectories arriving from the south-west. A secondary path for trajectories from the north appears to be evident over central New South Wales, roughly following the contours of the Great Dividing Range. For the upper level, the picture is slightly different. A clockwise rotation of the principal direction of approach relative to the 500 m is evident, consistent with the westerly winds which dominate flow at this latitude, especially during winter.

Trajectories associated with precipitation

In order to identify moisture corridors and sources, trajectories arriving at 500 m were selected if precipitation recorded by the SHL gauges during the three hours prior to arrival was more than a threshold amount T. These trajectories form a PPD that is interpreted as a function of position, and is constructed exactly as above, but with an additional Dirac delta function δ_r:

$$\delta_r(p^n) = \begin{cases} 0, & p^n < T \\ 1, & p^n \geq T \end{cases} \tag{5.9}$$

Where p^n is the amount of precipitation recorded in the three hour interval associated with the n-th trajectory. This term is included in the binary array representation of the trajectory, such that:

$$\Delta^n_{r_{ij}} = \delta_r(p^n)\Delta^n_{ij} \tag{5.10}$$

PPDs are constructed in the same manner as described above for these trajectories and shown in figure 5.5. The threshold used in this figure was 1.0 mm, which accounts for 91% of the recorded precipitation (i.e. 9% of precipitation was at rates lower than this). About 17% of all trajectories are represented in these figures. Compared with the probability distribution shown in figure 5.4, the lower level trajectories show a contrasting pattern. Trajectories associated with at least 1.0 mm of precipitation are most likely to come from due west, but the northern route is also of relative importance. There is a gradient in the value of $\mathcal{P}$ that is roughly coincident with the location of the Great Dividing Range; values of $\mathcal{P} > 0.0016$ (green shade) occur exclusively inland of the watershed, implying a controlling influence of topography on Snowy Mountains precipitation amounts, not simply locally but on a large scale.

The pattern for the 3000 m trajectories, on the other hand, is broadly similar to that shown in figure 5.4, implying that the origin of air arriving at this level does not have as strong an impact on precipitation.

Difference probability distributions

The distributions shown in figures 5.4 and 5.5 can be directly compared. Subtraction of the matrix representation of $\mathcal{P}$ for all trajectories (figure 5.4) from that for the "wet" trajectories (figure 5.5) yields a distribution which represents a suppression/enhancement pattern. Figure 5.6 shows this pattern for trajectories arriving at 500 and 3000 m, using a precipitation threshold amount of $T = 1.0$ mm.

Precipitation is more frequently associated with trajectories that pass through the blue shaded regions. For both the lower and upper level trajectories, the west-north-west sector is found to be associated more frequently with three-hour precipitation amounts greater than 1.0 mm.

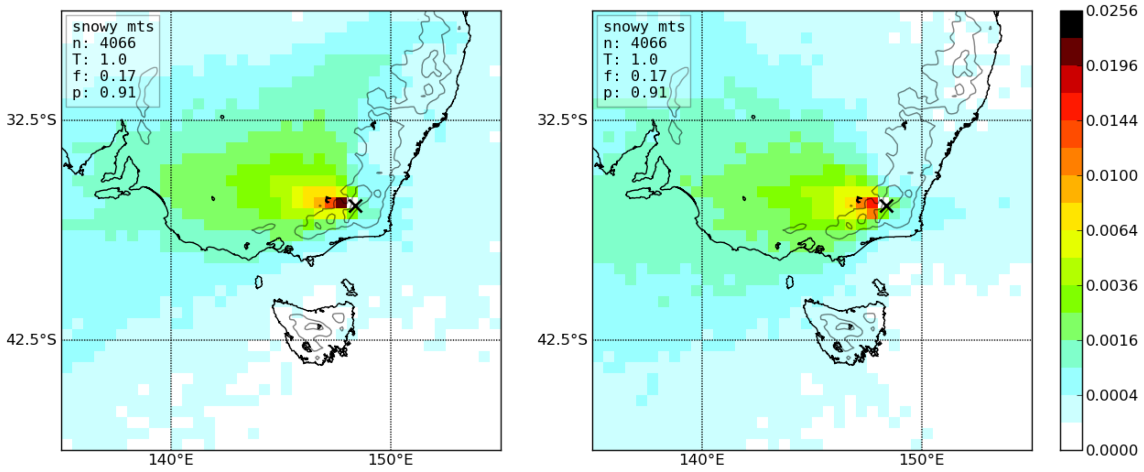

Figure 5.5: As for figure 5.4, but only using trajectories associated with a three-hour precipitation accumulation of at least $T = 1.0$ mm.

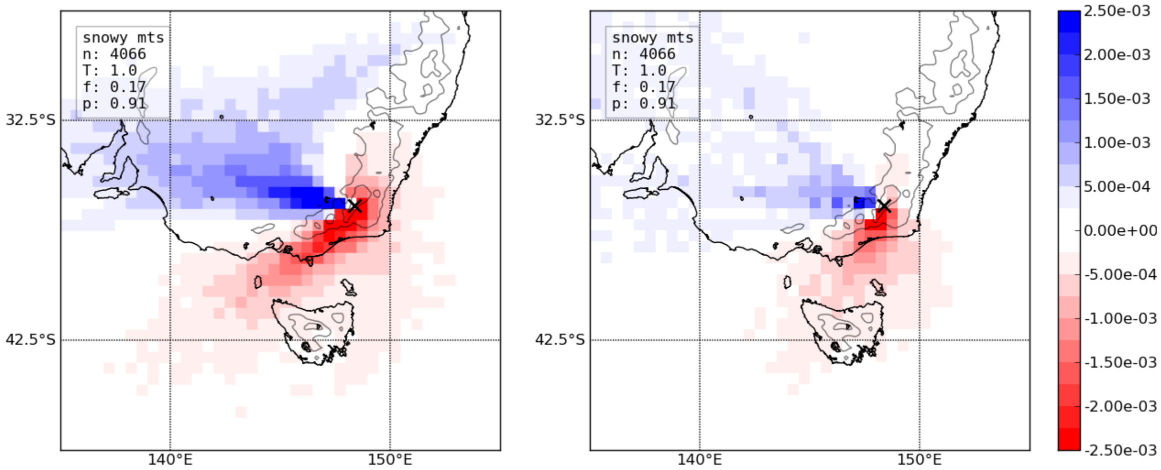

Figure 5.6: Difference between position probability distribution for all trajectories (from figure 5.4), and those associated with a three-hour precipitation accumulation of at least $T = 1.0$ mm (from figure 5.5).

The effect is more pronounced and coherent for the lower level trajectories. A secondary "corridor" is evident in the lower trajectories to the north, which runs along the western slopes of the great dividing range, but this feature is absent from the upper trajectories.

Trajectories passing through the region shaded red to the south and south-west of the Snowy Mountains are less likely to be associated with precipitation amounts above the threshold. This means that either the synoptic systems responsible for bringing precipitation do not result in trajectories from the south-west, or there is some mechanism suppressing precipitation in this region. Figure 5.6 shows that the suppressed region is to the far side of the Victorian Alps, which are apparently casting a rain shadow over the Snowy Mountains during south-westerly conditions. Indeed, a similar pattern is observed when the same analysis is performed for a number of high-elevation AWS sites along the north-western slopes of the Great Dividing Range, between Mt Ginini to the north and Mt Buller in the southern Victorian Alps. When performed for the Mt Baw-Baw AWS (to the south of the divide), the PPD shows a complementary pattern of suppression from the north-west and enhancement from the south-east. This indicates that either different phases of storms or different synoptic systems altogether are responsible for precipitation in alpine regions with a southern aspect. The effect is again less pronounced for the upper level trajectories.

In relative terms, the impact is measured by comparing the magnitudes of the difference PPD to the "wet" PPD at locations of interest. For example, trajectories passing through tiles in the Port Pirie region near Adelaide are about 30% more likely than average to be associated with at least 1.0 mm of precipitation in the Snowy Mountains, while those passing through Gippsland are about 90% less likely to be associated with this precipitation amount.

Analysis of uncertainties

As discussed in section 5.1.2, substantial position uncertainties for the trajectory calculations are introduced by errors in the analysed wind fields and interpolation of coarse meteorological data. According to the results of Rolph and Draxler (1990), the temporal and spatial resolution of the ERA-Interim reanalysis data would lead to an expected uncertainty (horizontal transport deviation) of some 150 km at 48 hours of trajectory duration. For the figures shown in this section, this uncertainty is equivalent to about three grid tiles. In assessing the results presented in this chapter, the question of whether this uncertainty has a substantial impact on the conclusions drawn must be addressed.

To do this formally, a Monte-Carlo experiment could be performed, where hourly position on a trajectory is perturbed by a random error $e(t)$ before the construction of the matrix representation of the individual trajectories (equation 5.8), and continuing to construct the PPDs as previously.

In practice, this type of analysis was not considered necessary, as the magnitude of the expected error is not of concern on the scale of the synoptic scale features that are discussed in this chapter. Random errors on the scale of three grid tiles in figure 5.6 may serve to blur the boundaries of the features noted, but in general there are sufficiently large numbers of trajectories included in these analyses to ensure that the features are of significance. Instead, the same analyses have been performed with alternative meteorological datasets. The features were initially identified using the operational NCEP Global Data Assimilation System (GDAS) output, which is archived in packed binary format on the ARL website. At a spatial resolution of $1^\circ \times 1^\circ$ this data is of higher resolution than the ERA-Interim Reanalysis, but only available from 2005. The hemispheric $2^\circ \times 2^\circ$ NCEP Reanalysis data was also used for the period 2005–2009 and the trajectory analyses display similar features, but the ERA Interim data was used in preference because of its in-house availability and superior resolution.

5.2.3 Intensity of precipitation

The patterns seen in figure 5.6 change for different precipitation intensity thresholds. Figure 5.7 shows the difference PPD for threshold values between 0.2 and 12 mm.

Increasing the precipitation threshold has a different effect on the trajectory patterns at the two levels. The 500 m trajectories show a shift from predominantly westerly trajectories at the trace (0.2 mm) threshold to being completely dominated by trajectories arriving from the north at the higher thresholds. Heavy precipitation accounts for about 15% or all recorded precipitation but is associated with only about 1% of trajectories. It is most likely to be associated with this northern corridor, at least for the low level trajectories. For a threshold of 3.0 mm, which accounts for 68% of all precipitation, the contribution is roughly equal.

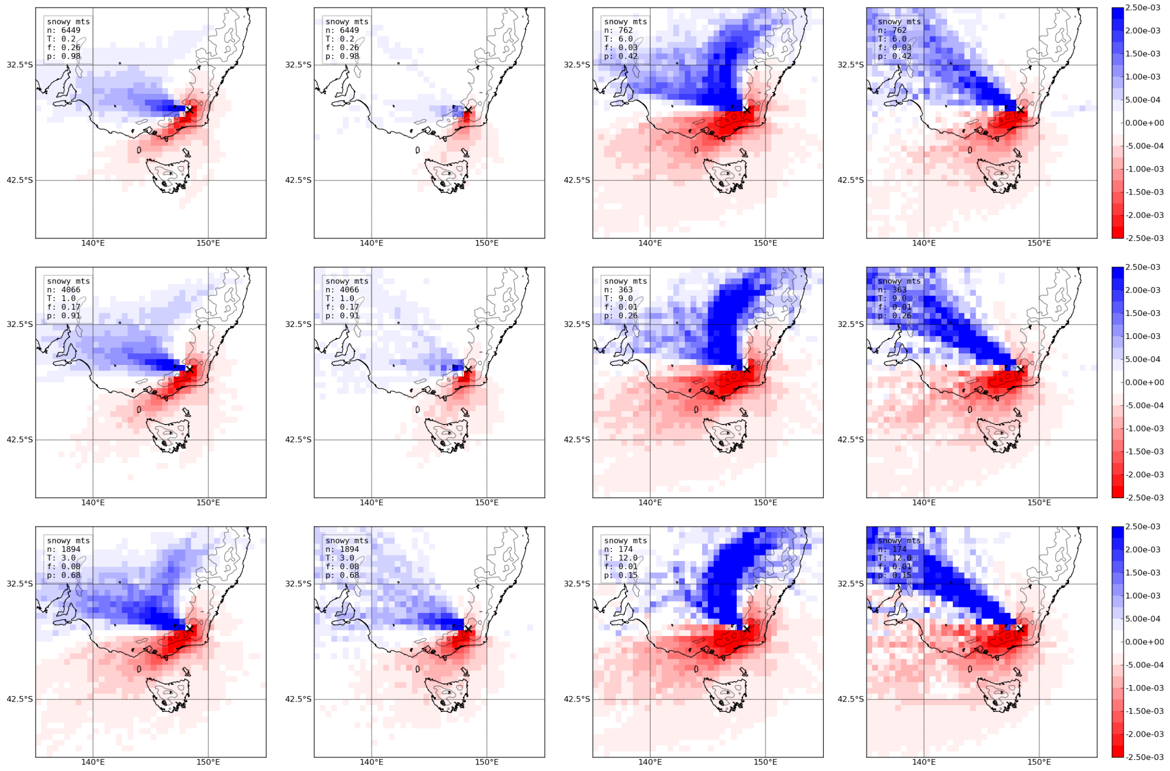

Figure 5.7: Difference between position probability distribution for all trajectories, and trajectories associated with a range of precipitation thresholds, at 500 m (first and third columns) and 3000 m (second and last columns). Three-hour precipitation thresholds used were 0.2, 1.0, 3.0, 6.0, 9.0 and 12.0 mm.

The upper level trajectories tell quite a different story. For trace precipitation amounts, there is virtually no signal in the trajectory patterns at 3000 m. The octant centred on west-north-west becomes evident at T = 1.0 mm, but for higher precipitation rates, the primary moisture corridor tightens to a narrow sector centred to the north-west. However, as it has been shown that the median moisture flux at this level is six times less than at the lower levels, the trajectories probably do not represent a moisture path, but rather a dynamic feature of upper level flow during more intense precipitation. These trajectories are most likely the result of the poleward flow along the east of a propagating trough. These conditions are associated with upper level divergence and would be conducive to convection.

The 500 m trajectory patterns capture something of the dynamics of frontal passages. The higher precipitation rates are most likely associated with the "warm conveyor" mechanism (Browning, 1986), otherwise termed atmospheric river (Zhu and Newell, 1994) ahead of a cold front. This lifting mechanism, combined with the forced uplift over the GDR, is responsible for the heavy precipitation rates observed. It is remarkable, however, that the moisture corridor is so coherent. The pattern observed suggests low-level moisture transport from the Coral Sea to the east of southern Queensland in the day or so before the frontal passage. The GDR in New South Wales appears to provide an eastern boundary to the corridor, and moisture is advected inland at around 30° S.

Following the passage of a strong front, the airmass typically changes from being subtropical in nature to mid-latitudinal. The westerly conditions continue force colder, drier air over the mountainous barrier, resulting in sustained precipitation but at a lower rate. This post-frontal scenario is most likely to be responsible for the trajectory patterns seen when the three-hour precipitation rate is less than about 3.0 mm, as the west-north-west corridor is aligned with the approximate gradient of the GDR in the Snowy Mountains region.

5.2.4 Atmospheric circulation, trajectories and precipitation

Meteorological trajectories naturally reflect changes in regional circulation. For the southern Australian region, the Southern Annular Mode is of particular importance and has been shown to be associated with cool season precipitation (Nicholls, 2010). In figure 5.8, trajectory composites have been formed by selection of trajectories based on the sign of the monthly

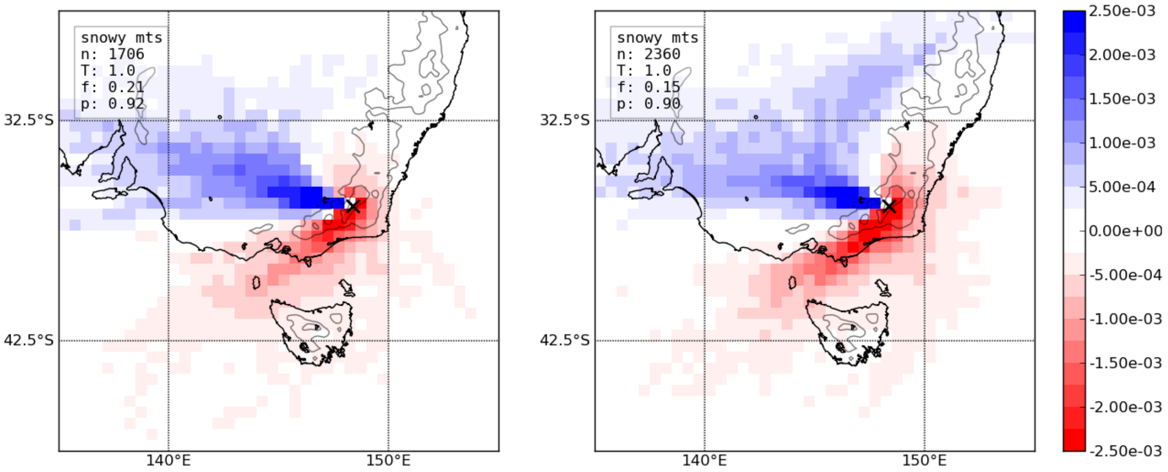

Figure 5.8: As for figure 5.4, except for trajectories arriving in months with negative (left) and positive (right) SAM index.

SAM index. For the negative phase, which describes an equatorward shift of the westerly belt, precipitation is shown to be more regularly associated with trajectories which have come from the west, with no remarkable contribution from the northern corridor. For the positive phase, the northern corridor is relatively much more important. Precipitation amounts above 1.0 mm are more frequent in the negative phase of the SAM, with 21% of all trajectories bringing at least this amount, compared to 15% for the positive phase. Incidentally, precipitation amounts for the high elevation gauges in the months with a negative SAM index were found to be about 30% higher than for months with a positive value.

A conceptual interpretation of these different patterns is that for negative values of the SAM index, there is a stronger influence of post-frontal flow over the topographic barrier. For positive values, the westerly stream brings less frequent precipitation, and the conveyor mechanism (frontal precipitation) plays a more dominant role.

This result gives insight into the exacerbated decline in precipitation amounts on the western slopes and at high elevation in the Snowy Mountains region. Trends in the wintertime SAM index during the analysis period have been strong, with about 1.5 more positive *monthly* values per year recorded at the end of the analysis period compared to the start. This represents a change in global circulation corresponding to a poleward shift in the average position of the westerly belt. Decreased westerlies over the Snowy Mountains region would result in a decrease in the orographic enhancement of precipitation, which is most important for the exposed slopes and high elevation regions. This is wholly consistent with Budin (1985), who found that years with stronger low-level westerlies are significantly related to winter snowpack depth.

Trajectories were also sorted on a range of different bases for investigation, but none were found to differentiate the patterns as substantially as the SAM index. The same analyses as shown in figure 5.8 are presented in appendix A.5 for the following selection criteria. Selection based on sign of the Southern Oscillation Index resulted in no substantial differences from the composites in figure 5.6, suggesting that this index does not impact trajectories associated with precipitation in the Snowy Mountains. When selected on the basis of synoptic type, the differences were quite subtle, the main feature being the increased relative importance of the westerly corridor for embedded lows. Selection of trajectories based on whether they came from one of the five wettest or driest years resulted in composites that were very similar to those in figure 5.8, as would be expected if the phase of the SAM index plays a role in the seasonal precipitation amount.

Chapter 6

Identification of precipitation suppression using back trajectory methods

The potential effects of air pollution in the alpine regions have received some attention from the scientific community in recent years. Recent satellite-based Advanced Very High Resolution Radiometer (AVHRR) observations depicting the effect of “pollution plumes” on cloud droplet effective radius in south-eastern Australia have raised concerns about suppression of precipitation in the Snowy Mountains region (Rosenfeld, 2000 and Rosenfeld et al., 2006, 2009). The aerosol pollution from industrial sources such as the Port Pirie lead smelter and the Port Augusta power plant was shown to reduce the cloud droplet effective radius from over 25 μm to under 14 μm, a threshold value for efficient droplet coalescence processes. This research has been controversial, with Ayers (2005, 2009) showing that the weather systems originally explored by Rosenfeld were not typical of precipitating systems affecting south-eastern Australia, so any effect on such clouds would be negligible in terms of seasonal precipitation. Levin and Cotton (2009) reviewed the status of research into the impact of pollution on clouds and precipitation, finding that while in-situ observations of clouds indeed verify the link between atmospheric aerosol loading and cloud droplet number concentration, the effect of pollution on surface precipitation observations has not been established. A lack of observational studies linking aerosol pollution to changes in precipitation, and the failure

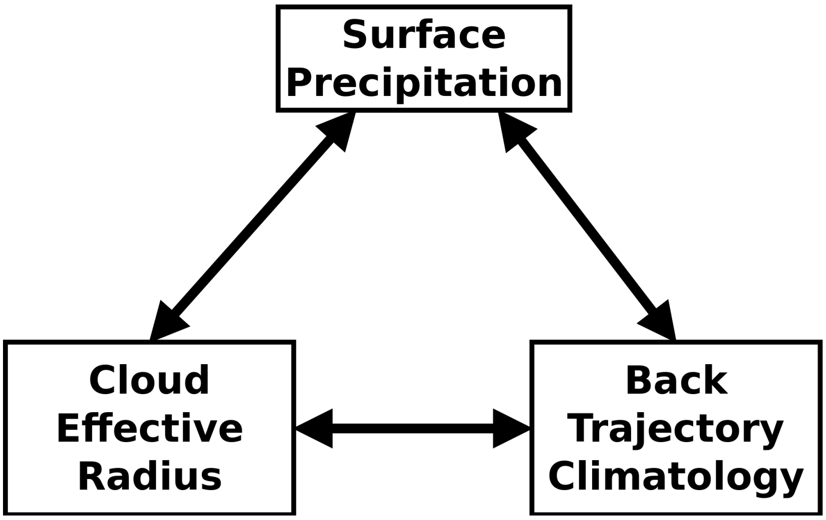

Figure 6.1: Precipitation, cloud effective radius and trajectory climatology

of these studies to rule out meteorological factors were identified as obstacles to ascertaining this effect. It was noted that "orographic clouds are the most susceptible to modification in precipitation by pollution owing to the modest liquid water contents in them, the relatively short time the drops and ice crystals spend in the clouds and the large areal coverage", which has some resonance with the hypothesis of Rosenfeld (2000).

This chapter outlines an analysis performed to address some of the concerns of both sides of this argument by investigating the links between cloud effective radius, surface precipitation and back trajectories (figure 6.1). Moderate Resolution Imaging Spectro-radiometer (MODIS) observations of cloud droplet effective radius are described in depth in the following sections. High quality surface precipitation measurements from the Snowy Mountains recorded between 2005 and 2010 were used to evaluate precipitation rates for the times at which the MODIS observations were made, and back trajectories generated using high resolution meteorological data were used to relate the airmass history to a selection of potential pollution sources, including those identified by Rosenfeld (2000).

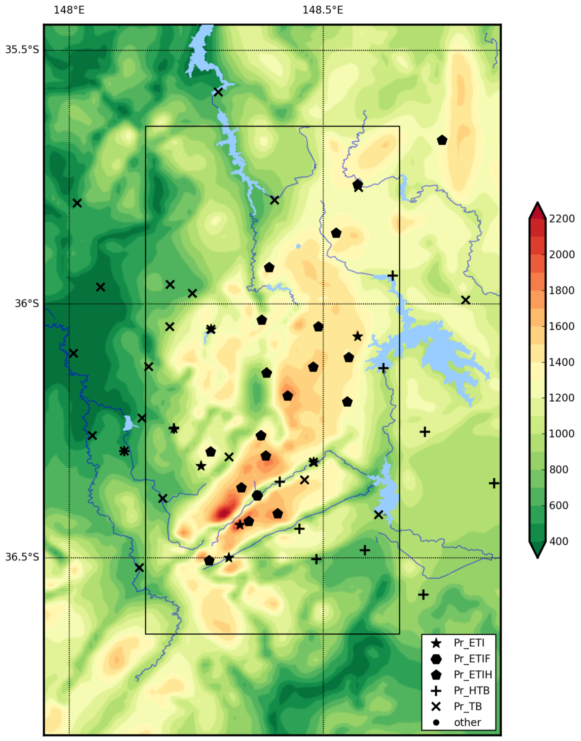

Figure 6.2: SPERP precipitation gauge network at May 2011. Installation of the additional gauges was begun in 2004 and continued through to 2006. Unfenced, Half-DFIR and Full-DFIR fenced ETI precipitation gauges are marked with stars, pentagons and hexagons respectively. The black rectangle shown is the analysis region discussed in this chapter.

6.1 Description of data sources

6.1.1 Analysis region and period

The analysis region was defined to be a 0.5°×1.0° latitude-longitude box, between 148.15° and 148.65° E, and 35.65° and 36.65° S, as shown in figure 6.2. This box defined the boundaries for inclusion of precipitation gauges and MODIS cloud retrievals. The analysis period was the winter months (May–September) of the five years 2005–2009.

6.1.2 Precipitation data

The precipitation data used in this analysis was collected during the Snowy Precipitation Enhancement Research Project (SPERP; Manton et al., 2011). A network of 44 gauges was used in this experiment to evaluate the impact of glaciogenic cloud seeding with silver iodide. The precipitation gauge network as at May 2011 is shown in figure 6.2.

The gauges used to perform the analyses described in this chapter were all of those depicted in figure 6.2 with an elevation of above 1000 m (see table A.2). When it was found that multiple gauges were operating at a single site (there were several instrumentation upgrades performed during the SPERP experimental period), only data from the most recently installed instrument was used. A total of 33 gauges were thus considered for the analysis, with a maximum of 29 operating at any one time. At least 10 were in operation for more than 99% of all hourly observations during the winter months in the analysis period.

Many of the gauges used to evaluate the SPERP were specialised, all-weather precipitation gauges, especially where frozen precipitation was regularly received. A number of these were situated in exposed locations, so to reduce the effect of under-catch in high winds, half-sized (6 m diameter) double wind fences were installed (marked with pentagons in figure 6.2). The SPERP gauges were maintained for the winter period only, with deployment during the month of April and decommission during the month of October so continuous observations in May–September were generally available. The data was provided for each gauge as half-hour accumulations in multiples of the gauge resolution, and has been averaged in two ways for this analysis:

1. Hourly average accumulation, where the data was averaged over all functioning gauges to represent precipitation associated with the hourly trajectories (section 6.1.3). The averaging period was from thirty minutes before to thirty minutes after each hour to centre it on the trajectory arrival time. This dataset was of sufficient temporal resolution to capture the effects of rapid meteorological changes.

2. Average precipitation rate, where the data was averaged over all functioning gauges to give an estimate of precipitation rate associated with each MODIS overpass (section 6.1.4). As the MODIS overpasses were irregular, the averaging period was three hours centred on the half-hour prior to the MODIS overpass. The longer averaging period used here was based on the approximate time that conditions seen by the satellite were assumed to persist.

Using an average calculated from a large number of gauges over a longer averaging period provides sensitivity to very low precipitation rates. Each gauge records an increment in precipitation when a threshold accumulation amount is reached (in the case of tipping bucked gauges, this was the amount required to overbalance the bucket assembly, while for the all-weather gauges it was software dependent). At low precipitation rates, the chances of recording a “tip” at a single gauge during a short interval were low, but when a few “tips” were averaged over the network, the precipitation was better represented. The drawback was that the average amount was also susceptible to erroneous data, that is, “false” tips. The data used here were part of a set that has been carefully quality controlled by the Snowy Hydro technicians for this type of error, but it was nonetheless of concern for this analysis.

6.1.3 HYSPLIT back trajectories

A detailed discussion of the use of back trajectories was given in chapter 5, where a 20-year climatology of back trajectories associated with precipitation was presented. To investigate the effect of aerosol pollution from remote sources on precipitation in the Snowy Mountains, the errors introduced in the trajectory calculations due to both interpolation and inadequate representation of flow around terrain become more important. Where ERA-Interim data was used to calculate the trajectories in chapter 5, forecast data from the Australian Mesoscale Limited Area Prediction System (MLAPS) was used. This model was run twice daily by the Australian Bureau of Meteorology, and was the highest resolution regular simulation for the five years of interest. The forecasts were provided three-hourly at a horizontal resolution of 0.125° on 29 vertical levels, with 14 levels below 3000 m. They were routinely converted into a format suitable for ingestion into HYSPLIT for operational use by the BOM.

Hourly back trajectories were calculated by running HYSPLIT in batch mode for each hour during the months of May–September in 2005–2009. As in chapter 5, the destination point was Mt Blue Calf. A total of 18 360 trajectory simulations were performed, with trajectories calculated at a number of levels, but only those arriving at (1000 m) were considered in this analysis.

Application of trajectories

Back trajectories were used in this analysis to provide a meteorological link between regions at a distance and conditions observed in the Snowy Mountains, specifically the impact of

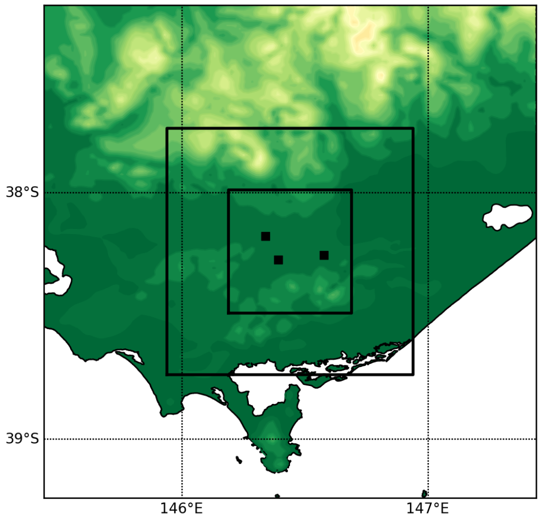

Figure 6.3: Example "source" and "nearby" region for the Latrobe Valley. Here the dimension of the "source" region was 0.5°, and the "nearby" region was 1.0°. The black squares show the location of Victoria's principal power stations.

pollution on cloud microphysics and precipitation. From the five-year climatology of trajectories, those that passed through a "source" region—a regular latitude-longitude box of side length l_s centred on a pre-determined pollution source as shown in figure 6.3—were selected from the climatology of MLAPS trajectories. Trajectories passing through a larger box, or the "nearby" region were selected separately. Trajectories that passed through the "source" were excluded from the "nearby" sample to ensure that no overlap existed between these sets. The dimensions of the regions used were varied as an experimental parameter, but the linear dimension l_n of the "nearby" region was always twice that of the "source" region. This means that any cross section through the centre will have equal parts in the "source" and "nearby" regions so that the trajectory sample sizes were similar.

The use of a "buffer" zone surrounding the source region was considered for this analysis, with the aim of providing a greater distinction between the "source" and "nearby" trajectories. It was found, in general, that the variability of the trajectory fields was on the same spatial scale as the source regions, so the necessary increase in size of the nearby region to accommodate a buffer served only to increase the noise in the comparisons between source and nearby regions.

"Capping" of source/nearby region

It was reasonably self-evident that for the air represented by a trajectory to be affected by a ground-based pollution source it must have passed relatively close to the surface. Strongly subsiding conditions, such as those following a very strong frontal passage, mean that the airmass at cloud height in the Snowy Mountains would be relatively pristine, despite potentially having passed over numerous pollution sources. The effect of capping the "source" and "nearby" regions, or requiring that trajectories pass below a given height threshold while in the region, was tested in this analysis, but the results presented in this chapter, unless specified otherwise, use a cap of 1 500 m above ground level. This is an elevation which is generally within the mixing layer, so surface emissions will be transported to this level by turbulent fluxes, but is not so low as to exclude overly many trajectories.

Conditioning of trajectories

This analysis relied on trajectories taking a reasonably direct route from the source/nearby region to the analysis region. The uncertainty in trajectories is linearly related to travel distance (Rolph and Draxler, 1990), and particularly under strongly dynamic conditions (such as a frontal passage) the uncertainties introduced may become very large. The simplest way to filter circuitous trajectories was to prescribe a minimum average travel speed between the source and the destination. Figure 6.4 illustrates the effect of prescribing an average speed of at least 30 $\mathrm{km\,hr^{-1}}$. A total of 2156 trajectories are depicted in the left panel, and of these 1307 meet the speed criteria and are depicted in the right panel. Importantly, all of the trajectories in the right panel travel directly between the source/nearby region and the destination point, so the filter was clearly effective.

Some of the "nearby" trajectories in figure 6.4 apparently travelled through the "source" region. This figure illustrates a sampling error, whereby air parcels travelling with sufficient speed may traverse the "source" region during the hourly interval on which they were recorded. This contamination was naturally of greatest concern for smaller "source" regions and is a reflection of the limitation of the sampling system used, but was expected to be small for regions with $l_s > 0.5°$. It could be removed altogether by interpolating between the

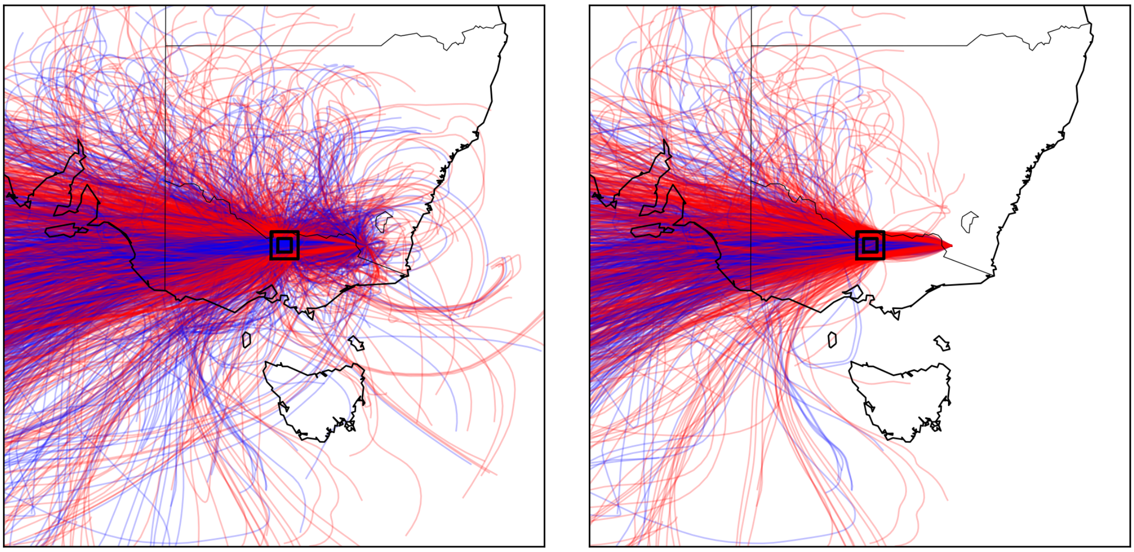

Figure 6.4: All trajectories passing through the source/nearby region (left) and those which meet the minimum speed criteria (right). Red trajectories pass through the “nearby” region only, while blue trajectories pass through the ”source” region.

output points on the trajectories, but the computational overhead to perform this was not considered to be justified.

Comments on fitness-for-purpose of trajectories for this application

The Lagrangian treatment of pollution transport by trajectories neglects some important factors. Firstly, sub-grid scale mechanisms of dispersion were ignored. In the horizontal sense, this was accounted for in the present analysis through the use of a “source” region, thereby representing diffusion with a degree of variability in the trajectory path. Uncertainties in the trajectory position were also handled by this approach, assuming the mean displacement error of the trajectories was not too large, and was centred on zero.

Due to wind shear in the lower levels of the atmosphere, small differences in the destination height of trajectories can lead to large differences in position after integration, potentially leading to ambiguity in the definition of “source” or “nearby” trajectories. The choice of 1 000 m AGL as the destination height for trajectories (as opposed to 500 m in chapter 5) reflects a trade-off between a trajectory that will pass near the surface for a pollution source, yet remain above the shear layer.

6.1.4 Cloud effective radius retrievals

Cloud effective radius

To characterise cloud reflectivity by a single cloud particle parameter rather than by the size distribution, the cloud droplet effective radius r_e was defined by Hansen and Travis (1974) as the area-weighted radius of cloud droplets:

$$r_e = \frac{\int_{r_1}^{r_2} \pi r^3 n(r)\,\mathrm{d}r}{\int_{r_1}^{r_2} \pi r^2 n(r)\,\mathrm{d}r}, \tag{6.1}$$

where $n(r)$ is the droplet size distribution and r is the droplet radius. The spherical albedo of the cloud droplets, which is related to the cloud reflectance, is sensitive to particle size in a number of near-infrared MODIS bands, where water vapour absorption is low (King et al., 1997). The effective radius is derived from the satellite radiances through the use of one of these bands (the choice depends on surface type), and a band which is absorbed by water vapour (Platnick et al., 2003) through the use of lookup tables to invert the relationship between r_e and cloud reflectance.

MODIS data

The Moderate Resolution Imaging Spectroradiometer (MODIS) instrument (Platnick et al., 2003) is currently operational on two Earth Observing System (EOS) satellites; the A-train Aqua satellite and the Terra satellite. Both of these satellites are in sun-synchronous orbit at an altitude of about 705 km, and together provide coverage of any given location approximately four times per day.

The MODIS instrument records radiances in 36 spectral bands, from visible light to mid-infrared radiation. These radiances (the “Level 1” data) were post-processed to produce a range of products including land, water vapour, aerosol and cloud properties. These products were available for free download from the NASA MODIS website[1]. The “Level 2” products were available as pixel-level “swath” data, which were essentially the result of the first processing step.

---

[1] http://modis.gsfc.nasa.gov/

The archived Level 2 Cloud Product data included cloud masks at both one and five kilometre resolution, as well as a selection of cloud top properties at five km resolution (temperature, pressure and thermodynamic phase), and optical properties at one km resolution (optical thickness, effective particle radius and water path). The resolution differences reflect the bands used to perform the retrievals; the optical (visible) bands provide the highest resolution, but the retrievals may only be performed for data with solar radiance (that is, captured during the daytime).

The Level 2 Cloud Product data was provided in a series of hierarchical data format files, each one representing scans of the MODIS instrument over about five minutes. Each variable was stored on a grid at the resolutions identified above. The axes of the grids are termed "along-swath", or parallel to the satellite's ground track, and "across-swath". For the one kilometre grid, there are 2030 pixels along the swath and 1354 pixels across the swath. It should be noted that due to the effect of the viewing angle, the pixels further from the centre of the swath become elongated, and especially towards the edges, some overlap occurs between successive scans.

The NASA MODIS website provides a search engine for the Level 2 products, where a region of interest and temporal period may be specified. The website returns a file list, and prepares the files for FTP transfer. For the analysis region specified in figure 6.2, all of the Level 2 Cloud Product data between 2005 and 2009 in the months of May–September were acquired.

Processing of MODIS data

As the analysis region was very small in comparison to the domain represented by each swathe file, only a small part of the data in each file was required. In order to accelerate the processing speed, the data was subdivided into "patches" that just covered the analysis region, as shown in figure 6.5. In the event that a division between successive swath retrievals occurred near the analysis region, the two retrievals were joined before subdivision. All of the resultant patches were stored in netcdf files, with one file per year for the one and five kilometre resolution variables, along with the latitude and longitude of the pixels for each swathe retrieval. As the across-swath resolution changes with viewing angle, the grid dimensions were different for each swathe retrieval. The dimensions of the variables in the netcdf files were selected to

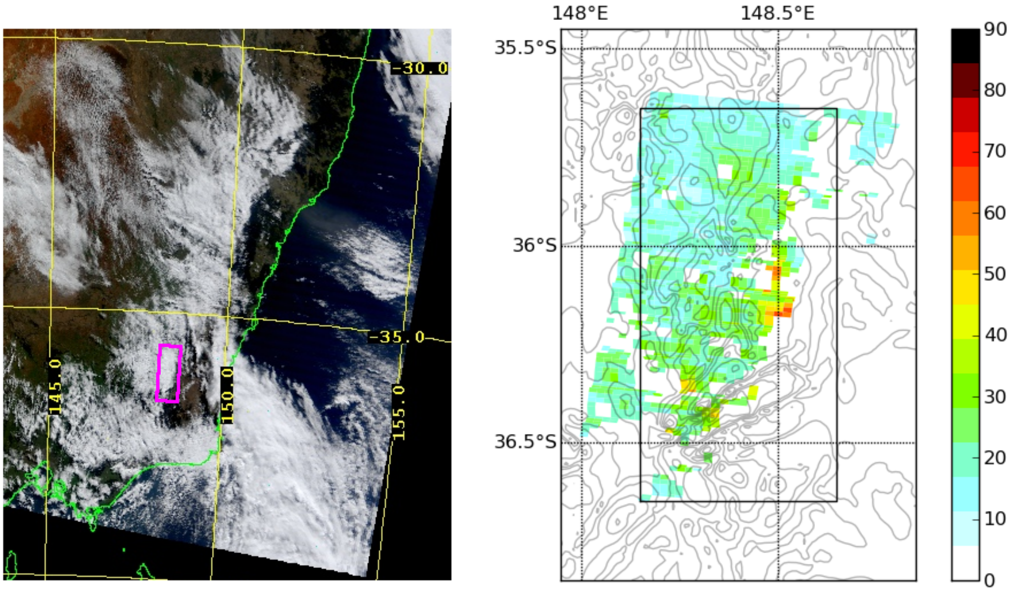

Figure 6.5: Example RGB rendering of a MODIS granule image for 00:35 UTC on 21/07/2008, and the Cloud Effective Radius "patch" extracted from the raw data. This example shows typical post frontal conditions for the region (it was selected from the July case in chapter 4). The magenta box in the left panel shows the analysis region for this chapter.

be larger than the maximum expected for any swathe retrieval, and fill values were applied to pad the data accordingly.

As the cloud effective radius algorithm is dependent on optical radiances, granules captured during the night time did not provide any information about particle size. The retrieval thus introduced a bias in the sense that no diurnal cycle was represented. Diabatic (i.e. solar) heating of the surface during the day time results in additional buoyancy which typically leads to cloud development, which would have obvious implications for cloud effective radius statistics. However, during wintertime at high elevation, snow cover over the majority of the terrain and reduced insolation would be expected to inhibit convection, so this impact was expected to be minimised.

Statistics from the patches were extracted for the analyses described in the following sections. As shown in figure 6.5, a sizeable proportion of the pixels in each patch may occur outside the analysis region, a side effect of subdividing the raw data. When the statistics were calculated, a binary mask was applied to these patches to exclude pixels that occur outside the boundaries of the analysis region. To ensure that the sample was representative of the whole analysis region, a lower threshold on the number of pixels within the analysis region was set. The threshold used was 1 000 pixels (out of a maximum possible of about 5 000). To establish that the scene was sufficiently "cloudy", at least 25% of the pixels within the analysis region were required to have a valid cloud effective radius value.

6.2 Pollution sources

6.2.1 Clouds and aerosol pollution

Of primary importance to the study of cloud physics is the formation of water droplets in the atmosphere in conditions of water vapour saturation. In the absence of a suitable particle to facilitate droplet nucleation, cloud drops may only grow as a result of chance agglomeration of water molecules (Pruppacher and Klett, 1997). The tiny embryos that are produced are generally unstable and subject to random disassociation at water vapour pressures below a critical value (which varies as a function of temperature). This *homogeneous* nucleation does not occur in the atmosphere because the presence of aerosol particles means that cloud droplets are initiated at much lower supersaturation than required for homogeneous nucleation. The supersaturation required for a given aerosol particle to nucleate a droplet depends on a number of factors including the particle constituency and size, as well as the ambient temperature (Twomey, 1977). Most particles ultimately support droplet nucleation at sufficient supersaturation, and those that do are termed "condensation nuclei" (CN).

Cloud condensation nuclei (CCN) are the subset of these aerosol particles which initiate droplet formation at low water vapour supersaturation ($\sim 0.1\%$–$\sim 10\%$). World-wide studies of CCN concentrations (Twomey and Wojciechowski, 1969) show substantial variation according to location, with a clear distinction found between maritime airmasses (including those that have been over land for a short time) and continental airmasses. The largest concentrations were found over dense urban environment and industrial complexes, as a result of emissions from a range of activities.

6.2.2 Aerosol pollution as a function of population

Ayers et al. (1982) established an empirical relationship between CN flux and population based on aircraft measurements downwind of 11 Australian towns of various sizes. The towns

“Source” name	Longitude	Latitude	Population	Notes
Port Augusta*	137.77	-32.48	13 257	Coal-fired electricity
Port Pirie*	138.02	-33.19	13 206	Lead smelting/refining
Sydney	151.21	-33.86	4 575 532	Largest NSW city
Melbourne	144.97	-37.81	4 077 036	Largest VIC city
Adelaide	138.60	-34.93	1 203 186	Largest SA city
Geelong	144.35	-38.15	178 650	Second largest VIC city
Ballarat	143.85	-37.55	96 097	Third largest VIC city
Bendigo	144.26	-36.75	91 713	Fourth largest VIC city
Canberra	149.12	-35.31	358 600	Largest inland population
Albury-Wodonga	146.92	-36.08	106 052	Nearest major upwind city
Shepparton,VIC	145.40	-36.38	49 859	Medium upwind town
Latrobe Valley†	146.44	-38.24	∼ 75 000	Coal-fired electricity

Table 6.1: Pollution “sources” specifically tested in this investigation. Population estimates are as at March 2010 from the Australian Bureau of statistics, except for those marked *, which are from the 2006 census; and †, which is from the Latrobe City council website.

ranged in population from 2 000 (Broome, W.A.), to 3 500 000 (the population of Sydney at the time). To a remarkable degree of fit, the relationship between CN flux F and population P in nuclei per second was given as:

$$F = 8.0 \times 10^{13} P \ (\mathrm{s}^{-1}). \tag{6.2}$$

The area of the town and the number of privately owned vehicles were found to be even better estimators for the CN flux, but the ease with which population statistics may be obtained makes it a more useful value.

A number of major population centres were located in regions upwind of the Snowy Mountains, and are included in table 6.1. The most notable of these is the city of Melbourne, with a current population of greater than 4 000 000. Melbourne lies directly on the axis of most frequent trajectory arrivals (see figure 5.4), which meant that it was frequently directly upwind of the Snowy Mountains. Indeed, a “pollution plume” emanating from this city was clearly identified as passing close to the Snowy Mountains by Rosenfeld (2000).

6.2.3 Pollution from industry

A selection of additional “point sources” were specifically considered in this analysis, as outlined in table 6.1. Pollution plumes from coal-fired electricity generation at Port Augusta and industrial activity in Port Pirie, among others, were explicitly identified by Rosenfeld (2000) as having an impact on nearby cloud microphysical characteristics. The more intensive electrical generation activities in the Latrobe Valley—where about 85% of Victoria's electricity is generated from lignite (brown coal) combustion—were identified as important in ensuing discussion (Rosenfeld et al., 2006). Both the direct particulate emissions and the gas-to-aerosol conversions (from NO_X and SO_2 emissions) which occur downwind were considered to have an impact on cloud effective radius observations. The four major generation plants in the Latrobe Valley are located within about 25 km of one another and were treated as an individual source in this analysis.

6.3 Cloud effective radius and surface precipitation

Central to the suggestion of Rosenfeld (2000) that precipitation amounts in the Snowy Mountains are affected by pollution is that the decrease in radar reflectivity in regions of low cloud r_e equates to a systematic and substantial surface precipitation reduction. The analysis presented in this section, investigates whether a connection between satellite-derived cloud r_e and surface precipitation can be established.

One of the major obstacles to such an investigation is that the high spatial and temporal variability of precipitation observations, combined with the infrequency of satellite overpasses means that it is difficult to make simultaneous observations of cloud r_e and surface precipitation. Performing such an analysis in a mountainous region like the Snowy Mountains goes some way to alleviating these problems. The increased frequency of precipitation and increased overall cloudiness meant that the number of cloud observations, and the likelihood of simultaneous precipitation measurements, was greater for this region. Furthermore, the orographic clouds that are the most common in these regions are stationary in nature, so a single overpass was representative of the averaging periods used to characterise precipitation rates.

6.3.1 Selecting suitable MODIS cloud retrievals

Cloud r_e median and quartile values were calculated over the analysis region shown in figure 6.2 if the domain coverage and cloudiness criteria outlined in section 6.1.4 were met. To exclude clouds such as high cirrus or frontal bands, it was additionally required that at least 85% of the cloudy pixels had a cloud top temperature (CTT) warmer than $-13°$ C. Combined, the cloudiness and CTT criteria guarantee that the scenarios considered were orographic in nature, and thus the type of cloud considered to be the most susceptible to precipitation suppression by pollution (Levin and Cotton, 2009).

The MODIS instrument captured data within the analysis region a total of 3 473 times during the winter months of 2005–2009. Of these overpasses, 1 903 swath retrievals met the domain coverage, cloudiness and CTT criteria. As the season of interest was winter, more than half of these occurred during the night, leaving 498 retrievals from which cloud r_e statistics were calculated.

6.3.2 Results of analysis

The relationship between the surface precipitation rate and cloud r_e is shown in figure 6.6, where $\widetilde{r_e}$ (the median value of r_e for an overpass) were plotted directly against the precipitation rate. Note that non-precipitating clouds were excluded from this figure as the x-axis scale is logarithmic. Wintertime values of cloud $\widetilde{r_e}$ for orographic clouds were generally between 10 and 25 μm. For negligible precipitation rates (below 0.01 $\mathrm{mm\,hr^{-1}}$), the values of $\widetilde{r_e}$ were low, with a mean value of less than 14 μm which corresponds with the findings of Rosenfeld and Gutman (1994) that precipitation was seldom observed in clouds with r_e below 12 μm. For $0.01 < P < 1.0$ $\mathrm{mm\,hr^{-1}}$, the binned values of $\widetilde{r_e}$ increased monotonically, and the correlation coefficient between $\widetilde{r_e}$ and P was about 0.38. This compares well with studies of the relationship between cloud top effective radius and ship/satellite radar retrievals of precipitation; for example Chen et al. (2008) found a correlation coefficient of 0.45 for these parameters within the south-eastern Pacific stratocumulus region.

Figure 6.7 shows histograms of $\widetilde{r_e}$ for all overpasses which meet the coverage and cloudiness criteria, including those for non-precipitating scenarios. Of 1903 overpasses that met domain

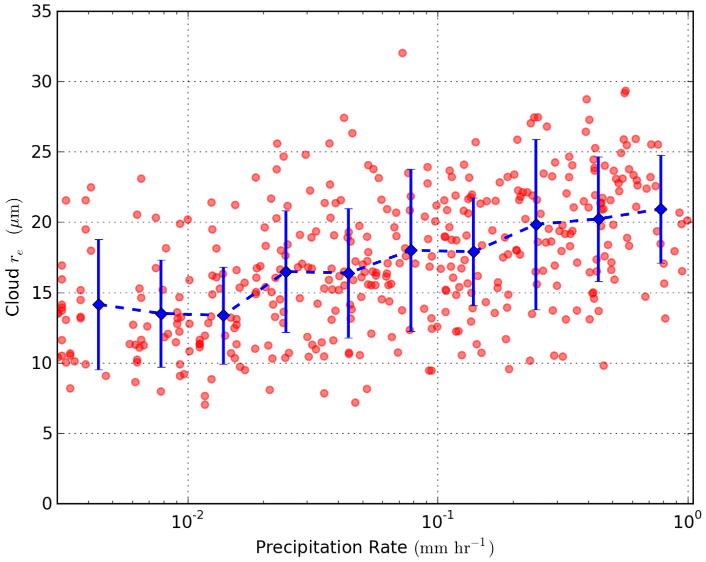

Figure 6.6: Scatter plot of median cloud r_e and surface precipitation rate (where it was greater than zero) during winter months in 2005–2009. Shown in blue are the mean and standard deviation of the median r_e values when partitioned by precipitation rate. Note the logarithmic scale of the x-axis. The correlation coefficient between the cloud $\widetilde{r_e}$ and precipitation rate was 0.376.

coverage, cloudiness and CTT requirements, median and quartile cloud r_e were calculated from 498 observations. The modal $\widetilde{r_e}$ was in the 15–17.5 μm band. The positive skewness of the distribution was evidenced by the wider distribution of the upper quartile compared to that of the lower quartile values. Examination of the individual cloudy scenes suggested that high r_e values occurred in isolated patches, such as might be expected from convective development.

On 827 occasions, no precipitation was recorded during the MODIS overpass, but only 77 of these occurred during the daytime and met the cloudiness criteria for inclusion. The distributions of $\widetilde{r_e}$ were much narrower, and the modal $\widetilde{r_e}$ values were in the 10–12.5 μm band, with a mean value of 12.54 μm. The slight positive skew of this distribution indicates that high r_e for non-precipitating clouds can exist, but these were quite rare.

Very light average precipitation rates ($0 < P \leq 0.1$ mm hr^{-1}) were often an indication of patchy precipitation, recorded at only a handful of the gauges or not sustained for the three-hour averaging period. This scenario was very frequent in the Snowy Mountains, accounting for nearly 50% of all of the MODIS r_e retrievals that met the cloudiness criteria. The mean

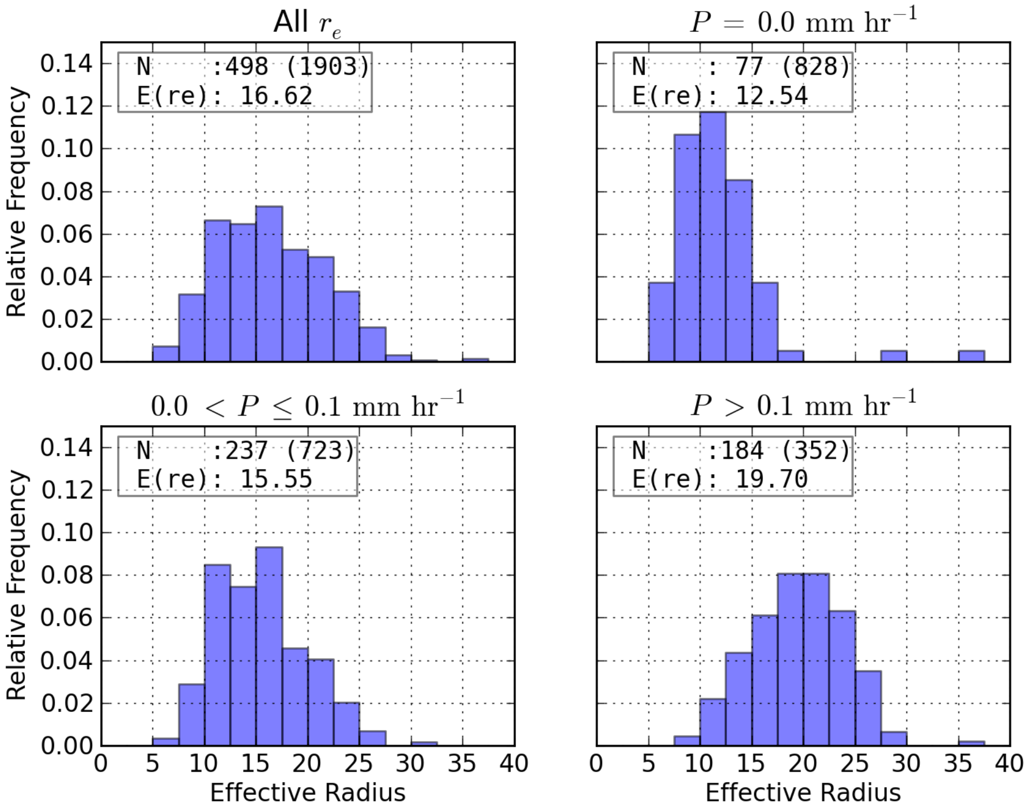

Figure 6.7: Histograms of median cloud r_e partitioned by precipitation rate. In boxes are N: the number of samples where a valid result for $\widetilde{r_e}$ was retrieved (in parentheses the total number of MODIS overpasses), and $E(r_e)$: the mean value of $\widetilde{r_e}$ for the distributions.

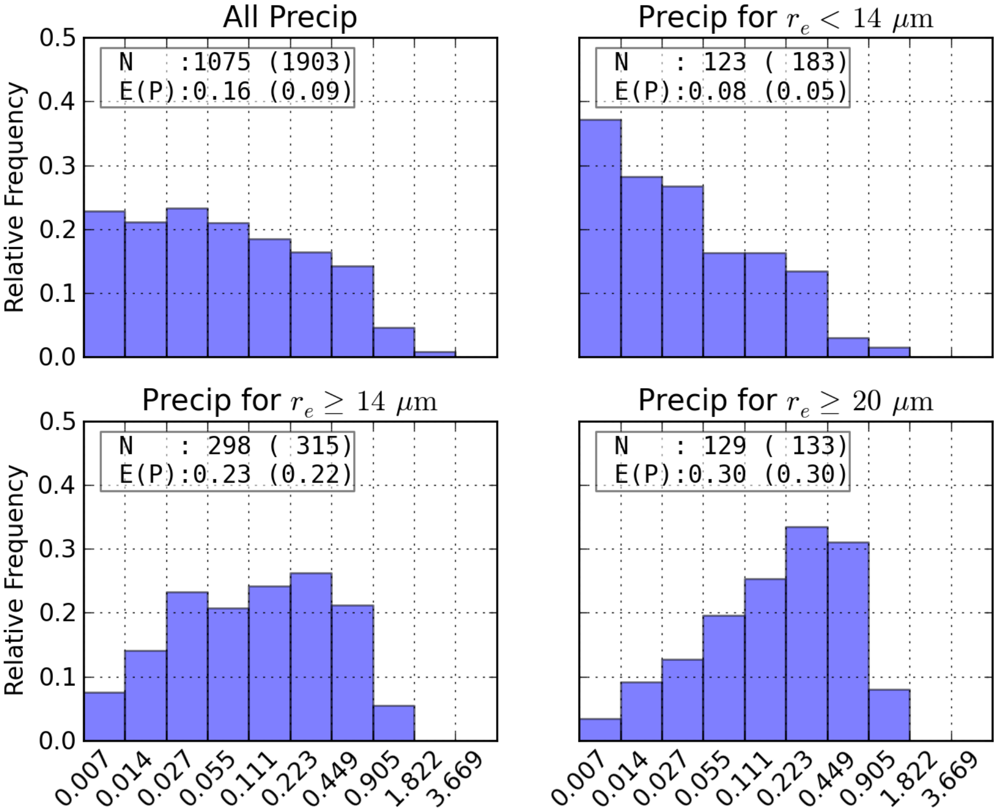

Figure 6.8: Histograms of precipitation rates partitioned by median cloud r_e. Note the exponential spacing of the precipitation rate bins (x-axes). In boxes are N: the number of samples where $P > 0$ (in parentheses the total number of precipitation observations), and $E(P)$: the mean precipitation amount for these samples. (in parentheses the mean for all observations)

value of $\widetilde{r_e}$ was about 3 μm greater than for the non-precipitating clouds. Clouds with higher precipitation rates ($P > 0.1$ mm hr^{-1}) show normally distributed values of $\widetilde{r_e}$, with a mean value of 19.7 μm, a further increase of 4 μm over the lightly precipitating clouds.

Figure 6.8 shows the converse of the previous discussion, with histograms of precipitation rates partitioned by median cloud r_e. The upper left panel shows the frequency of precipitation for 1 903 essentially random samples during wintertime; of these 1 075 (56%) of the three hour periods recorded precipitation, with a mean precipitation rate of about 0.09 (0.16) mm hr^{-1} for “all” (“wet”) samples. The distribution was truncated in this instance by the choice of precipitation bins, but for practical purposes precipitation rates of less than 0.01 mm hr^{-1} can be ignored.

Cloudy scenes with $\widetilde{r_e} < 14\ \mu$m were precipitating in 123 of 183 cases (67%), but the precipitation rates were extremely low. For scenes with $\widetilde{r_e} \geq 14$ μm, precipitation was recorded in 298 of 315 cases (95%), with an average precipitation rate of 0.22 $\mathrm{mm\,hr^{-1}}$ (from all samples), while for $\widetilde{r_e} \geq 20$ μm this value increases to 0.30 $\mathrm{mm\,hr^{-1}}$, with precipitation occurring in 97% of samples.

6.3.3 Summary of findings

The results presented in the section are consistent with well-established literature in cloud microphysics. Remotely-sensed precipitation observations have been used a number of times to validate the relationship between precipitation and cloud droplet effective radius, but the remarkable result in this section is that this has been shown to also hold true for surface precipitation. This result establishes the sensitivity of the surface precipitation observations to satellite-based cloud microphysical observations, as predicted by Rosenfeld (2000), and provides a context to continue in this investigation.

6.4 Cloud effective radius and back trajectory climatology

Back trajectories have been successfully used in source-receptor studies for some time, where observations of an atmospheric tracer or pollutant at a given site may be linked by the meteorology to a remote source location. The specific applications are widely varied, for example the attribution of air quality to desert dust (Escudero et al., 2006); pollution transport and deposition studies (Cohen et al., 2002); and identification of moisture sources important for precipitation (Hondula et al., 2010). This section presents a back trajectory method which demonstrates that one of the core assumptions in the hypothesis of Rosenfeld (2000)—that upwind aerosol pollution systematically and substantially modifies cloud structure in the Snowy Mountains—is not well founded.

6.4.1 Description of analysis

An objective test was devised to determine the impact of known pollution sources on the cloud microstructure in the analysis region. For all of the MODIS retrievals that met the coverage, cloudiness and CTT criteria outlined in the previous section, the MLAPS back trajectory arriving at 1000 m AGL on the nearest hour to the overpass time was selected. For a given pair of "source"/"nearby" regions, two mutually exclusive sets of MODIS r_e retrievals were defined for each of the source regions in table 6.1; those that were associated with trajectories passing through the "source" regions, and those passing "nearby". The distributions of cloud $\widetilde{r_e}$ over the analysis region were objectively compared with a two sample Kolmogorov–Smirnov (K–S) test to evaluate the null hypothesis that both samples were drawn from the same distribution, by providing a P-value for this scenario.

The difference in the *mean* of the distributions for $\widetilde{r_e}$ is a simple and physically meaningful statistic to evaluate the impact of a "source" region on cloud r_e in the Snowy Mountains:

$$\Delta\widetilde{r_e} = E(\widetilde{r_e})_s - E(\widetilde{r_e})_n. \tag{6.3}$$

This statistic was defined such that a negative value implies that the cloud r_e was reduced when a trajectory passes through the "source" region compared to when it passes through the nearby "region".

To characterise the natural variability within the statistics, some experiments were performed using gridded "source" regions. The analysis as described above was performed for each of the "pollution sources" in table 6.1, with the results compared to the gridded sources to evaluate whether a signal could be detected. Two values of l_s were considered for the gridded locations to assess the impact of varying the "source" region size.

6.4.2 Controlling for meteorological factors

Ayers (2005) pointed out that a possible confounding effect to the conclusion of Rosenfeld (2000) was that the dynamics of the different cloud systems were not accounted for. An adiabatic droplet growth ("parcel") model was used to illustrate the dependence of cloud droplet size distribution on updraft speed. Higher vertical velocities imply greater supersaturation of the atmosphere, so more CCN are expected to become activated, leading to higher droplet concentrations and consequently lower r_e.

To control for this factor, the optimum approach would be to use a convective indicator, such as convective available potential energy from a nearby regular sounding, to control for

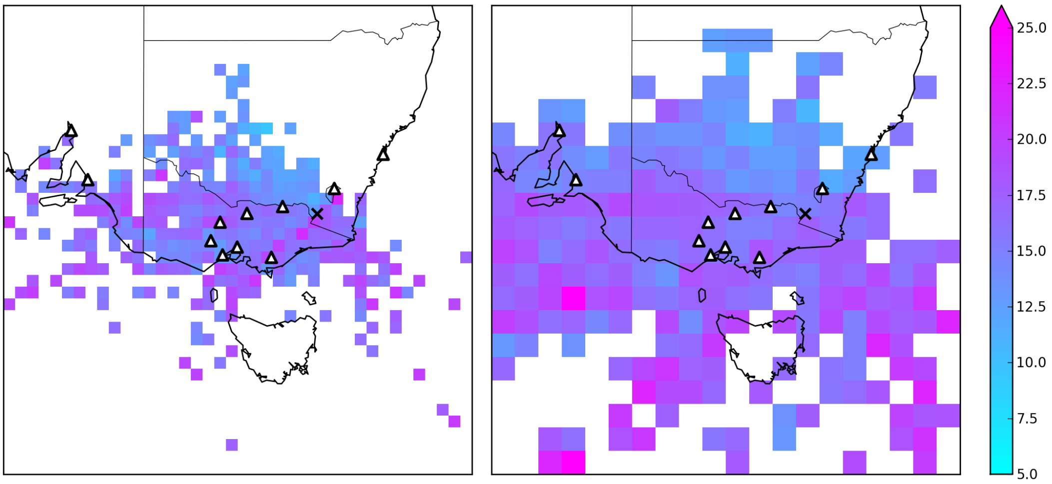

Figure 6.9: Median cloud effective radius ($\widetilde{r_e}$), given that a trajectory has passed though a gridded “source” region. Source region sizes were 0.5° (left) and 1.0° (right) and the location of specific pollution sources shown with small triangles.

excessively dynamical scenarios. In practice, this was not necessary given that stringent cloud criteria were already in place. The requirement for 85% of cloud tops in the analysis region to be warmer than $-13°$ C effectively rules out strong convective activity.

6.4.3 Results for gridded locations

Figure 6.9 shows the mean value of $\widetilde{r_e}$ given that a trajectory has passed through a gridded “source” region, using l_s values of 0.5° and 1.0°. The resolution of the grids used to locate the sources was the same as l_s, and each region required at least five back trajectories coincident with a MODIS r_e retrieval to be included in this figure. Naturally, the sample size was lower—and therefore the noise higher—for locations further from the Snowy Mountains region. More samples per source region were available for regions to the west of the Snowy Mountains for both values of l_s, indicative of the fact that the cloudiness criteria were most frequently met during westerly conditions.

It is not possible to say from the figure whether any of the marked pollution sources were having an impact on the values of $\widetilde{r_e}$, which is an indication that any signal was on the scale of the noise in the background. An interesting feature of this representation is a north-east to south-west gradient in $\widetilde{r_e}$, with generally lower values (10–12 μm) associated with regions in central NSW, and higher values (18–20 μm) over Victoria and the seas to the south of

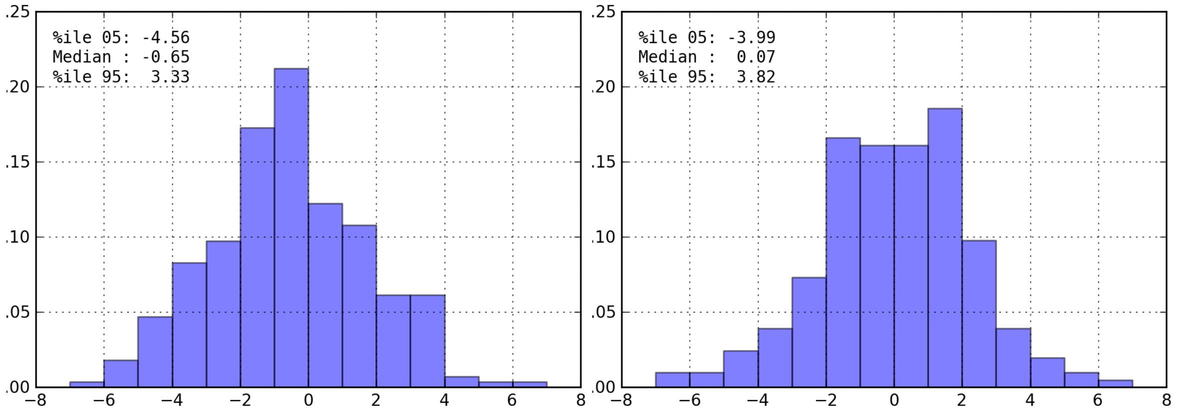

Figure 6.10: Histograms of $\Delta\widetilde{r}_e$ for gridded regions in figure 6.9. The 5th and 95th percentiles from the distributions are shown in the upper left of each panel, and are used as a means of identifying values that are significantly different from the population.

the continent. The seas to the south-east were also associated with high $\widetilde{r}_e$. Although not a clear indication of the aerosol content of the atmosphere, this observation is consistent with the understanding of the nature of clouds with continental/maritime origins.

Examining the variability in the test statistic $\Delta\widetilde{r}_e$ serves two important purposes. Firstly, the distribution of the statistic will characterise the natural variance that should be expected when assessing the impact of an individual pollution source, and secondly, any clear outliers that exist in the distribution will be identified. Figure 6.10 shows histograms representing the distributions of the test statistic $\Delta\widetilde{r}_e$ for the gridded locations shown in figure 6.9. They were normal in nature and have 5th and 95th percentiles as marked. There were no remarkable outliers requiring specific examination, but the spread in the distribution was large at both scales. For the 0.5° source regions, 5% of the values for $\Delta\widetilde{r}_e$ were below about -4.5. This difference was on par with the differences observed within and outside the plumes discussed by Rosenfeld (2000), and as such serves as a useful threshold for a difference that could be considered "substantial".

The locations of the points represented by the tails of the distribution in figure 6.10 are of general interest. Figure 6.11 shows the spatial distribution of $\Delta\widetilde{r}_e$. The first observation made was that none of the specified pollution sources were located within a gridded region showing a substantial value of $\Delta\widetilde{r}_e$ at either resolution (with the exception of Canberra, which is discussed later). Many of the extreme values occurred over the sea to the south, where

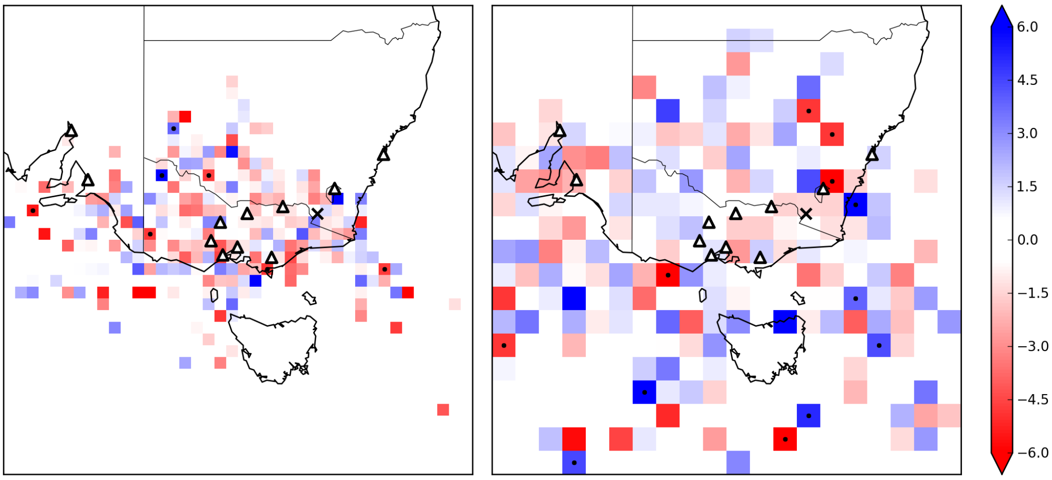

Figure 6.11: $\Delta\widetilde{r}_e$ (colours) for the gridded control regions used. Source region sizes were 0.5° (left) and 1.0° (right). The locations of regions with statistically significant $\Delta\widetilde{r}_e$ below the 5^{th} or above the 95^{th} percentile are shown with black dots.

the values of $\widetilde{r}_e$, and hence the noise, were greater than over land. Finally, there was little coherence between the two resolutions, which is an indication that the patterns seen here were predominantly noise.

The implication of the analysis of the background variability is that there was substantial noise in the test statistic $\Delta\widetilde{r}_e$. The 5^{th} and 95^{th} percentiles from the distributions serve as useful thresholds in deciding whether individual sources were “suspicious”. Additionally, figure 6.11 gives an indication of the required “source” region size that should be used to guarantee that sufficient samples were available. For a source very close to the Snowy Mountains (such as Albury-Wodonga), a small region was obviously preferable and would provide an adequate number of samples. For a more distant source, such as the city of Melbourne, a larger source region was needed for sample size. Other factors, such as how distributed the source was considered to be, must be taken into account when choosing the source region.

The use of a larger “source” region for more remote sources also allows for the dispersion of a plume as it was transported over a long distance, a factor which was not represented by back trajectories. Inaccuracies in trajectory position were also shown in chapter 5 to grow with path length, so the use of a larger source region to represent a more distant source takes this uncertainty into account. Larger regions can also include multiple discreet sources, which is appropriate given that plumes emanating from closely located sources will generally converge after some distance.

“Source” name	l_s	N_s/N_n	$E(\widetilde{r_e})_s$	$E(\widetilde{r_e})_n$	$\Delta\widetilde{r_e}$	P
Sydney	1.00	0/3	–	14.91	–	–
Canberra	0.50	1/9	14.46	17.42	-2.96	0.36
Albury-Wodonga	0.25	33/54	16.46	17.29	-0.82	0.41
Shepparton	0.50	33/51	20.74	17.11	3.63	0.00
Ballarat	0.50	11/35	15.22	17.44	-2.22	0.64
Bendigo	0.50	24/22	17.67	18.57	-0.90	0.89
Melbourne	0.50	26/32	17.55	15.37	2.18	0.39
Geelong	0.50	17/28	16.82	18.21	-1.39	0.39
Melbourne+Geelong	1.00	51/63	17.08	17.27	-0.19	0.85
Latrobe Valley	0.50	21/29	20.33	18.82	1.51	0.49
Adelaide	2.00	35/54	18.27	17.64	0.62	0.40
Eyre Industrial	2.00	13/20	16.76	15.26	1.50	0.35

Table 6.2: Results of basic analysis for back trajectories and cloud $\widetilde{r_e}$. The column labelled l_s is the side length of the “source region” (in degrees) used to select MODIS r_e retrievals (the “nearby” region was twice this value in all cases). N_s/N_n are the number of MODIS retrievals used, and $E(\widetilde{r_e})$ are the expected value (mean) of $\widetilde{r_e}$ for these retrievals. $\Delta\widetilde{r_e}$ is the test statistic, for which a negative (positive) value means reduced (increased) $\widetilde{r_e}$ when trajectories pass through the defined “source” region, and P is the P-value that the $\widetilde{r_e}$ means are drawn from the same distribution.

6.4.4 Results for selected pollution sources

Table 6.2 shows the results of the analysis for selected pollution “sources”. The values of l_s were selected based to achieve a reasonable number of samples, as well as to ensure all anticipated emissions sources were included within the defined region (for example, the Canberra source region was selected to include both Canberra and the nearby township of Queanbeyan). Trajectories were required to pass beneath 1 500 m while traversing the “source”/“target” regions.

A potential confounding mechanism to this analysis was the contamination of the “nearby” region for one pollution source with trajectories that pass through the “source” region of another. Melbourne and Geelong were likely to interact with one another this way, in a manner that would reduce the significance of this test. As the sources were closely located, it was appropriate to treat them as a single source with a larger source region, hence the inclusion of “Melbourne+Geelong” in table 6.2.

Choosing only trajectories that passed below 1 500 m had a minimal impact on the sample sizes for all sources except for Sydney and Canberra. Trajectories which approach from these regions were most likely to do so under the influence of a high pressure centre located over the Tasman Sea to the east, and were thus likely to be subsiding. A statistically significant result

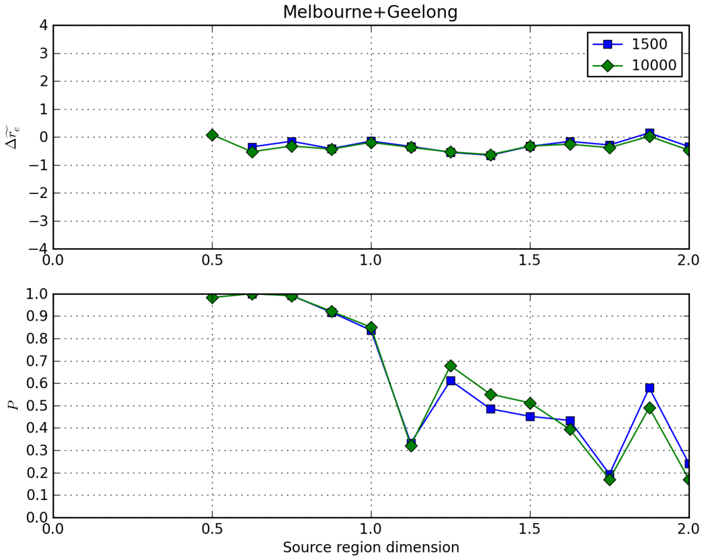

Figure 6.12: $\Delta\widetilde{r_e}$ (upper panel) and P-value (lower panel) for a range of l_s values, for trajectories capped at 1 500 m and 10 000 m (effectively the model ceiling), centred between Melbourne and Geelong

was found at the regional centre of Shepparton, with a value greater than the 95th percentile for the gridded distributions, but the positive sign implies that trajectories through this source were associated with higher values of r_e. The pollution sources of primary concern for the Snowy Mountains—Melbourne and the Latrobe Valley—show conflicting and statistically insignificant results. The combination of the Melbourne and Geelong source, which improves the differentiation between urban and rural surrounds, results in a less significant impact than for either of the two individual locations.

Variation of "source" region size

The effect of incrementally varying the value of l_s for each of these individual pollution sources was considered, as was the effect of removing the 1 500 m cap for selecting trajectories. In this section the two pollution sources considered to be of the greatest importance—the Melbourne/Geelong urban complex and the Latrobe Valley power generation plants—were presented; the results for the other sites are provided in appendix A.6.

The urban/industrial complex of Melbourne and Geelong is home to over 80% of Victoria's population, and was certainly the largest source of pollution to be found upwind of the Snowy

Mountains region. Figure 6.12 shows the change in $\Delta\widetilde{r_e}$ as l_s was increased from 0.25° to 2.0°, requiring at least 25 trajectories through the “source” region to perform the analysis. For no value of l_s were the differences statistically significant, so the null hypothesis—that pollution from Melbourne and Geelong has no impact on cloud microphysics in the Snowy Mountains—can not be ruled out in this test. In any case, the change in $\widetilde{r_e}$ was well within the noise range of values obtained from the gridded control “sources” in figure 6.11, so the impact, regardless of the statistical significance, would be inconsequential.

Another region of primary concern was the Latrobe Valley, both as a major aerosol pollution source as well as for its potential as a confounder for the Melbourne/Geelong samples. Air quality objectives were frequently exceeded in the Latrobe Valley as a result of the coal-fired electricity generation which occurs there (Kitwood, 2010). The electricity generation plants were located within a relatively short distance of one another, and the surrounding region is principally made up of rural communities or farmland, so it was for the purposes of this experiment an idealised “source” region. Figure 6.13 shows the same results as in figure 6.12, but for the Latrobe Valley region. A slight positive impact on cloud effective radius is found, but this is within the range of the expected background variability.

For all “source” regions with l_s between 0.5° and 2.0°, the value of $\Delta\widetilde{r_e}$ was positive, with statistical significance for regions greater than 0.75°. This indicates that trajectories passing directly through the source region were associated with larger cloud r_e than those passing nearby, contrary to what should be expected if pollution from this region was impacting cloud microphysical properties in the manner described by Rosenfeld (2000). Such an effect could potentially be explained if the “nearby” had been strongly contaminated by the Melbourne source, but the lack of an impact from there suggests that this was not the case.

In summary, there was no indication that anthropogenic pollution was having an impact above the background variability in $\widetilde{r_e}$ at any of the sites specified with the sole exception of Shepparton, which appears to have a strong *positive* impact on cloud effective radius. With no reasonable explanation as to why this should be the case, and no impact from the most significant sources of pollution in south-eastern Australia, the result for this source was considered to be an extreme value, consistent with the tails of the distributions shown in figure 6.10

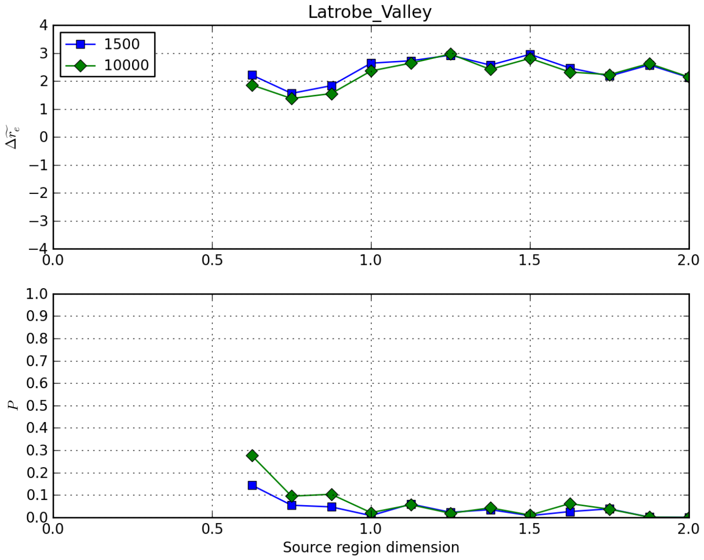

Figure 6.13: As for figure 6.12, but for the Latrobe Valley.

6.5 Back trajectories and precipitation

The final aspect that was considered in this analysis was whether a signal due to airmass history can be detected in the surface precipitation observations. An experiment similar in nature to that outlined in the previous section was proposed, whereby precipitation rates associated with trajectories which pass through “source” regions were tested against those associated with trajectories through surrounding “nearby” regions. The precipitation data, outlined in section 6.1.2 is a much denser dataset than the MODIS cloud retrievals, so the sample sizes in this analysis were substantially larger.

Two analyses were considered in this section. Firstly, the probability of recording *any* amount of precipitation given that a back-trajectory has travelled through a “source”/“nearby” region was used as a test statistic, then the *median* amount of precipitation, when it was observed, was considered separately. Neither analysis showed convincing evidence that precipitation was being suppressed when back trajectories were associated with the pollution sources considered.

6.5.1 Probability of receiving any amount of precipitation

Air pollution was hypothesized to "completely shut off precipitation" (Rosenfeld, 2000). This hypothesis was the most straightforward to test, and this was performed by comparing the probability P_s of observing precipitation coincident with the arrival of a trajectory which passes through some "source" region, with the probability P_n of observing precipitation when the trajectory passes through the surrounding "nearby" region. The significance of the difference ΔP_{sn} was evaluated with a two-tailed binomial test.

Threshold of detectability

Surface precipitation observations are discreet by the nature of the observational platform. The precision of the instruments deployed in the SPERP varies; for the tipping bucket gauges it is hardware-dependant, whereas for the all-weather gauges it is a parameter of calibration. In any case, it tends to be in the region of 0.25 mm. If the precipitation rate is similar to this amount, it tends to be poorly represented by a single gauge. The use of a dense network of gauges has the advantage of detectability of lower precipitation rates, but the disadvantage of being prone to "false tips". One way of addressing this is to require that at least two gauges record precipitation during the observational period. In a network of n gauges, each with a precision of 0.25 mm, the probability of detecting an area-averaged precipitation rate of p_r in any given hour is:

$$P_d = 1 - \sum_{k=1}^{2} \binom{n}{k} \left(1 - \frac{p_r}{0.25}\right)^k \left(\frac{p_r}{0.25}\right)^{(n-k)} \tag{6.4}$$

For a hypothetical network of ten gauges, the probability of detecting a precipitation rate of 0.1 $\mathrm{mm\,hr^{-1}}$ (a light drizzle) is about 0.954. It was found that during May–September in the years 2005–2009, at least 10 gauges were in operation recording half-hourly precipitation more than 99% of the time, so a threshold of detectability of 0.1 $\mathrm{mm\,hr^{-1}}$ was considered appropriate. Hours with precipitation recorded below this rate, or precipitation observations from only a single gauge, were ignored for this part of the analysis. During the 2005–2009 analysis period there were 18 360 one-hour observational periods. Of these, 10 535 were "zero precipitation" hours, 4 086 met the conditions required for a "rainy" precipitation observation

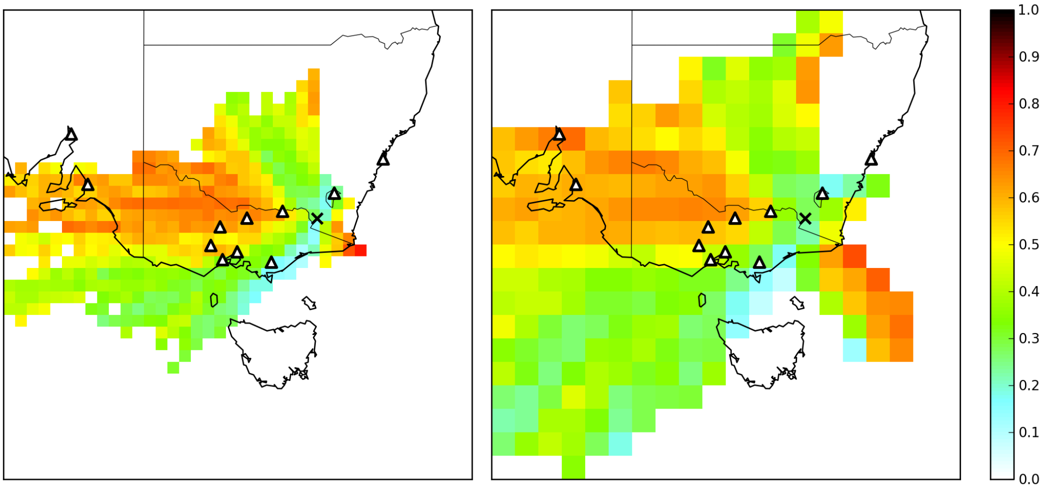

Figure 6.14: Probability of recording precipitation in the Snowy Mountains, given that a trajectory has passed through a gridded region (0.5° and 1.0° shown). At least 100 observations were required for representation in this figure.

and 3 739 were considered "ambiguous" because either only one gauge reported precipitation or the average amount was less than 0.1 mm.

Using these criteria, the probability P_s of observing precipitation, given a "source" trajectory, was defined simply as the number of "rainy" precipitation observations divided by the number of "zero" observations.

Background variability

The value of P_s was calculated for gridded locations at resolutions of 0.5° and 1.0°, requiring at least 100 trajectories to pass through the region. The resultant fields of P_s are shown in figure 6.14. Most important for precipitation was the sector to the west; as discussed in chapter 5, this direction was associated with orographic uplift over the Snowy Mountains. There was also a south-easterly corridor through which trajectories were frequently associated with precipitation, but trajectories from this direction are not common. They are most likely associated with low pressure systems over the Tasman Sea, which are climatologically common but relatively unimportant to the wintertime precipitation totals in the Snowy Mountains, as discussed in chapter 3. Another region of influence is apparent to the north, which is associated with the western slopes of the GDR. This feature may speculatively be associated with a low level pre-frontal jet, similar to that which occurs in the Sierra Nevada (Neiman

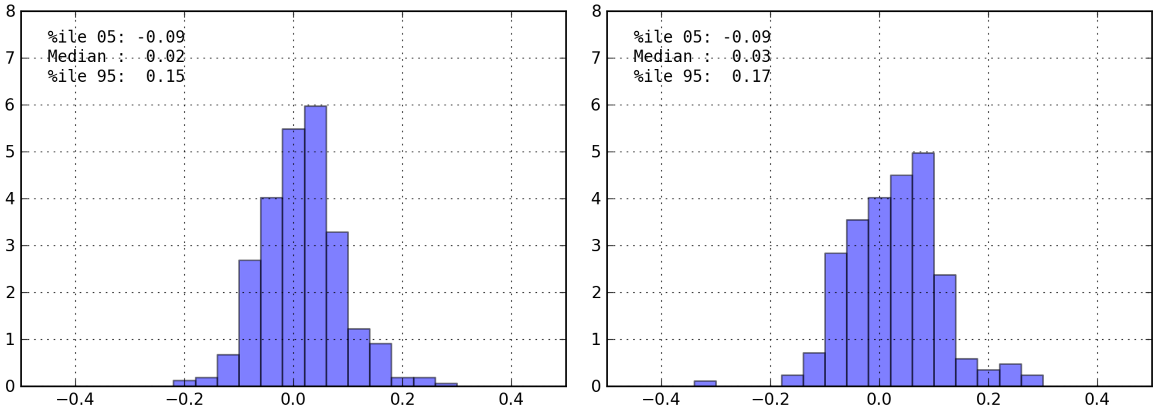

Figure 6.15: Histograms of the values shown in figure 6.16. The 5th and 95th percentile values are indicated.

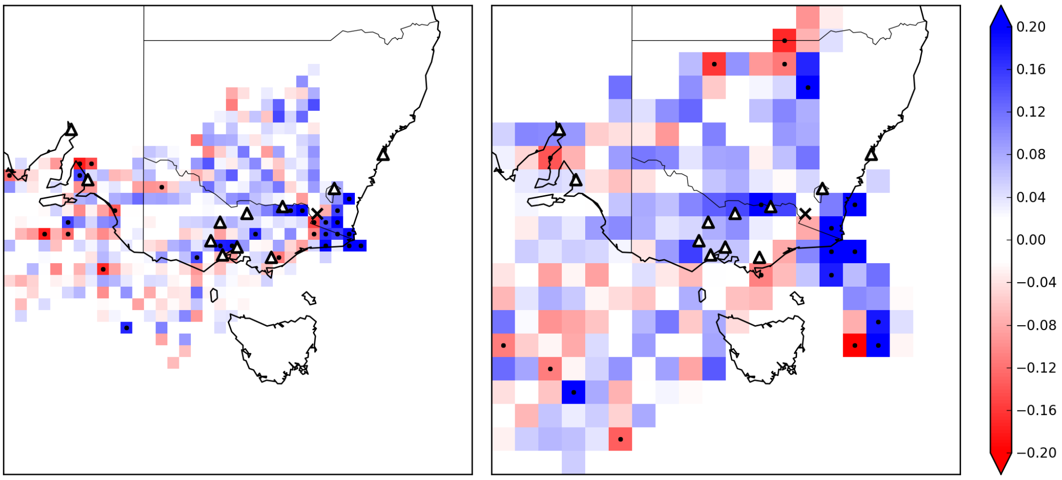

Figure 6.16: Difference between probability of recording precipitation for "source" trajectories (from figure 6.14) and "nearby" trajectories. The locations of regions with statistically significant ΔP_{sn} below the 5th or above the 95th percentile are shown with black dots.

et al., 2010), but the existence of such a feature has yet to be established locally.

Large differences in the values for P_s in adjacent grid squares in figure 6.14 suggest that the natural variability of the test statistic ΔP_{sn} was large, as this value was effectively the result of differentiating the P_s field. Figure 6.15 shows the distribution of this statistic for all of the gridded locations, with the 5th and 95th percentile values indicated. The tails of these distributions were considered with reference to the spatial distribution of ΔP_{sn}, which is shown in figure 6.16.

A strong suppression of precipitation due to a factor such as aerosol pollution would have been apparent as a negative outlier in the distributions in figure 6.15. For the 0.5° sources the tails were well formed and no such outliers were evident. The largest (positive) values mostly occurred to the south-east of the analysis region, due to the high gradients in the P_s field associated with the south-easterly corridor. The negative tail of the distribution was primarily associated with noise at the western fringe of the P_s field.

For the 1.0° sources, the spread was similar, but there were some outliers. The most important had a value of -0.307, occurring in the Tasman Sea some distance to the east of Tasmania, and thus could not be attributed to anthropogenic factors. This point was located with the fringe of the south-easterly corridor, which was also where the highest values of ΔP_{sn} were found, again due to the high gradients in P_s found in this region. The other extreme values were found to the far north, where the region of influence to the west of the GDR was located.

The 5^{th} percentile value for the distributions of the gridded values for ΔP_{sn} again served as a threshold for the identification of impacts considered to be suspicious. Source regions with values of $\Delta P_{sn} < -0.09$ could be treated as displaying a strong negative impact on precipitation frequency in the Snowy Mountains. Differences lower than this can not definitively be attributed to factors other than natural variability. For a source such as the Latrobe Valley, this difference would have been about 20% of the value of P_s, clearly a substantial reduction.

Result of the analysis for specified pollution sources

The test was applied to the pollution sources in table 6.1. Several of the results were statistically significant, but only three show a negative impact (i.e. consistent with the hypothesis that pollution from these sources was suppressing precipitation in the Snowy Mountains), and of these only Geelong has a statistically significant impact. This impact was substantially smaller (in an absolute sense) than the 5^{th} percentile value for the gridded regions, so it was considered to be within the noise level of the test.

The combined Melbourne/Geelong, Melbourne, Sydney and Eyre Peninsula sources return statistically significant, positive values of ΔP_{sn}. All of the values were below the 95^{th} percentile, so there was no need to speculate further than to say that these were within the noise level of the test. Melbourne and Geelong were near the southern fringe of the westerly corridor, which may explain the difference in sign between these locations, and the Eyre Peninsula

"Source" name	l_s	N_s/N_n	P_s	P_n	ΔP_{sn}	P
Sydney	1.00	67/89	0.343	0.236	0.107	0.044
Canberra	0.50	152/275	0.191	0.171	0.020	0.518
Albury-Wodonga	0.25	521/1201	0.536	0.568	-0.032	0.144
Shepparton	0.50	557/750	0.636	0.621	0.014	0.512
Ballarat	0.50	176/301	0.511	0.542	-0.030	0.450
Bendigo	0.50	320/398	0.603	0.560	0.043	0.128
Melbourne	0.50	307/466	0.482	0.399	0.083	0.004
Geelong	0.50	266/424	0.372	0.436	-0.064	0.036
Melbourne+Geelong	1.00	723/896	0.422	0.340	0.081	0.000
Latrobe Valley	0.50	353/628	0.297	0.255	0.043	0.067
Adelaide	1.00	356/364	0.601	0.574	0.027	0.309
Eyre Industrial	1.00	123/142	0.707	0.570	0.137	0.003

Table 6.3: Probability of observing precipitation given a source (P_s) or nearby (P_n) trajectory. The difference is given by ΔP_{sn}, and the P-value from the binomial test is given by P. As previously, l_s is the side length "source" region and N_s/N_n are the number of source and nearby trajectories.

was centrally located within this corridor, so it appears to be a local maximum in ΔP_{sn}.

The effect of varying the source region size was tested in the same manner as for the effective radius retrievals, and were provided in appendix A.7. The most remarkable result from these tests was that the results for Adelaide show a statistically significant, but weak, negative impact for a source region size of $l_s \sim 1.75°$. Canberra shows a strong impact, but only for values of l_s that would mean the analysis region was incorporated into the "nearby" region; clearly not a meaningful result.

In summary, the tails of the distribution for the test statistic have been examined and outliers explained, and thresholds for the expected level of natural variability in the test statistic ΔP_{sn} have been established. The specified pollution sources return values that were neither remarkable compared to the spread of the gridded values, nor signed such that they were consistent with the hypothesis that pollution from these sources may suppress precipitation. These results lead to the conclusion that, according to the test described in this section, no signal in the frequency of recording precipitation in the Snowy Mountains due to anthropogenic pollution can be detected: a null result.

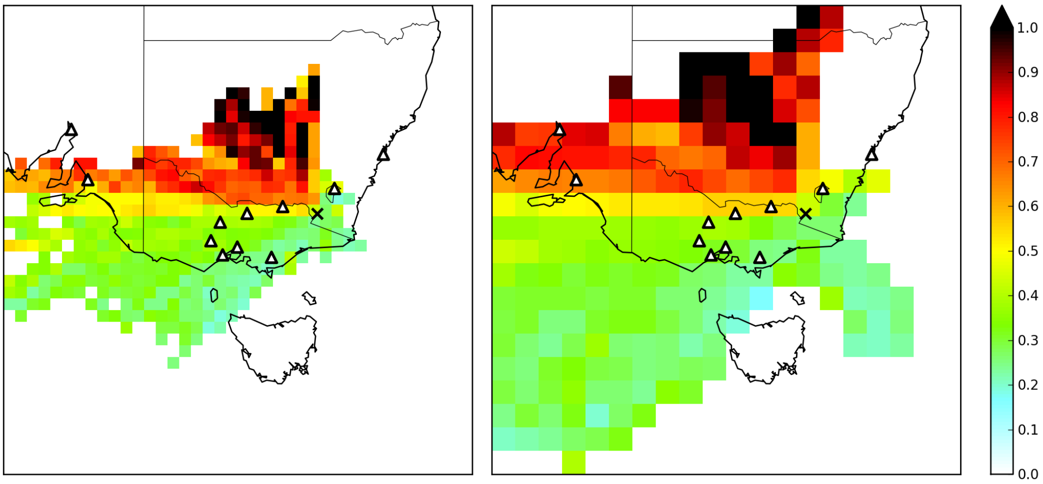

Figure 6.17: Median Snowy Mountains precipitation amount from precipitation observations where the mean hourly accumulation was greater than 0.1 mm, given that a trajectory has passed through a gridded region (0.5° and 1.0° shown).

6.5.2 Median precipitation amount

Precipitation was observed very frequently in the Snowy Mountains during the winters of 2005–2009, with average hourly precipitation amounts across the entire network (with at least two gauges recording a "tip") of at least 0.1 mm observed in 22% of all hours. The median amount—more representative than the mean due to the inherent skewness of the distribution—from a total of 4 086 precipitation observations, was 0.44 mm. With this relatively large population, it was feasible to perform a comparison of the distributions of hourly precipitation amounts for source/target trajectories.

The most suitable statistic to compare the distributions was to use the median precipitation amounts $\widetilde{R}_s$ and $\widetilde{R}_n$ for the source and target distributions respectively. The difference between these values, $\Delta\widetilde{R}_{sn}$, was defined such that a negative value implies that the median precipitation amount associated with trajectories which pass through the "source" region was lower than that for trajectories through the "nearby" region.

Gridded results

Once again the analysis proceeded by investigating the background variability of $\widetilde{R}_s$. Figure 6.17 shows the median precipitation amount, given that a 1 000 m trajectory has passed through the gridded regions considered in the previous sections. The patterns are quite

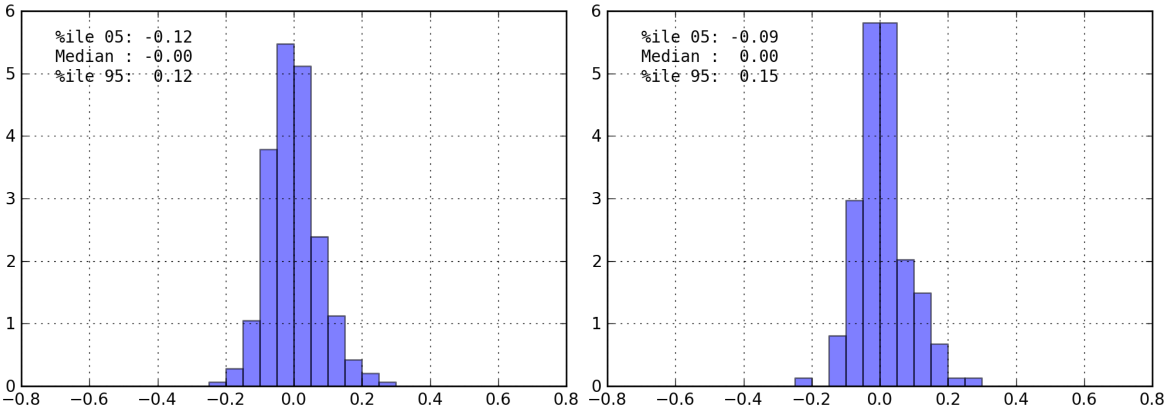

Figure 6.18: Histograms of difference in median precipitation amount for "source" trajectories (from figure 6.17) and "nearby" trajectories, but only for regions south of 35° S.

different to those for the probability of observing precipitation (figure 6.14). The heaviest precipitation was associated with trajectories from the north, related to the warm conveyor belt ahead of a cold front as discussed in chapter 5. Trajectories which passed through the state of Victoria were generally associated with median precipitation amounts of less than 0.5 mm. The south-eastern corridor over the Tasman Sea, which was associated with a high relative frequency of precipitation, was shown to bring relatively small amounts, reinforcing that precipitation from this sector was not important climatologically to the Snowy Mountains.

There was a high level of noise to the north-west apparent in figure 6.17 due to the higher precipitation amounts and lower frequency of precipitation observations. Since there were no pollution sources under examination in this region, it was most appropriate to exclude it from the analysis of the background variability (meaning that effectively only post-frontal precipitation is included). The histograms in figure 6.18 show the distributions for the test statistic $\Delta\widetilde{R}_{sn}$ for gridded regions to the south of 35° S, which was more representative of the field for the pollution sources under investigation in this thesis. The spatial variability of $\Delta\widetilde{R}_{sn}$, including the northern locations, is shown in figure 6.19

The tails of the distributions for $\Delta\widetilde{R}_{sn}$ were again found to be well-formed. The most substantial negative outlier in the 1.0° degree field was located on the southern NSW coast, far removed from any potential pollution sources. Positive extreme values were located along the north-western Victorian border, where the effect of the north-western regions becomes

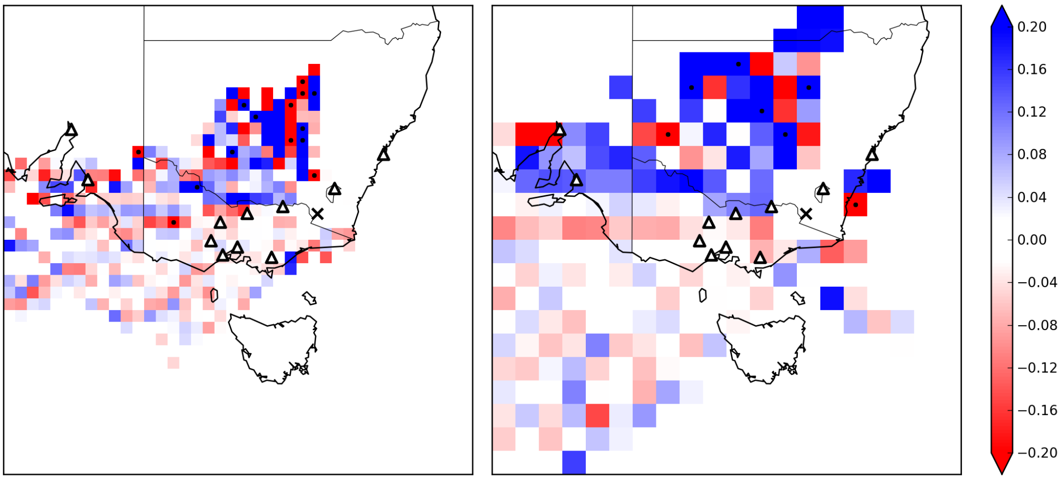

Figure 6.19: Difference in median precipitation amount for “source” and “nearby” trajectories. The locations of regions with statistically significant $\Delta\widetilde{R}_{sn}$ below the 5th or above the 95th percentile are shown with black dots.

apparent. The 5th percentile values for the 0.5° and 1.0° resolution gridded locations were -0.12 and -0.09 respectively.

Results for specified pollution sources

Table 6.4 shows the results for the pollution sources specified in table 6.1. Statistically significant results were seen for Canberra, Shepparton and Adelaide. The Canberra “source” trajectories were associated with a substantially higher median precipitation amount than the “nearby” sample, as well as a slightly higher frequency of observed precipitation, but the noise from the surrounding region and the relatively low number of samples make it difficult to rule out the effects of the background variability for this source. Adelaide also appears to have a strongly positive influence on the median precipitation amount. Its location in a region of high gradient (increasing northwards) of $\widetilde{R}_s$, while in this region Snowy Mountains back trajectory frequency increases to the south-east (figure 5.4), suggesting that there would be a bias to lower median precipitation amount, explaining the significant result. Shepparton was the only source with a statistically significant negative impact, but this impact was only about half the value of the 5th percentile, so there was no reason to attribute this to any other factor than the variability of $\widetilde{R}_s$. At any rate, it would be impossible to attribute the reduced precipitation amount for trajectories through this source to anthropogenic pollution, given that the major pollution sources in southern Victoria show much smaller, inconsistently

"Source" name	l_s	N_s/N_n	$\widetilde{R}_s$	$\widetilde{R}_n$	$\Delta\widetilde{R}_{sn}$	P
Sydney	1.00	23/21	0.548	0.250	0.298	0.185
Canberra	0.50	29/47	0.548	0.250	0.299	0.010
Albury-Wodonga	0.25	279/682	0.574	0.556	0.018	0.951
Shepparton	0.50	354/466	0.457	0.520	-0.063	0.024
Ballarat	0.50	90/163	0.329	0.370	-0.042	0.118
Bendigo	0.50	193/223	0.394	0.431	-0.037	0.963
Melbourne	0.50	148/186	0.333	0.316	0.017	0.471
Geelong	0.50	99/185	0.329	0.309	0.020	0.667
Melbourne+Geelong	1.00	305/305	0.316	0.309	0.006	0.996
Latrobe Valley	0.50	105/160	0.233	0.242	-0.010	0.958
Adelaide	1.00	214/209	0.710	0.513	0.197	0.007
Eyre Industrial	1.00	87/81	0.787	0.833	-0.047	0.695

Table 6.4: Median precipitation amount given a source ($\widetilde{R}_s$) or nearby ($\widetilde{R}_n$) trajectory. The difference is given by $\Delta\widetilde{R}_{sn}$, and the P-value from the K–S test is given by P. As previously, l_s is the side length "source" region and N_s/N_n are the number of source and nearby trajectories.

signed, statistically insignificant results.

Once again, the analysis has been performed by varying the source region dimension l_s for each of the sites, and the results are shown in appendix A.8. There was some ambiguity in these results, as for very large source regions ($l_s \geq 1.75°$), the value of $\Delta\widetilde{R}_{sn}$ for Melbourne reaches values of around -0.15, and the value for the Latrobe Valley reaches -0.10 for $l_s \sim 1.0°$. These values would both be considered significantly different to the background variability, but in both cases the "source" region size required to obtain these values was much larger than was required to differentiate between the urban/industrial pollution sources and the surrounds. The values were again better explained by natural variability; a 3.5° "nearby" region centred on Melbourne extends across the entire state of Victoria, into the region to the north which has been shown to be associated with higher precipitation rates.

The need for further work to test the sensitivity of this test was highlighted by this result. Modification of the precipitation record to simulate the effect of a hypothetical pollution source would be an appropriate way to do this. The sensitivity to the source region dimensions could also be investigated in this manner, and would provide a useful guide in the selection of source/nearby region dimensions.

The conclusion that must be drawn from these results is that no impact consistent with the suppression of precipitation due to the sources tested can be identified. The inconsistency in the sign, and the lack of statistical significance for the most important pollution sources implies that the values found can be attributed to the natural variability of the test statistic.

6.6 Can precipitation suppression due to anthropogenic aerosol pollution be detected using back trajectories?

The analysis presented in this chapter draws on a number of different datasets in order to assess the hypothesis of Rosenfeld (2000) that pollution from sources such as the city of Melbourne, the coal-fired electricity generation plants, and a number of others, is important in governing precipitation amounts in the Snowy Mountains. Using surface precipitation measurements from a dense, quality controlled network of gauges, it was shown that the microphysical characteristics of precipitating and non-precipitating clouds could be distinguished from MODIS cloud droplet effective radius retrievals. Using back trajectories to provide a meteorological link between potential sources and the Snowy Mountains analysis region, the effect of the sources being located directly upwind was tested on both cloud microphysical characteristics and surface precipitation amount.

6.6.1 Cloud effective radius and surface precipitation

The relationship between cloud effective radius and precipitation rate has been previously investigated through combining satellite-based radar and radiometer observations. Notably, it has been found that precipitation rates were lower in clouds with lower r_e, and may be completely suppressed when the droplet size falls below about 14 μm. From five years of wintertime observations, with a total of 498 MODIS retrievals during orographic cloud conditions, the relationship between surface precipitation and cloud $\widetilde{r_e}$ can be observed.

Non-precipitating clouds had a mean value of $\widetilde{r_e}$ of about 12.5 μm, for lightly precipitating (< 0.1 mm hr^{-1}) clouds the value was 15.5 μm and for higher precipitation rates the mean $\widetilde{r_e}$ was almost of 20 μm. This result gives some credibility to the hypothesis of Rosenfeld (2000), in that if pollution can be shown to reduce cloud effective radius in a consistent manner, it is feasible that precipitation is being suppressed. Furthermore, the ability of MODIS to discern between precipitating and non-precipitating clouds validates the fitness for purpose of the application of these observations in the current analysis.

6.6.2 Cloud effective radius and back trajectories

A back trajectory method to assess whether pollution from urban and industrial sources has a significant impact on cloud microphysical structure in the Snowy Mountains has been presented in this section. When scenes viewed by MODIS were deemed suitable to perform cloud effective radius (r_e) retrievals, the back trajectory arriving on the nearest hour was used to determine whether the airmass was affected by a pollution "source". The distributions of median r_e were compared to those when the back trajectory passed through the "nearby", or control, region to determine whether there was a statistically significant impact.

The statistic used to evaluate the impact was $\Delta\widetilde{r_e}$, the difference in the mean of the distribution of median r_e for the "source" and "nearby" samples. The P-value from the Kolmogorov-Smirnov test used to compare the distributions was used to evaluate the significance of this difference. The test was applied to a selection of pollution sources that have been identified as potentially being important to precipitation in the Snowy Mountains. The results were, generally speaking, statistically insignificant as well as being within the expected range of variability based on the results from the gridded control "sources".

The major sources of pollution—Melbourne/Geelong urban area and the Latrobe Valley electricity generation plants—were examined more closely. Tuning the Melbourne/Geelong source region returned a small and statistically insignificant result for all values of l_s tested. Further, the value for $\Delta\widetilde{r_e}$ for the Latrobe Valley sources—which represent the most ideal case for this test—was of the opposite sign to what would be expected were aerosol pollution playing a systematic and substantial role in cloud microphysics in the Snowy Mountains.

The small sample sizes and associated noise were of primary concern in this analysis. There were only 51 MODIS retrievals associated with a back trajectory through the "source" region of $1^\circ \times 1^\circ$ covering the Melbourne/Geelong urban region, and 63 for the "nearby" region. There is some scope for increasing the sample size beyond that which has been considered here. The analysis period for this investigation was based on the availability of the high-quality precipitation data available in the Snowy Mountains since the commencement of the SPERP in 2005, and only covers the winter months of May–September. It would be possible to increase the analysis period to include data from 2002, when both of the MODIS platforms were in operation, to the present date, as well as to extend the season by a month at either end to include April and October. This would increase the sample size by a factor of more than two. This has not yet been performed due to time constraints but is certainly considered relevant for future work on this topic.

6.6.3 Surface precipitation and back trajectories

The most direct measure for whether pollution was affecting precipitation amounts in the Snowy Mountains was to test whether any impact can be seen when the pollution source was located directly upwind. This was performed by comparing both the *probability of observing precipitation* and the *median precipitation amount* given a “source” or “nearby” trajectory. Applying the test to gridded locations, it was found that there was a good deal of background variability for both test statistics, which ultimately meant that the impact would need to be quite large in order to be unequivocally attributed to some factor in the source region. Although some statistically significant results were returned, the sign of these results was not found to be consistent with the suppression of precipitation, and the magnitude was insufficient to rule out the effect of the natural variability.

6.6.4 Summary and scope for future work

One aspect of this work that had yet to be performed is the simulation of a pollution source, whereby the precipitation or the microphysical record was modified when a trajectory passed through the source region. A degree of randomness could be incorporated into this type of analysis, to account for the impact of trajectory errors and also the variability of any aerosol impact. This would serve as a sensitivity analysis, and the ability of the methods presented in this chapter to detect true suppression would be verified.

There is plenty of scope for future work in this topic. Clearly, the consideration of alternative analysis regions, where major pollution sources were more directly upwind, would provide more conclusive results. A case-based approach, where some pollution source was intermittently upwind of the analysis region, would also provide useful insight. Numerical simulation of pollution plumes may potentially be validated against cloud r_e retrievals to enhance the understanding of the downwind impacts on clouds. However, the results presented in this chapter provide a representation of many events over a long period, and it is the most fit-for-purpose analysis to assess whether there is a systematic impact of aerosol pollution on precipitation amount.

A positive result for both a microphysical and surface precipitation impact would have been a very strong finding, providing a demonstrable link between pollution and precipitation. However, the analysis conducted in this thesis draws a null result in both cases for all potential pollution sources. In summary, the results presented in this chapter imply that any impact of pollution on precipitation in the Snowy Mountains, as assessed by the test statistics, clearly plays a second fiddle to the natural variability.

Chapter 7

Summary

The study of precipitation in the Snowy Mountains is of general interest because of its unique alpine environment and its importance as the source of major rivers which feed into the Murray-Darling Basin. The recent drought in south-eastern Australia has had a particular impact in the Snowy Mountains, as demonstrated by an analysis of precipitation from an independent gauge network.

Changes in the nature of synoptic systems were investigated in the context of this decline. Precipitation from cut-off lows, which approached the region north of 45° S, were shown to have a strong declining trend over the two decades considered. Two recent examples of such storms were considered in detail to assess the capacity of the Weather Research and Forecasting (WRF) model's ability to simulate precipitation in these events, and to evaluate the importance of the post-frontal period in governing precipitation amounts.

Back trajectories were used as an investigative tool for two purposes in this thesis; to illustrate the way moisture is transported to the Snowy Mountains during precipitation, and to directly address recent claims of precipitation suppression due to anthropogenic pollution.

7.1 Wintertime precipitation in the Snowy Mountains

Reliable precipitation records from the Snowy Mountains date back to the mid-1950's, when construction of the Snowy Mountains Hydro-electric Scheme began. A daily precipitation record at Guthega Power Station (GPS) and Cabramurra (CAB) in the Snowy Mountains has been constructed by merging overlapping data from different instruments located at the same sites, providing data to the end of 2009. To address the impact of missing days in the more recent data due to the introduction of automated gauges, data from the GPS gauge was used to estimate precipitation amounts at CAB.

This data has been used to evaluate the impact of the recent drought in the Snowy Mountains. A decrease of 19% is evident in the annual precipitation amounts, and for the wintertime (May–September), the decline was about 22%. These amounts are substantially higher than those found in general in south-eastern Australia, where declines of 14–15% were evident.

Wintertime precipitation in the most recent two decades (1990–2009) was considered in greater detail. Grouping observations from the increasingly dense network available in the Snowy Mountains, and using Bureau of Meteorology gauges to the west and east for comparison, an analysis of the trends in precipitation amounts was performed. A strong decline in precipitation is evident on the western slopes as well as at high elevation. the relationship between precipitation decline and elevation/annual precipitation was investigated on a gauge-by-gauge basis. The fact that the most significant relationship is between the *absolute* decline and elevation suggests that orographic factors are controlling the enhancement of precipitation over the lower gauges (compared to the eastern gauges), as well as the decline observed during the analysis period.

7.2 Synoptic decomposition of wintertime precipitation

Wintertime precipitation in the Snowy Mountains was decomposed into two major categories:

- Cut-off lows with minima in MSLP or 500 hPa height located north of 45° S, accounting for 56% of total precipitation, and 43% of all precipitation events.
- Embedded lows, in the circumpolar westerly belt south of 45° S, accounting for 40% of total precipitation and 47% of all precipitation events.

About 59% of precipitation events (accounting for 79% of precipitation) were associated with a cold frontal passage over the region. Over the twenty year period, embedded lows were more frequent than cut-off lows in all months except July, but cut-off lows brought more precipitation than embedded lows in every month except August.

Pook et al. (2006) noted that the statistic of rainfall per station per cut-off day declined over the period of their analysis (1970–2002) for north western Victoria and this climatology finds a similar result for the period from 1990–2009. The decline in wintertime precipitation over the 20 year analysis period was found to be about 40%, and this was mostly apparent in precipitation intensity, especially from cut-off lows. Although there are no trends in the frequency of either embedded or cut-off lows, the number of precipitating systems associated with a frontal passage was estimated to have declined by about 18%. Both of these results are consistent with the hypothesis that observed trends in intensity of the subtropical ridge (Larsen and Nicholls, 2009) or Southern Annular Mode (Nicholls, 2010) can cause changes in the paths followed by mid-latitude storms.

7.3 Case studies of orographic influence on clouds and precipitation in south-eastern Australia

A detailed discussion of the available observations during two typical wintertime storms in the winter of 2008 has been presented. High resolution numerical simulations with the WRF model match the observations remarkably well and have been used to provide a more complete picture of the nature of these storms. The two case studies provide an in-depth picture of the nature of wintertime storms in the Brindabella Ranges, and it is likely that the insights gained from this work are applicable more broadly in the alpine regions of south-eastern Australia.

The two events offer some contrast as the July event arose from a stronger cut-off low with a well-defined frontal passage. This event was characterised by greater accumulated precipitation (40 mm) and deeper clouds during the post-frontal orographic periods of precipitation. The August case study could be characterised by a very weak front tied to a weak cut-off low and less total precipitation (16 mm). In both of the case studies, total precipitation amounts recorded at Mt Ginini were approximately double those recorded at Wagga Wagga, consistent with the climatology of monthly precipitation for these sites for winter (May–September) of the years 2004–2010. The duration of precipitation was longer at the mountain-top site, where post-frontal orographic uplift plays an important role. Precipitation at Isabella Plains appears to be controlled by the orography upwind of the site, as it is located in the rain shadow of the Brindabella ranges.

The predominance of supercooled liquid phase clouds in winter as observed by the MODIS instrument is supported by both surface-based microwave radiometer observations and WRF model simulations. To establish the relationship between these cloud conditions and surface precipitation, additional work should be performed. Consideration of a large number of precipitation events over several winters would be necessary, and data from a more reliable precipitation gauge network is essential to making more general conclusions.

7.4 Back trajectories during wintertime precipitation events

Back trajectories provide useful insight into synoptic transport of moisture for precipitation. The climatology of low-level trajectories arriving in the alpine regions of the Snowy Mountains highlights the following key features:

- Moisture during wintertime precipitation arrives at low levels via two principal routes: a direct west-north-west corridor and a circuitous northerly corridor. Both of these corridors become more pronounced for higher precipitation rates.
- Enhancement of precipitation from the west-north-west is principally linked to orography, as this flow is aligned with the terrain gradient.
- The Southern Annular Mode plays an important role in the pattern of trajectories associated with precipitation. Negative (positive) phases of the SAM show a greater (reduced) contribution of the westerly stream to precipitation amounts.
- Enhancement of precipitation for trajectories arriving from the north is linked to moisture transport from the north-eastern subtropical sea surface by the warm conveyor mechanism associated with cold fronts.

While the analysis presented in this thesis only applied to trajectories in the Snowy Mountains, it was also considered (although in less depth) for other alpine regions. The picture was found to be largely similar along the western flanks of the Great Dividing Range, but a sharply contrasting picture was found for the southern end of the ranges.

7.5 Identification of precipitation suppression using back trajectory methods

The hypothesis that anthropogenic aerosol pollution from large urban and industrial centres was tested for the Snowy Mountains region, which has been identified as one of the most likely places in the world where such an effect could be detected. The analysis presented in this thesis draws on a number of different datasets, including high-quality surface precipitation observations, satellite-based microphysics retrievals and back trajectories calculated from the mesoscale Limited Area Prediction System, which is operated by the Australian Bureau of Meteorology. It was shown that the microphysical characteristics of precipitating and non-precipitating clouds could be distinguished from MODIS cloud droplet effective radius retrievals. However, the airmass history was not found to be linked to any of the test statistics proposed for cloud microphysics, probability of recording precipitation or median precipitation amount. This null result acknowledges that an impact may be detected in particular case studies, but in the long term the background variability is the dominant factor.

7.6 Closing remarks

There are a number of aspects that have been raised in this thesis that warrant further investigation. An interesting supplement to the synoptic climatology of chapter 3 would be the use of an objective approach, perhaps in the form of a principal component analysis, to objectively type the MSLP or upper level fields. Although this type of approach lacks the additional information included in the manual analyses, more weight could be placed on the significance of any trends disclosed by the procedure.

The numerical modelling of the two case studies in chapter 4 showed that post frontal precipitation was substantial in the alpine regions, and that shallow, supercooled liquid phase predominated. The nature of these clouds is of general interest to the meteorological community. The life cycle and extent of these clouds, and the proportion of wintertime precipitation that they contribute are two questions that arise from this research. Future numerical simulation, with focus on validation from satellite and radar observations, would lead to enhanced understanding of these clearly important cloud systems.

Insight was given to the transport of moisture during precipitation events in chapter 5, but the analysis could be enhanced substantially by the consideration of moisture budgets along the length of the back trajectories. Instead of simply identifying the corridors, the moisture sources would be pinpointed more explicitly by such an approach.

Chapter 6 is far from the final word on the potential for aerosol pollution to suppress precipitation. It is an interesting analysis that directly tests the hypothesis in question, but as with any analysis there is room for improvement.

Bibliography

ABS, 2008: Water and the Murray-Darling Basin - A Statistical Profile, 2000-01 to 2005-06. Tech. Rep. 4610.0.55.007, Australian Bureau of Statistics. Viewed September 27, 2011.

Alpert, P., N. Halfon, and Z. Levin, 2008: Does Air Pollution Really Suppress Precipitation in Israel? *Journal of Applied Meteorology and Climatology*, **47**, 933.

Ayers, G., 2005: Air pollution and climate change: Has air pollution suppressed rainfall over Australia? *Clean Air and Environmental Quality*, **39 (2)**, 51–57.

Ayers, G., 2009: Air pollution and precipitation suppression over SE Australia: A critical review of evidence presented by Rosenfeld (2000) and Rosenfeld (2006). *Tellus B*, **61 (4)**, 685–693.

Ayers, G., E. Bigg, D. Turvey, and M. Manton, 1982: Urban influence on condensation nuclei over a continent. *Atmospheric Environment*, **16 (5)**, 951 – 954.

Berry, G., 2011: Personal Communication.

Berry, G., M. J. Reeder, and C. Jakob, 2011: A global climatology of atmospheric fronts. *Geophysical Research Letters*, **38**, L04 809.

Boers, R. and P. B. Krummel, 1998: Microphysical properties of boundary layer clouds over the Southern Ocean during ACE 1. *Journal of Geophysical Research*, **103**, 16 651–16 664.

Browning, K., 1986: Conceptual models of precipitation systems. *Weather and Forecasting*, **1 (1)**, 23–41.

Budin, G., 1985: Interannual variability of Australian snowfall. *Australian Meteorological Magazine*, **33 (3)**, 145–159.

Chen, R., R. Wood, Z. Li, R. Ferraro, and F.-L. Chang, 2008: Studying the vertical variation of cloud droplet effective radius using ship and space-borne remote sensing data. *Journal of Geophysical Research (Atmospheres)*, **113**, D00A02.

Cohen, M. D., et al., 2002: Modeling the atmospheric transport and deposition of pcdd/f to the great lakes. *Environmental Science & Technology*, **36 (22)**, 4831–4845.

Cotton, W. R., 1972: Numerical simulation of precipitation development in supercooled cumulipart i. *Monthly Weather Review*, **100 (11)**, 757–763.

Draxler, R. and G. Hess, 1998a: An overview of the HYSPLIT_4 modelling system for trajectories, dispersion and deposition. *Australian Meteorological Magazine*, **47 (4)**, 295–308.

Draxler, R. and G. Hess, 1998b: Description of the HYSPLIT_4 modelling system. Tech. rep., Air Resources Laboratory, Silver Spring, Maryland.

Draxler, R. and A. Taylor, 1982: Horizontal Dispersion Parameters for Long-Range Transport Modeling. *Journal of Applied Meteorology*, **21 (3)**, 367–372.

Eagan, R. C., P. V. Hobbs, and L. F. Radke, 1974a: Measurements of cloud condensation nuclei and cloud droplet size distributions in the vicinity of forest fires. *Journal of Applied Meteorology*, **13 (5)**, 553–557.

Eagan, R. C., P. V. Hobbs, and L. F. Radke, 1974b: Particle emissions from a large kraft paper mill and their effects on the microstructure of warm clouds. *Journal of Applied Meteorology*, **13 (5)**, 535–552.

Escudero, M., A. Stein, R. R. Draxler, X. Querol, A. Alastuey, S. Castillo, and A. Avila, 2006: Determination of the contribution of northern Africa dust source areas to PM10 concentrations over the central Iberian Peninsula using the Hybrid Single-Particle Lagrangian Integrated Trajectory model (HYSPLIT) model. *Journal of Geophysical Research*, **111 (D06210)**.

Fuenzalida, H. A., R. Sánchez, and R. D. Garreaud, 2005: A climatology of cutoff lows in the Southern Hemisphere. *Journal of Geophysical Research (Atmospheres)*, **110**, D18 101.

Givati, A. and D. Rosenfeld, 2004: Quantifying precipitation suppression due to air pollution. *Journal of Applied Meteorology*, **43**.

Givati, A. and D. Rosenfeld, 2009: Comments on "Does Air Pollution Really Suppress Precipitation in Israel?". *Journal of Applied Meteorology and Climatology*, **48 (8)**, 1733–1750.

Hansen, J. E. and L. D. Travis, 1974: Light Scattering In Planetary Atmospheres. *Space Science Reviews*, **16 (4)**, 527–610.

Holland, G., A. Lynch, and L. Leslie, 1987: Australian East Coast Cyclones. Part I: Synoptic Overview and Case Study. *Monthly Weather Review*, **115 (12)**, 3024–3036.

Hondula, D., et al., 2010: A back-trajectory and air mass climatology for the Northern Shenandoah Valley, USA. *International Journal of Climatology*, **30 (4)**, 569–581.

Houze, R., 1993: *Cloud Dynamics*. San Diego Academic Press.

Ikeda, K., R. Rasmussen, W. Hall, and G. Thompson, 2007: Observations of Freezing Drizzle in Extratropical Cyclonic Storms during IMPROVE-2. *Journal of Atmospheric Science*, **64**, 3016–3043.

Kahl, J. and P. Samson, 1986: Uncertainty in trajectory calculations due to low resolution meteorological data. *Journal of Climate and Applied Meteorology*, **25**, 1816–1831.

King, M., S. Tsay, S. Platnick, M. Wang, and K. Luoi, 1997: Cloud Retrieval Algorithms for MODIS: Optical Thickness, Effective Particle Radius, and Thermodynamic Phase. Tech. rep., NASA Goddard Space Flight Center, Greenbelt, Maryland 20771.

Kitwood, M., 2010: Latrobe Valley Air Monitoring Network Annual Summary for 2009. Tech. rep., Advanced Technology Centre, Aurecon Australia, Callaghan NSW.

Kraus, E. B. and P. Squires, 1947: Experiments on the Stimulation of Clouds to Produce Rain. *Nature*, **159**, 489–491.

Kusunoki, K., M. Murakami, M. Hoshimoto, N. Orikasa, Y. Yamada, H. Mizuno, K. Hamazu, and H. Watanabe, 2004: The Characteristics and Evolution of Orographic Snow Clouds under Weak Cold Advection. *Monthly Weather Review*, **132**, 174–191.

Landvogt, P., J. Bye, and T. Lane, 2008: An investigation of recent orographic precipitation events in northeast victoria. *Australian Meteorological Magazine*, **57**.

Larsen, S. H. and N. Nicholls, 2009: Southern Australian rainfall and the subtropical ridge: Variations, interrelationships, and trends. *Geophysical Research Letters*, **36**, L08 708.

Lavery, B., G. Joung, and N. Nicholls, 1997: An extended high-quality historical rainfall dataset for Australia. *Australian Meteorological Magazine*, **46**, 27–38.

Levin, Z. and W. Cotton, 2009: *Aerosol Pollution Impact on Precipitation: A Scientific Review*. Springer Netherlands, 295-300 pp.

Lin, Y.-L., R. D. Farley, and H. D. Orville, 1983: Bulk Parameterization of the Snow Field in a Cloud Model. *Journal of Applied Meteorology*, **22**, 1065–1092.

Manton, M. and L. Warren, 2011: A Confirmatory Snowfall Enhancement Project in the Snowy Mountains of Australia – Part 2: Primary and Associated Analyses. *Journal of Applied Meteorology and Climatology*.

Manton, M., L. Warren, S. Kenyon, A. Peace, S. Bilish, and K. Kemsley, 2011: A Confirmatory Snowfall Enhancement Project in the Snowy Mountains of Australia – Part 1: Project Design and Response Variables. *Journal of Applied Meteorology and Climatology*.

Mellor, G. and T. Yamada, 1982: Development of a turbulence closure model for geophysical fluid problems. *Reviews of Geophysics and Space Physics*, **20**, 851–875.

Meyers, G., P. McIntosh, L. Pigot, and M. Pook, 2007: The Years of El Niño, La Niña, and Interactions with the Tropical Indian Ocean. *Journal of Climate*, **20**, 2872–2880.

Morrison, A., S. Siems, and M. Manton, 2011: A three-year climatology of cloud-top phase over the southern ocean and north pacific. *Journal of Climate*, **24 (9)**, 2405–2418.

Morrison, A., S. Siems, M. Manton, and A. Nazarov, 2010: A Modeling Case Study of Mixed-Phase Clouds over the Southern Ocean and Tasmania. *Monthly Weather Review*, **138 (3)**, 839–862.

Morrison, A. E., S. T. Siems, M. J. Manton, and A. Nazarov, 2009: On the Analysis of a Cloud Seeding Dataset over Tasmania. *Journal of Applied Meteorology and Climatology*, **48**, 1267–+.

Mossop, S. C. and J. Hallett, 1974: Ice Crystal Concentration in Cumulus Clouds: Influence of the Drop Spectrum. *Science*, **186**, 632–634.

Murphy, B. F. and B. Timbal, 2008: A review of recent climate variability and climate change in southeastern Australia. *International Journal of Climatology*, **28 (7)**, 859–879.

Murray, R. J. and I. Simmonds, 1991a: A numerical scheme for tracking cyclone centres from digital data. Part I: Development and operation of the scheme. *Australian Meteorological Magazine*, **39**, 155–166.

Murray, R. J. and I. Simmonds, 1991b: A numerical scheme for tracking cyclone centres from digital data. Part II: Application to January and July general circulation model simulations. *Australian Meteorological Magazine*, **39**, 167–180.

Neiman, P. J., E. M. Sukovich, F. M. Ralph, and M. Hughes, 2010: A seven-year wind profiler-based climatology of the windward barrier jet along california's northern sierra nevada. *Monthly Weather Review*, **138 (4)**, 1206–1233.

Nicholls, N., 2005: Climate variability, climate change, and the Australian snow season. *Australian Meteorological Magazine*, **54**, 177–185.

Nicholls, N., 2010: Local and remote causes of the southern Australian autumn-winter rainfall decline, 1958-2007. *Climate Dynamics*, **34 (6)**, 835–845.

Petterssen, S., 1940: *Weather Analysis and Forecasting.* Mcgraw-Hill, New York, 221-223 pp.

Platnick, S., M. King, S. Ackerman, W. Menzel, B. Baum, J. Riedi, and R. Frey, 2003: The MODIS cloud products: Algorithms and examples from Terra. *IEEE Transactions on Geoscience and Remote Sensing*, **41 (2)**, 459–473.

Politovich, M. K. and B. C. Bernstein, 1995: Production and Depletion of Supercooled Liquid Water in a Colorado Winter Storm. *Journal of Applied Meteorology*, **34**, 2631–2648.

Pook, M., P. McIntosh, and G. Meyers, 2006: The synoptic decomposition of cool-season rainfall in the Southeastern Australian cropping region. *Journal Of Applied Meteorology And Climatology*, **45 (8)**, 1156–1170.

Pruppacher, H. and J. Klett, 1997: *Microphysics of clouds and precipitation.* Atmospheric and oceanographic sciences library, Kluwer Academic Publishers.

Puri, K., G. S. Dietachmayer, G. A. Mills, N. E. Davidson, R. A. Bowen, and L. W. Logan, 1998: The new BMRC Limited Area Prediction System, LAPS. *Australian Meteorological Magazine*, **47**, 203–223.

Qi, L., L. M. Leslie, and S. X. Zhao, 1999: Cut-off low pressure systems over southern Australia: climatology and case study. *International Journal of Climatology*, **19**, 1633–1649.

Rauber, R. M. and L. O. Grant, 1987: Supercooled Liquid Water Structure of a Shallow Orographic Cloud System in Southern Utah. *Journal of Applied Meteorology*, **26**, 208–215.

Rolph, G. and R. Draxler, 1990: Sensitivity of Three-Dimensional Trajectories to the Spatial and Temporal Densities of the Wind Field. *Journal of Applied Meteorology*, **29 (10)**, 1043–1054.

Rosenfeld, D., 2000: Suppression of rain and snow by urban and industrial air pollution. *Science*, **287**, 1793–1796.

Rosenfeld, D. and G. Gutman, 1994: Retrieving microphysical properties near the tops of potential rain clouds by multispectral analysis of AVHRR data. *Atmospheric Research*, **34 (1-4)**, 259–283, 11th conference on clouds and precipitation.

Rosenfeld, D., I. Lensky, J. Peterson, and A. Gingis, 2006: Potential impacts of air pollution aerosols on precipitation in Australia. *Clean Air and Environmental Quality*, **40**, 43–49.

Rosenfeld, D., J. Peterson, and A. Gingis, 2009: Comment on "Air pollution and precipitation suppression over SE Australia: a critical review of evidence presented by Rosenfeld (2000) and Rosenfeld (2006)" by Greg Ayers. *Tellus B*, **61 (4)**, 694–700.

Rotunno, R. and R. Houze, 2007: Lessons on orographic precipitation from the Mesoscale Alpine Programme. *Quaterly Journal of the Royal Meteorological Society*, **133**, 811–830.

Ryan, B. F. and W. D. King, 1997: A Critical Review of the Australian Experience in Cloud Seeding. *Bulletin of the American Meteorological Society*, **78**, 239–239.

Ryan, B. F. and K. J. Wilson, 1985: The Australian Summertime Cool Change. Part III: Subsynoptic and Mesoscale Model. *Monthly Weather Review*, **113 (2)**, 224–240.

Sardeshmukh, P. D. and B. Liebmann, 1993: An assessment of low-frequency variability in the tropics as indicated by some proxies of tropical convection. *Journal of Climate*, **6**, 569–575.

Schaefer, V. J., 1946: The Production of Ice Crystals in a Cloud of Supercooled Water Droplets. *Science*, **104**, 457–459.

Simmonds, A. S., D. D. Uppala, and S. Kobayashi, 2007: ERA-Interim: New ECMWF reanalysis products from 1989 onwards. *ECMWF Newsletter*, **110**, 25–35.

Simmonds, I. and K. Keay, 2000: Mean Southern Hemisphere Extratropical Cyclone Behaviour in the 40-Year NCEP–NCAR Reanalysis. *Journal of Climate*, **13**, 873–885.

Smith, E. J., E. E. Adderley, and D. T. Walsh, 1963: A Cloud-Seeding Experiment in the Snowy Mountains, Australia. *Journal of Applied Meteorology*, **2**, 324–332.

Stoelinga, M., et al., 2003: Improvement of Microphysical Parameterizations through Observational Verification Experiments (IMPROVE). *Bulletin of the American Meteorological Society*, **84**, 1807–1826.

Stohl, A., 1998: Computation, accuracy and applications of trajectories – A review and bibliography. *Atmospheric Environment*, **32 (6)**, 947–966.

Stohl, A. and P. Seibert, 1998: Accuracy of trajectories as determined from the conservation of meteorological tracers. *Quarterly Journal of the Royal Meteorological Society*, **124**, 1465–1484.

Stunder, B. J. B., 1996: An assessment of the quality of forecast trajectories. *Journal of Applied Meteorology*, **35 (8)**, 1319–1331.

Thompson, G., P. R. Field, R. M. Rasmussen, and W. D. Hall, 2008: Explicit Forecasts of Winter Precipitation Using an Improved Bulk Microphysics Scheme. Part II: Implementation of a New Snow Parameterization. *Monthly Weather Review*, **136**, 5095–+.

Thompson, G., R. M. Rasmussen, and K. Manning, 2004: Explicit Forecasts of Winter Precipitation Using an Improved Bulk Microphysics Scheme. Part I: Description and Sensitivity Analysis. *Monthly Weather Review*, **132 (2)**, 519–542.

Timbal, B., 2009: The continuing decline in SEA rainfall: update to May 2009. *CAWCR Research Letters*, **2**, 4–11.

Trenberth, K. E., 1991: Storm tracks in the southern hemisphere. *Journal of the Atmospheric Sciences*, **48 (19)**, 2159–2178.

Twomey, S., 1977: *Atmospheric aerosols*. Developments in atmospheric science, Elsevier Scientific Pub. Co.

Twomey, S. and T. A. Wojciechowski, 1969: Observations of the geographical variation of cloud nuclei. *Journal of the Atmospheric Sciences*, **26 (4)**, 648–651.

Viney, N. and B. Bates, 2004: It never rains on Sunday: the prevalence and implications of untagged multi-day rainfall accumulations in the Australian high quality data set. *International Journal of Climatology*, **24**, 1171–1192.

Volkert, H. and T. Gutermann, 2007: Inter-domain cooperation for mesoscale atmospheric laboratories: The Mesoscale Alpine Programme as a rich study case. *Quaterly Journal of the Royal Meteorological Society*, **133**, 949–967.

Vonnegut, B., 1947: The Nucleation of Ice Formation by Silver Iodide. *Journal of Applied Physics*, **18**, 593–595.

Walmsley, J. L. and J. Mailhot, 1983: On the numerical accuracy of trajectory models for long-range transport of atmospheric pollutants. *Atmosphere-Ocean*, **21**, 14–39.

Warburton, J. A. and M. A. Wetzel, 1992: Field study of the potential for winter precipitation enhancement in the australian snowy mountains. *Atmospheric Research*, **28 (3-4)**, 327 – 363.

Warner, J., 1968: A reduction in rainfall associated with smoke from sugar-cane fires—an inadvertent weather modification? *Journal of Applied Meteorology*, **7 (2)**, 247–251.

Westwater, E., 1978: The accuracy of water vapor and cloud liquid determination by dual-frequency ground-based microwave radiometry. *Radio Science*, **13**, 688–685.

Wratt, D., 1996: The New Zealand Southern Alps Experiment. *Bulletin of the American Meteorological Society*, **77**, 683–692.

Wright, W., 1989: A synoptic climatological classification of winter precipitation in Victoria. *Australian Meteorological Magazine*, **37 (4)**, 217–229.

Young, K. C., 1974: A numerical simulation of wintertime, orographic precipitation: Part i. description of model microphysics and numerical techniques. *Journal of the Atmospheric Sciences*, **31 (7)**, 1735–1748.

Zhu, Y. and R. E. Newell, 1994: Atmosperic rivers and bombs. *Geophysical Research Letters*, **21 (18)**.

Appendix

A.1 South-eastern Australian precipitation

Some aspects of the analysis of Murphy and Timbal (2008) investigating the nature of precipitation decline in south-eastern Australia have been repeated and extended to include up to the year 2009, in order to make more relevant comparisons with the decline in Snowy Mountains precipitation.

Murphy and Timbal (2008) used the high quality rainfall records (Lavery et al., 1997) for Australia, which are publicly available from the National Climate Centre. Using mainland gauge south of 33° S and east of 135° E, they compared both the annual and monthly precipitation amounts during 1961–1990 (The WMO recommended reference period) and 1997–2006. After the publication of the work, south-eastern Australia experienced several years of further drought, the nature of which has been investigated in this thesis.

To extend the investigation, we used the all of the BOM “high quality” gauges from the same region and produced figures comparable to those presented by Murphy and Timbal (2008).

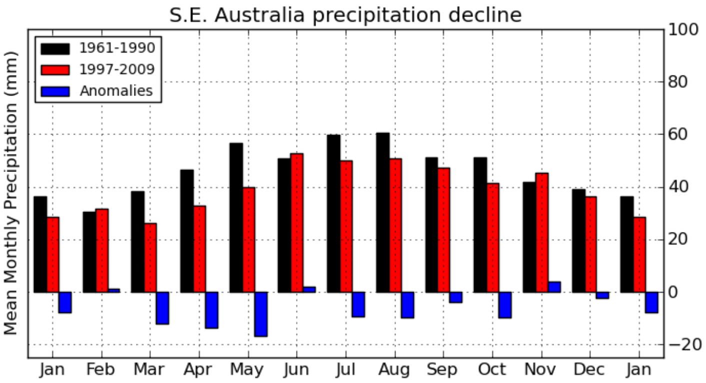

Figure A.1: Average monthly precipitation amounts for south-eastern Australia for the periods 1961–1990 and 1997–2009, with differences shown by the blue bars. This figure is an update to Murphy and Timbal (2008, Fig. 4) to include until the end of the year 2009.

A.2 Table of precipitation events

Table A.1: Record of all wintertime precipitation events classified for the synoptic decomposition performed in chapter 3

Start Date	**End Date**	**R. Days**	**Precip.**	**Classification**	**Comments**
04/05/1990	08/05/1990	1	2.32	E. Low with front	
09/05/1990	14/05/1990	2	10.75	C.O. Low with front	
15/05/1990	19/05/1990	2	41.34	C.O. Low with front	
23/05/1990	27/05/1990	3	32.33	C.O. Low	
28/05/1990	02/06/1990	3	33.49	Other	
03/06/1990	05/06/1990	1	21.41	E. Low with front	
13/06/1990	19/06/1990	1	25.00	E. Low with front	
20/06/1990	23/06/1990	1	1.49	E. Low	
24/06/1990	27/06/1990	3	9.50	C.O. Low	
27/06/1990	29/06/1990	3	76.40	C.O. Low with front	
30/06/1990	04/07/1990	5	125.94	C.O. Low with front	
05/07/1990	10/07/1990	4	107.50	E. Low with front	
11/07/1990	15/07/1990	2	8.81	E. Low	
16/07/1990	21/07/1990	4	44.29	E. Low with front	
22/07/1990	24/07/1990	2	22.41	E. Low with front	
25/07/1990	28/07/1990	3	45.25	E. Low with front	
29/07/1990	04/08/1990	4	39.84	C.O. Low	Looks like an E.C.L.
05/08/1990	08/08/1990	3	78.89	C.O. Low with front	
09/08/1990	11/08/1990	3	43.03	C.O. Low with front	
12/08/1990	14/08/1990	3	52.54	C.O. Low	
15/08/1990	16/08/1990	2	33.70	C.O. Low with front	
17/08/1990	19/08/1990	2	16.49	E. Low	
20/08/1990	21/08/1990	2	33.64	C.O. Low with front	
22/08/1990	25/08/1990	4	38.10	C.O. Low with front	
26/08/1990	29/08/1990	1	10.33	C.O. Low	
30/08/1990	31/08/1990	1	16.03	E. Low with front	
01/09/1990	02/09/1990	1	1.67	E. Low	
03/09/1990	06/09/1990	2	47.81	E. Low with front	
13/09/1990	15/09/1990	2	33.12	C.O. Low	
16/09/1990	20/09/1990	0	1.04	Other	
21/09/1990	23/09/1990	1	38.54	E. Low with front	
24/09/1990	28/09/1990	2	15.21	E. Low with front	
09/05/1991	10/05/1991	1	5.23	E. Low with front	
11/05/1991	17/05/1991	1	2.61	Other	
18/05/1991	24/05/1991	1	9.58	C.O. Low	Weak
25/05/1991	06/06/1991	2	33.57	E. Low with front	Near miss for cut-off low
07/06/1991	11/06/1991	5	86.06	C.O. Low	Upper level dominant
12/06/1991	13/06/1991	2	86.65	C.O. Low	
16/06/1991	17/06/1991	2	30.60	C.O. Low	
24/06/1991	25/06/1991	2	70.72	E. Low with front	
26/06/1991	27/06/1991	1	10.26	E. Low with front	
28/06/1991	02/07/1991	2	59.28	E. Low with front	
03/07/1991	08/07/1991	3	25.20	C.O. Low with front	
09/07/1991	13/07/1991	4	78.20	C.O. Low	EC low develops after ano
14/07/1991	16/07/1991	2	14.12	C.O. Low with front	
17/07/1991	20/07/1991	2	5.84	E. Low	
21/07/1991	22/07/1991	1	4.01	Other	Diffluent Jet
23/07/1991	27/07/1991	3	15.87	E. Low with front	
28/07/1991	31/07/1991	4	38.36	E. Low with front	
01/08/1991	04/08/1991	2	19.47	Other	
05/08/1991	07/08/1991	3	100.54	C.O. Low with front	
08/08/1991	12/08/1991	3	95.29	E. Low with front	

Continued on next page

Table A.1 – continued from previous page

Start Date	End Date	R. Days	Precip.	Classification	Comments
13/08/1991	15/08/1991	3	38.50	E. Low	
16/08/1991	19/08/1991	2	37.32	E. Low with front	
20/08/1991	29/08/1991	2	43.84	E. Low with front	
30/08/1991	02/09/1991	3	60.04	C.O. Low with front	
03/09/1991	04/09/1991	1	1.25	E. Low	
05/09/1991	10/09/1991	2	6.04	E. Low with front	
11/09/1991	13/09/1991	2	65.31	C.O. Low	
14/09/1991	17/09/1991	3	33.65	C.O. Low with front	
18/09/1991	20/09/1991	3	99.58	C.O. Low with front	
21/09/1991	23/09/1991	2	58.33	C.O. Low with front	
24/09/1991	30/09/1991	1	16.88	E. Low with front	
03/05/1992	04/05/1992	1	3.07	Other	Diffluent Jet
08/05/1992	11/05/1992	1	7.45	E. Low	
12/05/1992	15/05/1992	2	23.00	C.O. Low with front	
18/05/1992	21/05/1992	1	2.23	C.O. Low	
22/05/1992	23/05/1992	1	4.28	C.O. Low	
24/05/1992	29/05/1992	2	39.76	E. Low with front	
01/06/1992	05/06/1992	2	66.12	C.O. Low with front	
06/06/1992	09/06/1992	2	2.56	E. Low	
10/06/1992	11/06/1992	2	32.14	E. Low with front	
12/06/1992	14/06/1992	1	17.67	E. Low	
15/06/1992	22/06/1992	3	23.35	C.O. Low	
23/06/1992	26/06/1992	4	13.00	C.O. Low	
27/06/1992	29/06/1992	1	5.77	Other	ECL
30/06/1992	03/07/1992	0	1.84	Other	
04/07/1992	06/07/1992	2	17.40	E. Low with front	
07/07/1992	09/07/1992	1	5.68	C.O. Low with front	
10/07/1992	11/07/1992	1	1.22	E. Low	
12/07/1992	15/07/1992	1	5.51	E. Low with front	
18/07/1992	22/07/1992	2	20.98	E. Low with front	
23/07/1992	27/07/1992	2	19.06	E. Low with front	
28/07/1992	30/07/1992	1	5.68	C.O. Low with front	
31/07/1992	02/08/1992	1	2.55	C.O. Low with front	
03/08/1992	05/08/1992	1	1.58	Other	
06/08/1992	08/08/1992	2	76.14	C.O. Low with front	
11/08/1992	12/08/1992	2	39.74	E. Low with front	
13/08/1992	14/08/1992	2	81.92	C.O. Low with front	
15/08/1992	17/08/1992	2	19.10	E. Low with front	
18/08/1992	19/08/1992	2	26.37	C.O. Low with front	
20/08/1992	22/08/1992	1	22.93	E. Low with front	
23/08/1992	26/08/1992	1	9.19	C.O. Low with front	
27/08/1992	29/08/1992	1	6.59	E. Low	
30/08/1992	02/09/1992	4	147.07	C.O. Low with front	
03/09/1992	05/09/1992	3	25.40	C.O. Low with front	
06/09/1992	07/09/1992	2	6.60	E. Low	
08/09/1992	09/09/1992	1	15.45	E. Low	
10/09/1992	14/09/1992	3	64.11	C.O. Low with front	
15/09/1992	18/09/1992	3	58.28	C.O. Low with front	
19/09/1992	21/09/1992	1	7.22	E. Low	
22/09/1992	24/09/1992	2	27.20	C.O. Low with front	
25/09/1992	28/09/1992	2	39.78	C.O. Low	
29/09/1992	03/10/1992	3	36.86	E. Low with front	
02/05/1993	05/05/1993	2	15.27	E. Low	
10/05/1993	12/05/1993	2	11.55	E. Low	
13/05/1993	16/05/1993	1	1.30	E. Low	
22/05/1993	25/05/1993	2	8.01	C.O. Low with front	
29/05/1993	01/06/1993	1	39.75	E. Low with front	
02/06/1993	04/06/1993	2	13.19	E. Low	ECL

Continued on next page

Table A.1 – continued from previous page

Start Date	End Date	R. Days	Precip.	Classification	Comments
10/06/1993	14/06/1993	4	74.91	C.O. Low with front	
15/06/1993	17/06/1993	2	4.85	Other	Upper Diffluence
18/06/1993	20/06/1993	3	32.20	E. Low with front	
21/06/1993	22/06/1993	3	25.40	E. Low with front	
23/06/1993	25/06/1993	1	6.68	E. Low	
26/06/1993	05/07/1993	3	55.07	E. Low with front	
06/07/1993	09/07/1993	3	48.78	C.O. Low with front	
10/07/1993	11/07/1993	1	17.57	E. Low with front	
12/07/1993	18/07/1993	1	2.53	C.O. Low	
23/07/1993	28/07/1993	2	68.27	C.O. Low with front	
29/07/1993	01/08/1993	2	67.66	E. Low with front	
02/08/1993	05/08/1993	3	13.56	C.O. Low with front	
06/08/1993	10/08/1993	3	28.88	E. Low with front	
11/08/1993	13/08/1993	1	22.93	C.O. Low with front	
14/08/1993	20/08/1993	4	70.94	C.O. Low with front	
21/08/1993	24/08/1993	1	4.27	E. Low	
27/08/1993	05/09/1993	4	109.81	C.O. Low with front	
06/09/1993	11/09/1993	2	50.79	E. Low with front	
12/09/1993	19/09/1993	5	21.28	C.O. Low	Upper anomaly... almost n
20/09/1993	24/09/1993	3	43.29	C.O. Low with front	
08/05/1994	14/05/1994	1	13.59	C.O. Low	
17/05/1994	21/05/1994	3	57.08	E. Low with front	
22/05/1994	25/05/1994	2	5.49	E. Low with front	
26/05/1994	31/05/1994	3	45.16	C.O. Low with front	
04/06/1994	11/06/1994	3	25.73	C.O. Low	
12/06/1994	16/06/1994	3	17.03	E. Low with front	
17/06/1994	23/06/1994	4	71.15	C.O. Low with front	
24/06/1994	30/06/1994	4	93.68	C.O. Low with front	
04/07/1994	15/07/1994	3	24.65	E. Low with front	
16/07/1994	18/07/1994	0	1.31	E. Low	
28/07/1994	30/07/1994	2	6.21	Other	Upper divergence
31/07/1994	04/08/1994	3	51.19	C.O. Low with front	
05/08/1994	10/08/1994	2	10.86	E. Low with front	
13/08/1994	17/08/1994	2	35.38	E. Low with front	
20/08/1994	25/08/1994	2	17.92	E. Low with front	
05/09/1994	08/09/1994	2	16.00	E. Low	
11/09/1994	15/09/1994	1	5.74	C.O. Low with front	
16/09/1994	18/09/1994	0	1.20	E. Low	
19/09/1994	20/09/1994	2	11.10	E. Low with front	
21/09/1994	23/09/1994	1	14.15	E. Low	
24/09/1994	26/09/1994	1	1.76	E. Low	
27/09/1994	29/09/1994	3	40.89	E. Low with front	
30/04/1995	02/05/1995	2	55.70	E. Low with front	
03/05/1995	07/05/1995	3	36.60	C.O. Low with front	
10/05/1995	12/05/1995	3	22.00	E. Low with front	
13/05/1995	16/05/1995	3	127.10	E. Low with front	
17/05/1995	20/05/1995	1	5.20	C.O. Low with front	
25/05/1995	29/05/1995	4	100.50	C.O. Low with front	
04/06/1995	08/06/1995	1	7.50	Other	Upper diffluence
09/06/1995	14/06/1995	4	202.10	C.O. Low with front	
15/06/1995	20/06/1995	1	3.20	E. Low	
25/06/1995	28/06/1995	2	18.50	C.O. Low with front	
29/06/1995	30/06/1995	2	26.80	C.O. Low	
01/07/1995	03/07/1995	3	64.50	C.O. Low with front	
04/07/1995	05/07/1995	1	11.60	E. Low	
08/07/1995	13/07/1995	3	62.90	C.O. Low with front	
14/07/1995	16/07/1995	3	66.80	C.O. Low with front	
17/07/1995	21/07/1995	4	108.50	C.O. Low with front	

Continued on next page

Table A.1 – continued from previous page

Start Date	End Date	R. Days	Precip.	Classification	Comments
22/07/1995	26/07/1995	4	33.90	C.O. Low with front	
27/07/1995	28/07/1995	2	6.70	C.O. Low with front	
29/07/1995	01/08/1995	4	24.70	E. Low with front	
02/08/1995	05/08/1995	3	28.20	E. Low with front	
06/08/1995	09/08/1995	3	13.80	C.O. Low	Near miss
16/08/1995	23/08/1995	1	10.50	E. Low	
24/08/1995	27/08/1995	1	1.70	E. Low	
28/08/1995	03/09/1995	2	123.80	E. Low with front	
04/09/1995	06/09/1995	1	28.70	E. Low with front	
07/09/1995	08/09/1995	1	1.60	Other	
09/09/1995	10/09/1995	1	1.10	Other	
11/09/1995	16/09/1995	1	3.60	E. Low with front	
17/09/1995	23/09/1995	3	53.80	E. Low with front	
24/09/1995	26/09/1995	2	28.10	C.O. Low	
04/05/1996	08/05/1996	3	44.00	C.O. Low	Upper level anomaly over
09/05/1996	15/05/1996	2	62.60	E. Low with front	
22/05/1996	26/05/1996	1	3.60	E. Low	
31/05/1996	03/06/1996	1	20.70	E. Low with front	
04/06/1996	06/06/1996	2	52.00	E. Low with front	
07/06/1996	09/06/1996	1	3.00	E. Low	
13/06/1996	21/06/1996	1	7.20	C.O. Low	
22/06/1996	25/06/1996	3	66.60	C.O. Low with front	
26/06/1996	28/06/1996	3	31.00	C.O. Low with front	
29/06/1996	01/07/1996	3	40.50	C.O. Low with front	
02/07/1996	04/07/1996	1	13.30	C.O. Low with front	
05/07/1996	09/07/1996	3	50.40	C.O. Low with front	
10/07/1996	13/07/1996	1	1.10	C.O. Low	
14/07/1996	16/07/1996	1	1.20	Other	
17/07/1996	23/07/1996	5	85.40	E. Low with front	
24/07/1996	26/07/1996	3	32.60	C.O. Low with front	
27/07/1996	28/07/1996	2	21.80	Other	Continental low
29/07/1996	31/07/1996	2	14.30	Other	ECL (from existing low)
01/08/1996	02/08/1996	2	60.30	E. Low with front	
03/08/1996	03/08/1996	1	39.80	E. Low with front	
04/08/1996	06/08/1996	2	84.40	E. Low with front	
07/08/1996	11/08/1996	3	58.70	E. Low with front	
15/08/1996	17/08/1996	2	17.20	E. Low with front	
18/08/1996	20/08/1996	1	7.20	E. Low with front	
23/08/1996	26/08/1996	2	7.80	E. Low	
27/08/1996	30/08/1996	3	24.90	C.O. Low	
31/08/1996	02/09/1996	2	4.20	Other	ECL
03/09/1996	05/09/1996	3	14.00	E. Low	
06/09/1996	07/09/1996	2	21.80	E. Low with front	
08/09/1996	09/09/1996	2	6.50	C.O. Low with front	
10/09/1996	11/09/1996	2	27.20	C.O. Low with front	
12/09/1996	18/09/1996	5	144.20	C.O. Low with front	
19/09/1996	23/09/1996	2	32.30	E. Low with front	
24/09/1996	26/09/1996	1	6.30	E. Low with front	
27/09/1996	28/09/1996	1	27.60	E. Low with front	
01/05/1997	06/05/1997	1	15.00	E. Low with front	
07/05/1997	09/05/1997	1	41.50	C.O. Low with front	
10/05/1997	12/05/1997	0	1.20	Other	ECL present
13/05/1997	20/05/1997	3	26.20	C.O. Low	Continental
21/05/1997	25/05/1997	1	2.40	Other	
26/05/1997	28/05/1997	1	25.40	E. Low with front	
29/05/1997	31/05/1997	2	29.50	E. Low with front	
05/06/1997	08/06/1997	2	33.50	E. Low with front	
12/06/1997	17/06/1997	3	56.50	C.O. Low with front	

Continued on next page

Table A.1 – continued from previous page

Start Date	End Date	R. Days	Precip.	Classification	Comments
18/06/1997	27/06/1997	2	13.00	Other	ECL present
28/06/1997	01/07/1997	2	82.60	Other	ECL present
05/07/1997	15/07/1997	4	51.20	E. Low with front	
16/07/1997	19/07/1997	2	13.90	E. Low with front	
25/07/1997	28/07/1997	3	71.50	C.O. Low with front	
29/07/1997	31/07/1997	1	2.30	E. Low	
05/08/1997	11/08/1997	5	51.40	C.O. Low with front	
12/08/1997	16/08/1997	4	48.30	E. Low with front	
17/08/1997	19/08/1997	2	11.30	E. Low with front	
22/08/1997	26/08/1997	3	42.70	C.O. Low with front	
27/08/1997	28/08/1997	1	5.50	E. Low	
29/08/1997	01/09/1997	2	17.30	C.O. Low	
03/09/1997	02/09/1997	2	73.60	C.O. Low with front	
04/09/1997	06/09/1997	2	16.70	C.O. Low with front	
07/09/1997	11/09/1997	3	55.00	C.O. Low with front	
12/09/1997	17/09/1997	1	26.50	C.O. Low	
20/09/1997	23/09/1997	2	23.60	C.O. Low	
24/09/1997	26/09/1997	2	2.60	Other	ECL present
27/09/1997	29/09/1997	2	4.20	E. Low	
02/05/1998	05/05/1998	1	3.10	Other	
06/05/1998	07/05/1998	1	1.50	Other	ECL present
08/05/1998	10/05/1998	1	3.30	C.O. Low with front	
15/05/1998	17/05/1998	2	3.10	Other	
20/05/1998	23/05/1998	2	11.90	C.O. Low with front	
24/05/1998	26/05/1998	2	25.00	C.O. Low with front	
29/05/1998	06/06/1998	1	1.80	E. Low	
07/06/1998	09/06/1998	2	46.20	C.O. Low with front	
10/06/1998	14/06/1998	1	12.10	E. Low with front	
15/06/1998	18/06/1998	2	8.50	E. Low	
19/06/1998	22/06/1998	2	98.00	C.O. Low with front	
23/06/1998	27/06/1998	4	52.30	Other	ECL present
28/06/1998	30/06/1998	1	1.10	E. Low	
01/07/1998	08/07/1998	2	74.70	E. Low with front	
09/07/1998	12/07/1998	2	35.10	C.O. Low with front	
13/07/1998	20/07/1998	0	1.20	Other	
21/07/1998	25/07/1998	3	29.50	C.O. Low with front	
26/07/1998	31/07/1998	5	90.20	C.O. Low with front	
01/08/1998	02/08/1998	2	10.50	E. Low with front	
03/08/1998	04/08/1998	2	6.60	E. Low	
05/08/1998	06/08/1998	1	12.40	C.O. Low	
07/08/1998	10/08/1998	2	18.90	Other	ECL present
11/08/1998	13/08/1998	3	23.40	C.O. Low	
14/08/1998	15/08/1998	1	19.50	Other	
16/08/1998	21/08/1998	3	43.40	Other	Easterlies
22/08/1998	25/08/1998	3	60.30	E. Low with front	
29/08/1998	08/09/1998	3	35.50	E. Low with front	
09/09/1998	15/09/1998	4	35.00	C.O. Low with front	
16/09/1998	19/09/1998	3	20.70	E. Low	
20/09/1998	21/09/1998	1	29.20	C.O. Low with front	
22/09/1998	27/09/1998	4	86.20	E. Low with front	
06/05/1999	09/05/1999	1	2.80	E. Low	
12/05/1999	15/05/1999	3	39.30	E. Low with front	
16/05/1999	19/05/1999	1	24.40	C.O. Low with front	
20/05/1999	28/05/1999	3	18.20	C.O. Low with front	
29/05/1999	02/06/1999	3	113.10	C.O. Low with front	
03/06/1999	09/06/1999	2	30.00	E. Low with front	
10/06/1999	13/06/1999	3	18.90	E. Low	ECL forms
14/06/1999	17/06/1999	4	52.40	C.O. Low with front	

Continued on next page

Table A.1 – continued from previous page

Start Date	End Date	R. Days	Precip.	Classification	Comments
18/06/1999	21/06/1999	2	63.10	C.O. Low with front	
28/06/1999	03/07/1999	1	13.80	C.O. Low	
04/07/1999	16/07/1999	3	13.80	Other	ECL Present
17/07/1999	21/07/1999	4	56.70	E. Low with front	
22/07/1999	24/07/1999	2	15.80	E. Low	
27/07/1999	02/08/1999	1	16.70	E. Low with front	
03/08/1999	12/08/1999	3	76.80	C.O. Low with front	
13/08/1999	17/08/1999	3	49.40	E. Low with front	
18/08/1999	22/08/1999	1	10.10	E. Low with front	
23/08/1999	30/08/1999	4	37.00	C.O. Low	Continental
31/08/1999	04/09/1999	2	7.70	E. Low	
05/09/1999	09/09/1999	3	83.70	C.O. Low with front	
10/09/1999	20/09/1999	4	42.10	C.O. Low with front	
30/04/2000	03/05/2000	1	9.70	E. Low with front	
04/05/2000	05/05/2000	2	32.60	Other	Strong eastern trough
06/05/2000	07/05/2000	1	17.30	C.O. Low with front	
13/05/2000	16/05/2000	3	73.30	C.O. Low with front	
23/05/2000	26/05/2000	1	6.90	E. Low	
27/05/2000	29/05/2000	3	56.30	C.O. Low with front	
30/05/2000	03/06/2000	4	22.90	C.O. Low with front	
04/06/2000	08/06/2000	3	17.40	C.O. Low with front	
09/06/2000	11/06/2000	2	3.70	E. Low	
19/06/2000	21/06/2000	2	41.00	C.O. Low with front	
23/06/2000	25/06/2000	1	26.40	C.O. Low with front	
26/06/2000	01/07/2000	3	28.20	C.O. Low with front	
07/07/2000	09/07/2000	3	20.10	C.O. Low with front	
10/07/2000	12/07/2000	1	7.20	C.O. Low	
13/07/2000	18/07/2000	2	3.30	E. Low	
19/07/2000	20/07/2000	2	38.00	E. Low with front	
21/07/2000	23/07/2000	3	32.90	E. Low with front	
24/07/2000	29/07/2000	5	64.90	C.O. Low with front	
05/08/2000	13/08/2000	5	87.80	E. Low with front	
14/08/2000	18/08/2000	4	58.20	E. Low with front	
19/08/2000	21/08/2000	1	3.50	Other	
22/08/2000	25/08/2000	4	17.00	C.O. Low with front	
26/08/2000	28/08/2000	3	26.60	C.O. Low with front	
29/08/2000	31/08/2000	3	27.50	Other	Strong eastern trough
01/09/2000	02/09/2000	2	19.70	E. Low with front	
03/09/2000	04/09/2000	1	16.40	E. Low with front	
05/09/2000	07/09/2000	2	20.50	E. Low with front	
08/09/2000	09/09/2000	2	104.20	C.O. Low	
10/09/2000	11/09/2000	2	22.70	C.O. Low with front	
12/09/2000	14/09/2000	2	26.70	E. Low with front	
15/09/2000	22/09/2000	1	1.10	E. Low	
26/09/2000	27/09/2000	1	7.60	C.O. Low	
26/09/2000	26/09/2000	1	34.40	C.O. Low	
27/09/2000	27/09/2000	1	24.00	C.O. Low	
28/09/2000	28/09/2000	1	14.90	C.O. Low	
05/05/2001	06/05/2001	1	4.00	Other	Upper div
09/05/2001	19/05/2001	2	28.90	C.O. Low with front	
26/05/2001	30/05/2001	2	16.20	C.O. Low	
31/05/2001	09/06/2001	2	38.40	C.O. Low with front	
10/06/2001	11/06/2001	1	15.40	C.O. Low	
12/06/2001	18/06/2001	4	128.80	C.O. Low with front	
19/06/2001	23/06/2001	2	25.40	C.O. Low with front	
03/07/2001	09/07/2001	4	78.40	C.O. Low with front	
10/07/2001	11/07/2001	1	6.90	Other	
12/07/2001	14/07/2001	3	12.40	Other	Upper Div

Continued on next page

Table A.1 – continued from previous page

Start Date	End Date	R. Days	Precip.	Classification	Comments
15/07/2001	16/07/2001	2	7.00	C.O. Low with front	
17/07/2001	17/07/2001	1	6.30	E. Low	
18/07/2001	20/07/2001	1	8.70	E. Low	
21/07/2001	28/07/2001	1	3.90	C.O. Low	Upper Anomaly
29/07/2001	03/08/2001	2	24.00	E. Low with front	
04/08/2001	07/08/2001	3	44.30	C.O. Low with front	
08/08/2001	11/08/2001	3	30.10	C.O. Low with front	
12/08/2001	15/08/2001	1	1.70	E. Low	
16/08/2001	17/08/2001	1	30.50	E. Low with front	
18/08/2001	19/08/2001	2	44.30	E. Low with front	
20/08/2001	22/08/2001	3	80.80	E. Low with front	
23/08/2001	25/08/2001	1	21.60	C.O. Low with front	
26/08/2001	31/08/2001	2	31.70	C.O. Low with front	
01/09/2001	04/09/2001	3	18.90	C.O. Low with front	
05/09/2001	06/09/2001	1	13.30	E. Low	
07/09/2001	11/09/2001	3	68.90	C.O. Low with front	
12/09/2001	13/09/2001	0	1.40	C.O. Low	
14/09/2001	16/09/2001	1	2.50	Other	
17/09/2001	23/09/2001	1	8.00	E. Low	
24/09/2001	27/09/2001	2	21.50	E. Low with front	
30/04/2002	11/05/2002	1	6.90	E. Low	
12/05/2002	18/05/2002	3	37.00	C.O. Low with front	
19/05/2002	23/05/2002	4	75.00	C.O. Low with front	
26/05/2002	09/06/2002	3	84.80	E. Low with front	
10/06/2002	12/06/2002	3	20.00	E. Low	
13/06/2002	14/06/2002	2	52.50	C.O. Low with front	
15/06/2002	20/06/2002	3	69.10	C.O. Low with front	
21/06/2002	24/06/2002	3	12.40	E. Low	
25/06/2002	27/06/2002	1	3.00	E. Low	
28/06/2002	30/06/2002	2	34.00	E. Low with front	
01/07/2002	05/07/2002	2	54.40	E. Low with front	
07/07/2002	09/07/2002	3	72.00	C.O. Low with front	
10/07/2002	11/07/2002	1	10.30	C.O. Low with front	
12/07/2002	20/07/2002	2	10.80	E. Low with front	
21/07/2002	22/07/2002	1	13.90	E. Low with front	
23/07/2002	25/07/2002	1	8.40	E. Low	
26/07/2002	28/07/2002	1	1.50	Other	
29/07/2002	30/07/2002	1	1.60	E. Low with front	
31/07/2002	05/08/2002	3	42.40	C.O. Low with front	
06/08/2002	09/08/2002	2	15.70	E. Low with front	
12/08/2002	14/08/2002	3	67.20	C.O. Low with front	
15/08/2002	18/08/2002	1	7.40	Other	
21/08/2002	31/08/2002	2	12.00	C.O. Low with front	
01/09/2002	02/09/2002	1	1.90	C.O. Low with front	
03/09/2002	04/09/2002	1	39.70	E. Low with front	
05/09/2002	07/09/2002	2	8.50	E. Low	
08/09/2002	11/09/2002	3	18.60	E. Low	
12/09/2002	18/09/2002	2	71.10	E. Low with front	
19/09/2002	21/09/2002	2	55.80	E. Low with front	
22/09/2002	24/09/2002	1	6.20	E. Low	
25/09/2002	26/09/2002	1	1.20	E. Low with front	
27/09/2002	01/10/2002	2	27.60	C.O. Low with front	
02/05/2003	11/05/2003	2	14.90	E. Low	
12/05/2003	18/05/2003	1	6.00	Other	
19/05/2003	23/05/2003	3	61.60	C.O. Low with front	
27/05/2003	04/06/2003	2	15.20	E. Low	
05/06/2003	07/06/2003	3	48.80	E. Low with front	
08/06/2003	11/06/2003	2	15.20	E. Low with front	

Continued on next page

Table A.1 – continued from previous page

Start Date	End Date	R. Days	Precip.	Classification	Comments
12/06/2003	14/06/2003	2	41.80	E. Low with front	
15/06/2003	15/06/2003	1	19.10	E. Low with front	
16/06/2003	17/06/2003	2	9.00	E. Low	
18/06/2003	19/06/2003	1	3.90	E. Low	
20/06/2003	25/06/2003	3	11.00	C.O. Low with front	
26/06/2003	28/06/2003	1	25.50	E. Low	
30/06/2003	03/07/2003	3	26.70	C.O. Low	
08/07/2003	10/07/2003	0	1.20	Other	
11/07/2003	15/07/2003	2	52.80	E. Low with front	
16/07/2003	23/07/2003	2	10.20	C.O. Low	
24/07/2003	25/07/2003	2	50.40	C.O. Low with front	
26/07/2003	28/07/2003	2	19.30	C.O. Low with front	
29/07/2003	03/08/2003	4	24.30	E. Low with front	
04/08/2003	08/08/2003	3	20.30	E. Low with front	
09/08/2003	11/08/2003	3	10.90	C.O. Low with front	
12/08/2003	17/08/2003	4	122.70	E. Low with front	
18/08/2003	20/08/2003	1	4.10	E. Low	
21/08/2003	23/08/2003	1	4.10	E. Low	
24/08/2003	29/08/2003	4	128.50	C.O. Low with front	
30/08/2003	03/09/2003	2	17.00	E. Low with front	
04/09/2003	09/09/2003	1	11.30	Other	
10/09/2003	13/09/2003	3	17.20	C.O. Low	
14/09/2003	15/09/2003	2	37.00	E. Low with front	
16/09/2003	18/09/2003	3	62.20	E. Low with front	
19/09/2003	20/09/2003	2	17.50	E. Low with front	
21/09/2003	22/09/2003	1	6.40	E. Low with front	
23/09/2003	25/09/2003	2	29.60	E. Low with front	
26/09/2003	26/09/2003	1	29.00	E. Low	
27/09/2003	30/09/2003	2	21.60	C.O. Low with front	
28/04/2004	02/05/2004	3	24.30	C.O. Low with front	
03/05/2004	03/05/2004	1	6.60	E. Low	
04/05/2004	06/05/2004	2	5.50	E. Low	
10/05/2004	13/05/2004	1	5.00	Other	ECL present
14/05/2004	18/05/2004	1	4.70	C.O. Low	
19/05/2004	20/05/2004	1	26.80	E. Low with front	
23/05/2004	28/05/2004	4	26.10	C.O. Low with front	
29/05/2004	31/05/2004	1	4.50	E. Low	
01/06/2004	06/06/2004	2	19.40	E. Low with front	
07/06/2004	09/06/2004	1	2.70	E. Low	
10/06/2004	12/06/2004	1	27.00	E. Low with front	
13/06/2004	17/06/2004	4	95.50	C.O. Low with front	
18/06/2004	23/06/2004	5	81.20	E. Low with front	
25/06/2004	25/06/2004	2	12.05	C.O. Low with front	
26/06/2004	28/06/2004	3	27.35	C.O. Low with front	
29/06/2004	30/06/2004	2	7.30	E. Low	
26/06/2004	04/07/2004	2	16.10	E. Low with front	
05/07/2004	07/07/2004	3	10.40	E. Low	
08/07/2004	10/07/2004	2	11.80	C.O. Low with front	
11/07/2004	15/07/2004	3	17.70	C.O. Low	
16/07/2004	21/07/2004	2	5.70	E. Low with front	
22/07/2004	27/07/2004	3	54.40	C.O. Low	
28/07/2004	31/07/2004	2	15.00	E. Low	
01/08/2004	05/08/2004	3	51.50	C.O. Low with front	
06/08/2004	08/08/2004	3	24.50	C.O. Low	
09/08/2004	10/08/2004	1	10.50	E. Low	
11/08/2004	13/08/2004	2	9.70	E. Low	
14/08/2004	17/08/2004	3	50.50	C.O. Low with front	
18/08/2004	20/08/2004	0	1.60	C.O. Low	

Continued on next page

Table A.1 – continued from previous page

Start Date	End Date	R. Days	Precip.	Classification	Comments
21/08/2004	24/08/2004	1	11.80	E. Low	
29/08/2004	02/09/2004	3	120.50	C.O. Low with front	
03/09/2004	07/09/2004	2	7.60	Other	
08/09/2004	11/09/2004	4	74.10	C.O. Low with front	
12/09/2004	14/09/2004	3	30.60	E. Low with front	
15/09/2004	17/09/2004	2	6.60	E. Low	
18/09/2004	26/09/2004	1	3.80	E. Low with front	
27/09/2004	01/10/2004	5	36.20	C.O. Low	
01/05/2005	03/05/2005	1	3.30	E. Low	
11/05/2005	12/05/2005	1	3.00	E. Low	
16/05/2005	19/05/2005	0	1.10	Other	
20/05/2005	25/05/2005	1	3.50	Other	
26/05/2005	27/05/2005	1	1.50	E. Low	
28/05/2005	31/05/2005	1	1.90	E. Low	
01/06/2005	13/06/2005	3	39.30	E. Low with front	
14/06/2005	15/06/2005	1	32.50	C.O. Low with front	
16/06/2005	19/06/2005	4	55.30	C.O. Low with front	
20/06/2005	22/06/2005	2	77.90	C.O. Low	
22/06/2005	26/06/2005	3	43.80	C.O. Low with front	
29/06/2005	04/07/2005	4	55.60	C.O. Low with front	
07/07/2005	08/07/2005	1	15.10	E. Low with front	
09/07/2005	12/07/2005	3	39.60	Other	ECL
13/07/2005	15/07/2005	3	20.80	C.O. Low	
16/07/2005	18/07/2005	2	17.70	E. Low with front	
19/07/2005	21/07/2005	1	2.90	E. Low	
22/07/2005	28/07/2005	4	28.20	E. Low with front	
29/07/2005	31/07/2005	1	2.30	C.O. Low with front	
01/08/2005	07/08/2005	3	88.70	E. Low with front	
08/08/2005	11/08/2005	4	53.40	C.O. Low with front	
12/08/2005	15/08/2005	3	9.40	E. Low	
16/08/2005	18/08/2005	2	11.40	E. Low with front	
19/08/2005	21/08/2005	2	8.20	C.O. Low with front	
22/08/2005	24/08/2005	1	25.00	E. Low with front	
25/08/2005	05/09/2005	4	52.10	C.O. Low with front	
06/09/2005	14/09/2005	6	123.70	C.O. Low with front	
15/09/2005	17/09/2005	2	13.70	C.O. Low with front	
18/09/2005	19/09/2005	1	19.60	C.O. Low	
20/09/2005	21/09/2005	1	3.80	C.O. Low with front	
22/09/2005	24/09/2005	1	1.20	C.O. Low	
25/09/2005	28/09/2005	2	13.60	Other	
29/09/2005	01/10/2005	2	66.30	E. Low with front	
01/05/2006	05/05/2006	4	27.00	E. Low with front	
06/05/2006	09/05/2006	3	30.40	C.O. Low with front	
10/05/2006	14/05/2006	2	31.30	E. Low	
22/05/2006	26/05/2006	1	2.00	Other	ECL present
01/06/2006	04/06/2006	3	24.20	C.O. Low	ECL present
05/06/2006	14/06/2006	3	8.30	C.O. Low	ECL present
18/06/2006	26/06/2006	2	13.90	C.O. Low with front	
29/06/2006	05/07/2006	2	14.40	C.O. Low with front	
06/07/2006	09/07/2006	1	6.70	E. Low with front	
10/07/2006	14/07/2006	2	14.50	C.O. Low with front	
15/07/2006	19/07/2006	4	19.90	C.O. Low	Continental
25/07/2006	28/07/2006	2	10.60	Other	ECL present
29/07/2006	03/08/2006	5	28.30	C.O. Low with front	
04/08/2006	05/08/2006	1	4.20	C.O. Low	
08/08/2006	11/08/2006	1	2.50	E. Low with front	
12/08/2006	20/08/2006	2	16.20	E. Low with front	
21/08/2006	24/08/2006	1	3.40	C.O. Low	

Continued on next page

Table A.1 – continued from previous page

Start Date	End Date	R. Days	Precip.	Classification	Comments
25/08/2006	27/08/2006	3	47.30	C.O. Low with front	
03/09/2006	06/09/2006	2	42.30	C.O. Low with front	
07/09/2006	08/09/2006	1	5.00	C.O. Low	
09/09/2006	10/09/2006	2	4.50	C.O. Low	
11/09/2006	13/09/2006	1	2.40	Other	
16/09/2006	21/09/2006	1	7.00	E. Low with front	
22/09/2006	23/09/2006	1	2.60	E. Low with front	
24/09/2006	29/09/2006	1	26.60	E. Low with front	
03/05/2007	06/05/2007	1	18.40	E. Low with front	
07/05/2007	21/05/2007	3	47.20	C.O. Low with front	
22/05/2007	25/05/2007	4	40.60	E. Low with front	
26/05/2007	28/05/2007	1	1.90	E. Low	
29/05/2007	31/05/2007	2	41.80	C.O. Low with front	
01/06/2007	02/06/2007	1	14.60	C.O. Low with front	
03/06/2007	05/06/2007	1	2.20	C.O. Low	
06/06/2007	10/06/2007	1	3.00	Other	ECL
11/06/2007	14/06/2007	2	5.80	E. Low	
15/06/2007	17/06/2007	2	8.10	Other	ECL
18/06/2007	21/06/2007	3	20.20	Other	ECL
22/06/2007	24/06/2007	1	6.80	E. Low	
25/06/2007	30/06/2007	4	50.80	Other	ECL
01/07/2007	02/07/2007	2	24.90	C.O. Low	
03/07/2007	06/07/2007	4	101.00	C.O. Low with front	
07/07/2007	09/07/2007	3	28.40	C.O. Low	
10/07/2007	12/07/2007	1	4.20	C.O. Low	
13/07/2007	14/07/2007	0	1.00	Other	
17/07/2007	22/07/2007	4	18.30	E. Low with front	
23/07/2007	30/07/2007	2	53.70	C.O. Low with front	
31/07/2007	02/08/2007	2	12.10	E. Low with front	
03/08/2007	04/08/2007	2	12.10	E. Low with front	
05/08/2007	08/08/2007	3	14.80	C.O. Low with front	
09/08/2007	14/08/2007	2	52.80	E. Low with front	
17/08/2007	20/08/2007	1	19.40	C.O. Low with front	
24/08/2007	02/09/2007	1	12.70	C.O. Low with front	
03/09/2007	10/09/2007	1	3.30	Other	
11/09/2007	13/09/2007	2	44.30	C.O. Low with front	
14/09/2007	16/09/2007	1	14.00	C.O. Low with front	
17/09/2007	19/09/2007	2	23.70	C.O. Low with front	
20/09/2007	22/09/2007	1	8.60	E. Low with front	
23/09/2007	03/10/2007	6	23.00	E. Low with front	
02/05/2008	05/05/2008	2	5.40	E. Low	
06/05/2008	08/05/2008	2	20.30	E. Low	
15/05/2008	17/05/2008	1	5.50	E. Low	
18/05/2008	20/05/2008	3	15.70	C.O. Low with front	
21/05/2008	22/05/2008	1	2.50	E. Low	
23/05/2008	29/05/2008	3	12.70	C.O. Low	
01/06/2008	06/06/2008	1	2.00	Other	Onshore flow from east
10/06/2008	12/06/2008	3	11.80	E. Low with front	
13/06/2008	16/06/2008	2	26.10	E. Low with front	
17/06/2008	21/06/2008	2	7.30	C.O. Low	
22/06/2008	23/06/2008	1	5.30	E. Low	
24/06/2008	25/06/2008	1	3.30	E. Low	
26/06/2008	28/06/2008	2	7.50	E. Low	
29/06/2008	04/07/2008	3	58.20	E. Low with front	
05/07/2008	10/07/2008	4	35.20	C.O. Low with front	
11/07/2008	13/07/2008	3	30.10	C.O. Low with front	
14/07/2008	15/07/2008	1	13.30	C.O. Low	
16/07/2008	17/07/2008	1	2.00	C.O. Low	

Continued on next page

Table A.1 – continued from previous page

Start Date	End Date	R. Days	Precip.	Classification	Comments
18/07/2008	20/07/2008	3	26.80	E. Low with front	
21/07/2008	24/07/2008	3	46.80	C.O. Low with front	
25/07/2008	31/07/2008	2	4.70	C.O. Low	
01/08/2008	03/08/2008	3	54.36	C.O. Low with front	
04/08/2008	07/08/2008	3	8.84	C.O. Low with front	
08/08/2008	09/08/2008	1	3.90	E. Low	
10/08/2008	12/08/2008	3	20.30	C.O. Low with front	
13/08/2008	14/08/2008	2	6.60	E. Low with front	
15/08/2008	18/08/2008	2	24.90	E. Low	
21/08/2008	24/08/2008	1	2.50	E. Low with front	
25/08/2008	02/09/2008	2	68.70	E. Low with front	
03/09/2008	05/09/2008	0	1.10	Other	
06/09/2008	09/09/2008	1	1.30	Other	ECL
10/09/2008	15/09/2008	1	29.00	E. Low with front	
16/09/2008	18/09/2008	2	29.10	E. Low with front	
19/09/2008	24/09/2008	1	71.50	E. Low with front	
25/09/2008	27/09/2008	1	1.50	E. Low	
01/05/2009	04/05/2009	1	3.50	E. Low	
14/05/2009	17/05/2009	2	51.70	E. Low with front	
25/05/2009	28/05/2009	2	6.10	C.O. Low with front	
31/05/2009	02/06/2009	0	1.00	Other	E. Dip
03/06/2009	06/06/2009	3	9.10	Other	E. Dip
07/06/2009	11/06/2009	5	49.10	C.O. Low	
12/06/2009	15/06/2009	2	6.70	Other	
16/06/2009	23/06/2009	1	4.20	E. Low	
24/06/2009	27/06/2009	3	10.10	C.O. Low	
28/06/2009	30/06/2009	2	19.70	C.O. Low	
01/07/2009	08/07/2009	5	137.00	E. Low with front	
09/07/2009	18/07/2009	4	36.20	C.O. Low with front	
19/07/2009	21/07/2009	1	1.60	E. Low	
22/07/2009	25/07/2009	2	39.30	C.O. Low with front	
26/07/2009	30/07/2009	2	11.70	E. Low	
31/07/2009	02/08/2009	1	17.60	E. Low	
03/08/2009	04/08/2009	1	7.60	E. Low	
05/08/2009	07/08/2009	2	5.60	E. Low	
08/08/2009	10/08/2009	2	15.00	E. Low with front	
11/08/2009	15/08/2009	4	21.20	C.O. Low	
16/08/2009	19/08/2009	2	18.30	E. Low with front	
20/08/2009	24/08/2009	4	79.70	E. Low with front	
25/08/2009	28/08/2009	3	29.40	E. Low with front	
29/08/2009	31/08/2009	3	56.90	C.O. Low with front	
01/09/2009	02/09/2009	1	23.00	E. Low	
03/09/2009	06/09/2009	1	16.00	C.O. Low with front	
07/09/2009	09/09/2009	3	35.90	C.O. Low with front	
10/09/2009	12/09/2009	1	10.50	Other	ECL
16/09/2009	19/09/2009	1	35.20	C.O. Low with front	
20/09/2009	21/09/2009	1	2.10	E. Low	
22/09/2009	25/09/2009	4	42.10	C.O. Low	
26/09/2009	02/10/2009	6	85.00	C.O. Low with front	

A.3 Conversion of ERA-Interim data to HYSPLIT-compatible format

Here are the python and shell scripts used in the conversion of ERA-Interim data to ARL packed data format. Various paths will have to be updated and the programs `wgrib` and `grib2arl` will have to be installed.

A.3.1 `makearl.py`

```
import os
import sys
from datetime import datetime, timedelta

# home=’/home/tchubb/’
home=’/nfs/1/home/tchubb/’

erai_archive=home+’erai/’
grib2arlexe=home+’local/hysplit4/data2arl/grib2arl’
# grib2arlexe=home+’local/hysplit4R/data2arl/grib2arl’
arl_archive=home+’erai-arl/’
wgribexe=home+’local/wgrib/wgrib’

ei_sfc_invfile=home+’erai/ei_oper_an_sfc_15x15_90N0E90S3585E_19890101’

def main(input,Debug=False,Clean=True):
    from numpy import array, sort

    cwd=os.getcwd()

    os.mkdir(arl_archive+input); os.chdir(arl_archive+input)

    yr=int(input[:4])
    mn=int(input[4:6])
    wk=int(input[-3:])

    datelist=makedatelist(yr,mn,wk)
    datelist=sort(datelist)

    try: gribfiles=findgribfiles(datelist[0],datelist[-1])
    except IndexError: gribfiles=[]

    for file in gribfiles:
sys.stdout.write("Including file: %s"%file+"\n")

    # Now ready to ungrib, so ensure tempgribfiles are empty
    i_file=’./ei_pl_’+input+’.grib’; s_file=’./ei_sfc_’+input+’.grib’;
    try:
os.remove(s_file)
    except OSError: pass
    try:
os.remove(i_file)
    except OSError: pass

    for d in datelist:
datestr=d.strftime("%Y%m%d%H")
```

```
sys.stdout.write("WALLTIME: %s\n"%datetime.now().strftime("%Y-%m-%d %H:%M:%S"))
pname,sname=ungrib(datestr,gribfiles,Debug=Debug)

sys.stdout.write(’cat ’+sname+’ >> ’+s_file+"\n")
os.system(’cat ’+sname+’ >> ’+s_file)
if Clean:
    sys.stdout.write(’rm ’+sname+"\n")
    os.remove(sname)

sys.stdout.write(’cat ’+pname+’ >> ’+i_file+"\n")
os.system(’cat ’+pname+’ >> ’+i_file)
if Clean:
    sys.stdout.write(’rm ’+pname+"\n")
    os.remove(pname)

sys.stdout.write("\n")

    # Now ready to pass resultant gribfiles to grib2arl
    grib2arl(i_file,s_file,ei_sfc_invfile,arlfile=arl_archive+input+’.arl’,Debug=Debug)

    # clean up
    if Clean:
for file in os.listdir(arl_archive+input):
    os.remove(file)
os.chdir(arl_archive)
os.rmdir(arl_archive+input)

    os.chdir(cwd)

def makedatelist(yr,mn,wk):
    from numpy import array
    maxdays=31
    while True:
try: return array([[datetime(yr,mn,d,h) for h in [0,6,12,18]] for d in range(1+(wk-1)*7,1+min(maxdays,wk*7))]
except ValueError: maxdays-=1

def findgribfiles(start_date,end_date,erai_archive=erai_archive):
    """Find ecmwf era-interim grib files which cover period between start and end date"""

    files=os.listdir(erai_archive)
    oneday=timedelta(1)
    f_out=[]

    for file in files:
if file[:10] == ’ei_oper_an’:
    f=file.split(’_’)
    try:
fsd=datetime.strptime(f[6],"%Y%m%d")
fed=datetime.strptime(f[7],"%Y%m%d")
    except IndexError:
fsd=None; fed=None

    if all([fsd,fed]):
if f[3]==’pl’ or f[3]==’sfc’:
    if ( (end_date>=fsd) and (start_date<(fed+oneday)) ):
f_out.append(file)

    return f_out

def ungrib(datestr,files,Debug=False):
    import subprocess
```

```
    oneday=timedelta(1)
    files_out=[]

    for file in files:
f=file.split('_')
fname=erai_archive+file
fsd=datetime.strptime(f[6],"%Y%m%d")
fed=datetime.strptime(f[7],"%Y%m%d")


frame=datetime.strptime(datestr,"%Y%m%d%H")

sys.stdout.write("\tGribfile start: %s"%fsd+"\n")
sys.stdout.write("\tGribfile end  : %s"%(fed+timedelta(0.75))+"\n")
sys.stdout.write("\tCurrent Frame : %s"%frame+"\n")

try:
    assert ( (frame>=fsd) and (frame<fed+oneday) )

    tmpname='./ei_'+f[3]+'_'+datestr+'.grib'
    strcommand=wgribexe+' -s -4yr '+ fname + ' | awk ' +"'"+'{d=substr($3,3)'+\
    ';if (d>='+datestr+' &&d<' +str(int(datestr)+1)+') print $0}'+"'"\
    +' FS='+"'"+':'+"'"+' | '+wgribexe+' -i '+ fname +' -s -grib -o '+\
    tmpname

    sys.stdout.write("%s"%strcommand+"\n")

    if Debug:
os.system('touch '+tmpname)
    else:
wgrib_process=subprocess.Popen(strcommand,\
shell='True',\
stdout=subprocess.PIPE,\
)
wgrib_output=wgrib_process.stdout.readlines()

wfid=open('./wgribout_'+datestr+f[3]+'.txt','w')
wfid.writelines(wgrib_output)

# os.system(strcommand)

except AssertionError:
    pass


    ## put some assertions here to make sure everything has gone fine
    sname='./ei_sfc_'+datestr+'.grib'
    pname='./ei_pl_'+datestr+'.grib'

    assert (os.path.isfile(sname)), ('File: %s does not exist!'%sname)
    assert (os.path.isfile(pname)), ('File: %s does not exist!'%pname)

    sys.stdout.write("Temporary gribfiles: %s, %s created\n"%(sname,pname))


    return pname,sname

def grib2arl(ifile, sfile, cfile,\
arlfile=None,\
clon='0',\
```

```
clat='-90',\
gproj='2',\
numpts='180',\
numlevs='25',\
sdef='1',\
Debug=False,\
Clean=True,\
):
    import subprocess

    strcommand=grib2arlexe+\
    " -i"+ifile+\
    " -s"+sfile+\
    " -c"+cfile+\
    " -g"+gproj+\
    " -n"+numpts+\
    " -k"+numlevs+\
    " -p"+sdef
    # " -x"+clon+\
    # " -y"+clat+\

    sys.stdout.write("%s"%strcommand+"\n")

    if Debug:
os.system('touch ./DATA.ARL')
os.system('touch ./MESSAGE')
    else:
grib2arl_process=subprocess.Popen(strcommand,\
    shell='True',\
    stdout=subprocess.PIPE,\
    )
grib2arl_output=grib2arl_process.stdout.readlines()
gfid=open('./grib2arlout.txt','w')
gfid.writelines(grib2arl_output)
# os.system(strcommand)

    assert (os.path.isfile('./DATA.ARL')), ("File: %s not created!"%"DATA.ARL")
    if arlfile is not None:
os.system("mv DATA.ARL "+arlfile)

    if Clean:
try:
    os.system("mv MESSAGE "+arlfile.rstrip('.arl')+'.msg')
    os.remove("ARLTIME")
    os.remove("CFG_ARL")
    os.remove("CFG_GRIB")
except OSError: pass



if __name__=="__main__":
    args=sys.argv

    if "--Clean" in args:
Clean=eval(args[args.index("--Clean")+1])
    else: Clean=True

    if "--Debug" in args:
Debug=args[args.index("--Debug")+1]
    else: Debug=False
```

```
    main(sys.argv[1],Debug=Debug,Clean=Clean)
```

A.3.2 Example shell script for execution of `makearl.py`

```
#!/bin/sh
#$ -S /bin/sh
#$ -l h_rt=23:59:00
#$ -cwd
source /etc/profile
module load python/2.5.1
yr=1990
mn=01
python /nfs/1/home/tchubb/pylib/makearl.py $yr$mn.001
python /nfs/1/home/tchubb/pylib/makearl.py $yr$mn.002
python /nfs/1/home/tchubb/pylib/makearl.py $yr$mn.003
python /nfs/1/home/tchubb/pylib/makearl.py $yr$mn.004
python /nfs/1/home/tchubb/pylib/makearl.py $yr$mn.005
```

A.4 Table of precipitation gauges used in chapter 6

Site name	Gauge type	Longitude	Latitude	Elevation
Tooma Dam	ETI	148.28	-36.05	1222
Ramshead	ETIH	148.28	-36.51	1903
The Kerries	ETI	148.38	-36.26	1741
Grey Hill	ETI	148.28	-36.29	1624
Jagungal	HTB	148.39	-36.14	1669
Whites River	ETIH	148.39	-36.30	1709
Tantangara Dam	TB	148.65	-35.80	1237
North Bulls Peak	ETIH	148.43	-36.18	1805
Whites River	ETI	148.39	-36.30	1709
Charlotte Pass	ETI	148.34	-36.43	1758
Tantangara Reservoir	TB	148.57	-35.77	1250
Perisher	ETIH	148.41	-36.41	1744
Bald Hill RS	ETI	148.57	-36.06	1652
Island Bend	ETI	148.48	-36.31	1222
Snowy Plain	ETIH	148.55	-36.19	1368
Mount Hudson	ETIH	148.55	-36.11	1754
Thredbo	ETI	148.31	-36.50	1348
Guthega Dam	ETIH	148.37	-36.38	1586
Snowy Plain	ETI	148.55	-36.19	1368
Guthega PS	HTB	148.41	-36.35	1321
Pinnacle Mountain	ETI	148.26	-36.32	1535
Anderson	ETIH	148.34	-36.36	1818
Mount Hudson	ETI	148.55	-36.11	1754
Perisher	ETI	148.41	-36.41	1744
The Kerries	ETIH	148.38	-36.26	1741
Cabramurra	HTB	148.39	-35.94	1473
Brownleys Back Creek	TB	148.46	-36.35	1095
Geehi Dam	TB	148.31	-36.30	1161
Spencers Creek	ETIH	148.35	-36.43	1763
Murray 1 Valve House	ETI	148.21	-36.25	993
Grey Hill	ETIH	148.28	-36.29	1624
Ramshead	ETI	148.28	-36.51	1903
North Bulls Peak	ETI	148.43	-36.18	1805

Table A.2: Table of all precipitation gauges used in chapter 6. The abbreviations are: ETI, a weighing-type precipitation gauge; ETIH, a weighing type gauge installed in a wind fence; HTB, a heated tipping bucket gauge; and TB, a tipping bucket gauge.

A.5 Trajectory difference plots for other selection criteria

As discussed in chapter 5, trajectories were selected to form the difference plots on a number of criteria. The biggest difference was found based on when trajectories arriving during months with positive/negative SAM were separated, but results for the other criteria are presented here (see captions).

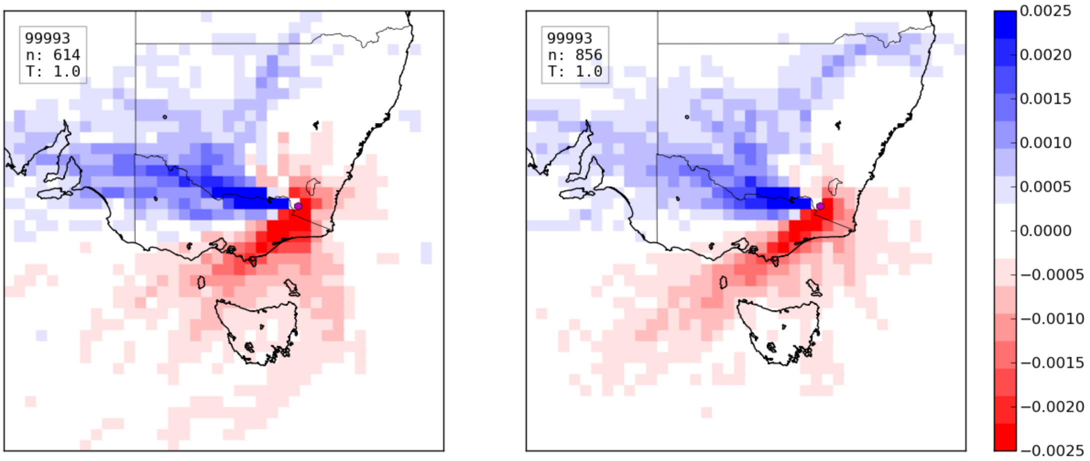

Figure A.2: As for figure 5.4, except for trajectories arriving in four years with negative (left) and positive (right) SOI index.

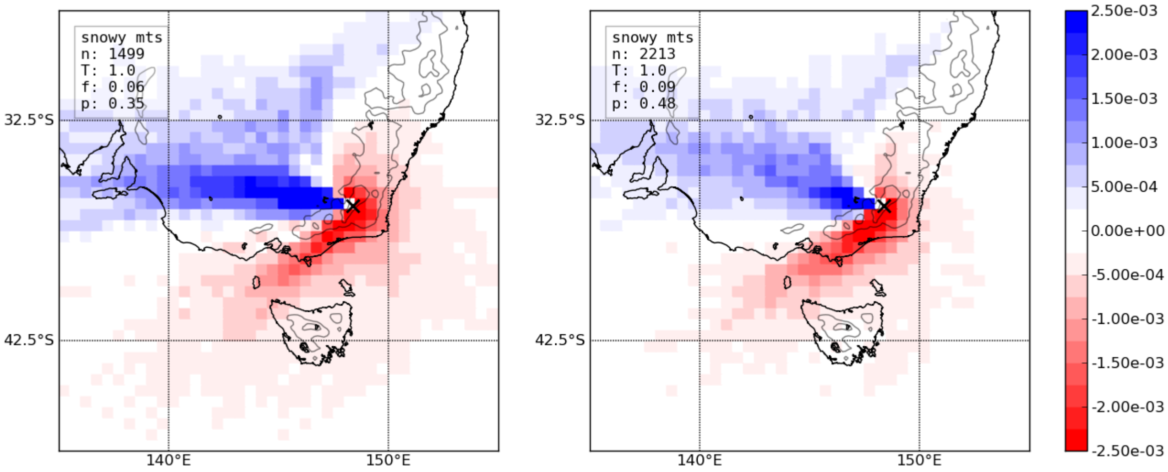

Figure A.3: As for figure 5.4, except for trajectories associated with embedded (left) and cut-off (right) lows.

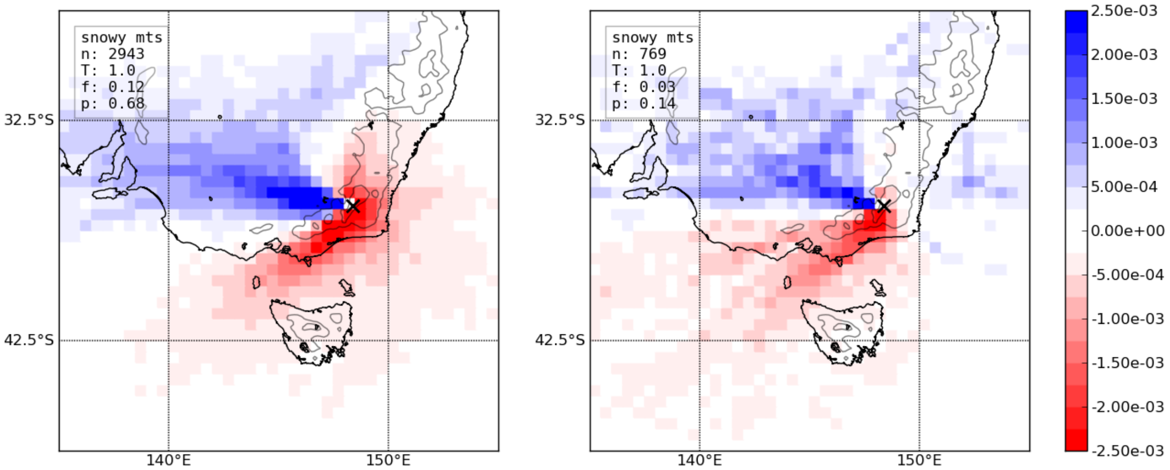

Figure A.4: As for figure 5.4, except for trajectories associated with frontal (left) and non-frontal (right) synoptic systems.

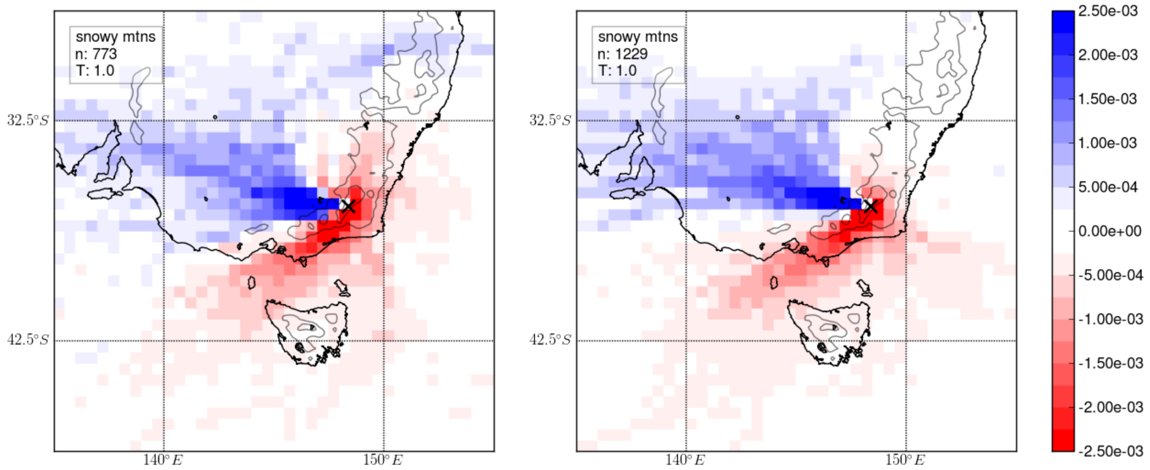

Figure A.5: As for figure 5.4, except for trajectories arriving in five driest (left) and wettest (right) years.

A.6 $\Delta\widetilde{r_e}$ for specific pollution sites when source region size is varied

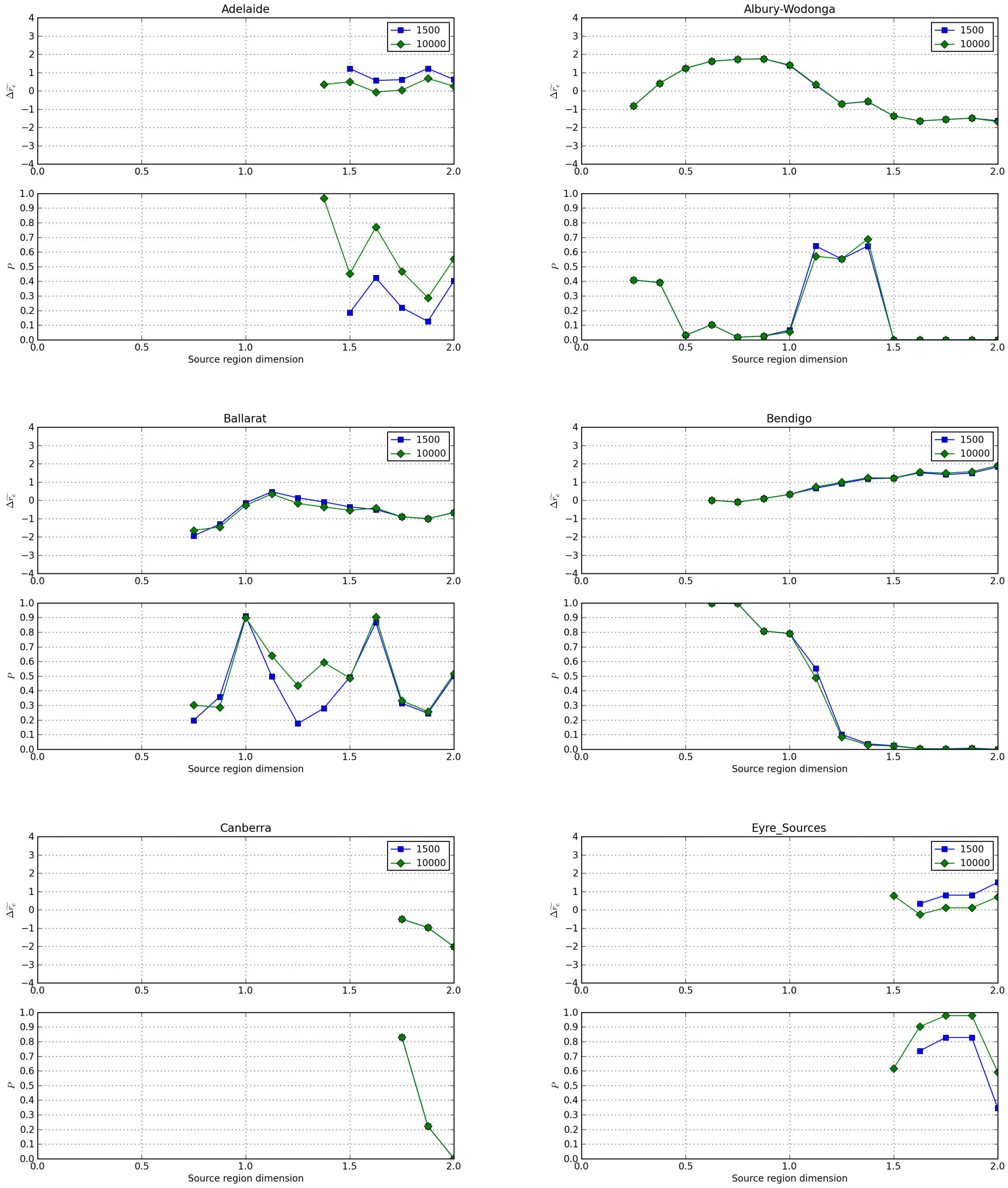

Figure A.6: As for figure 6.12, but for a selection of sites. Note that at least 25 retrievals were required to make an assessment of the impact for each source/nearby combination.

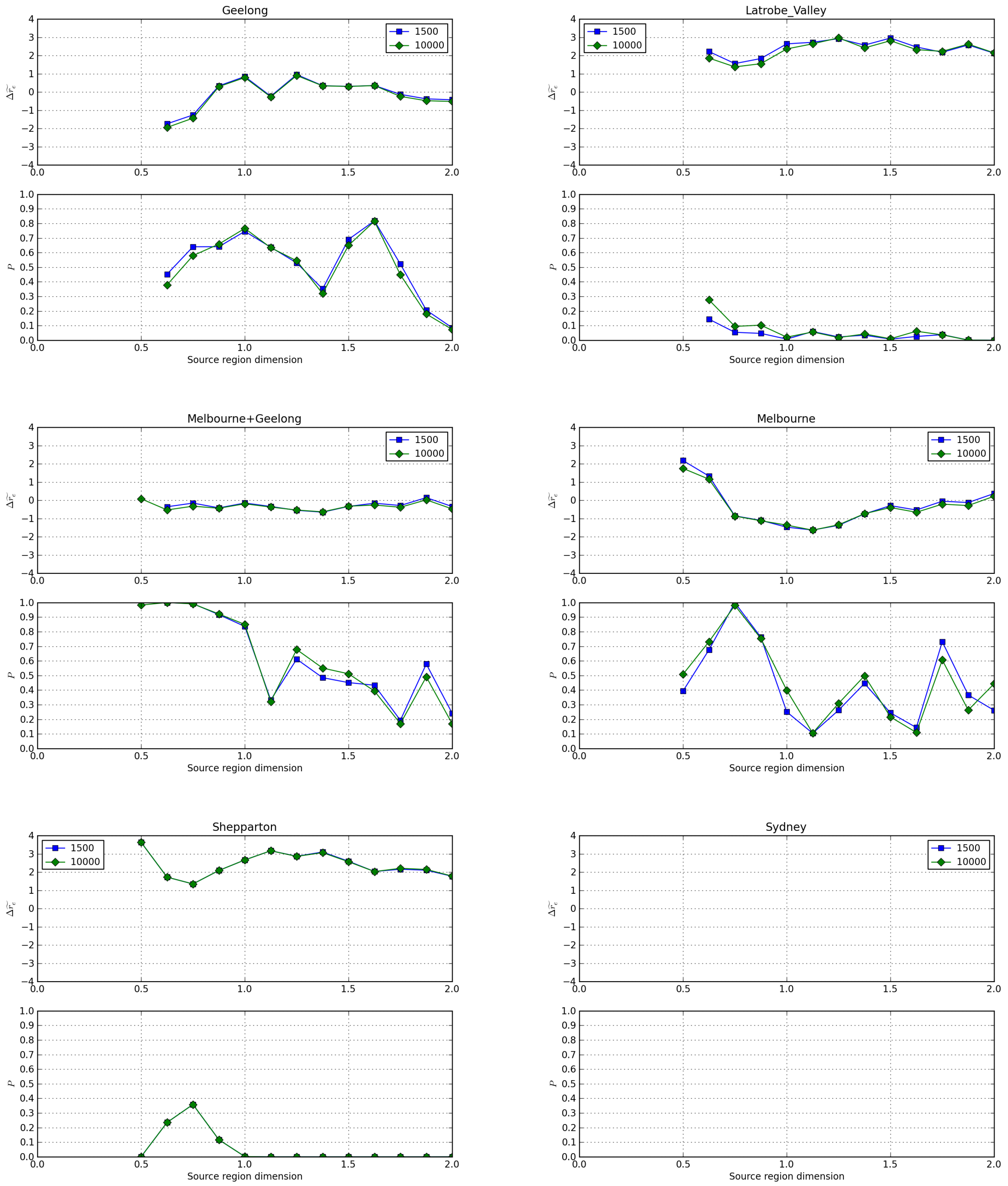

Figure A.7: As for figure 6.12, but for a selection of sites (continued).

A.7 ΔP_{sn} for specific pollution sites when source region size is varied

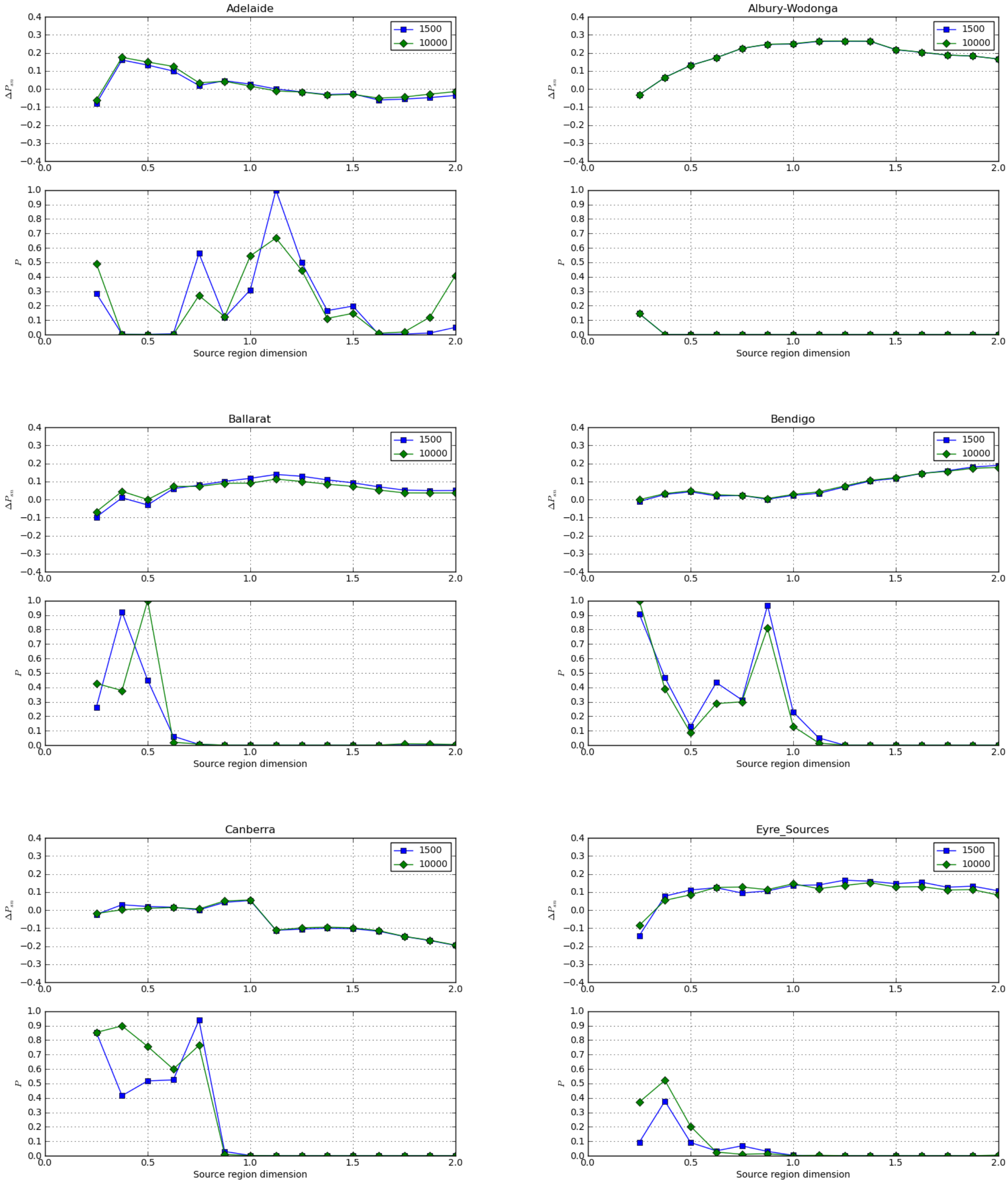

Figure A.8: As for figure A.6, but for the statistic ΔP_{sn}.

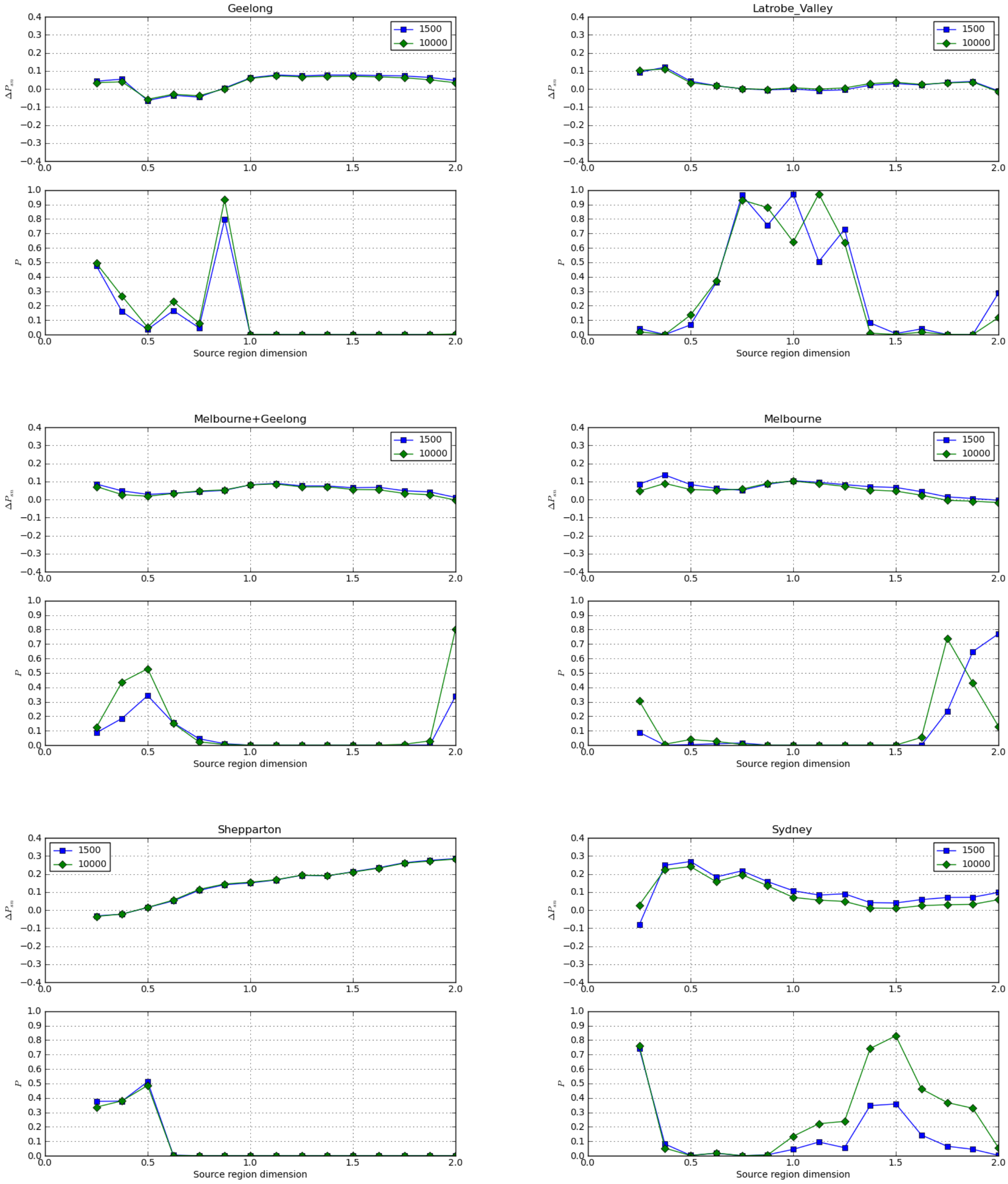

Figure A.9: As for figure A.6, but for the statistic ΔP_{sn} (continued).

A.8 $\Delta\widetilde{R}_{sn}$ for specific pollution sites when source region size is varied

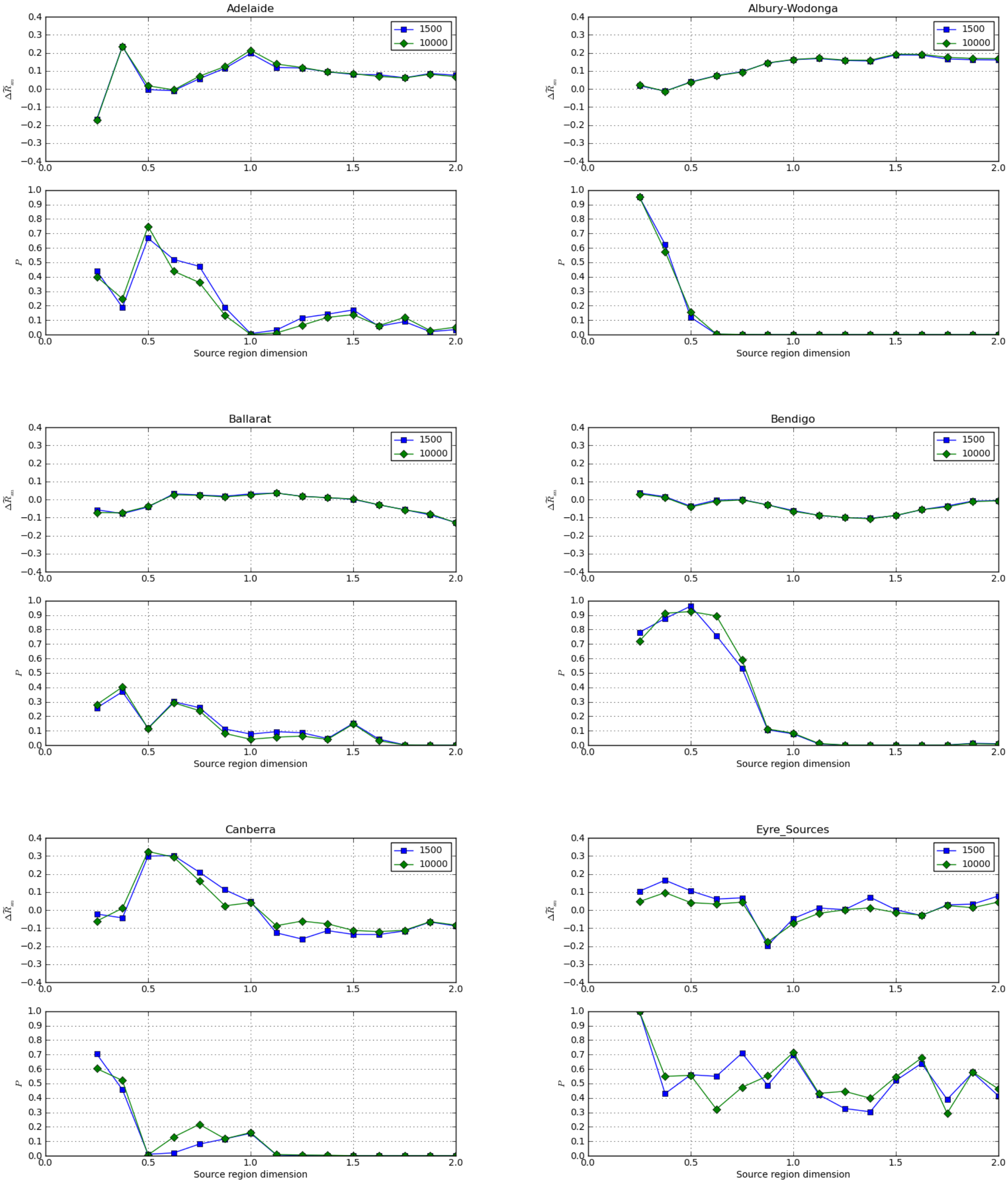

Figure A.10: As for figure A.6, but for the statistic $\Delta\widetilde{R}_{sn}$

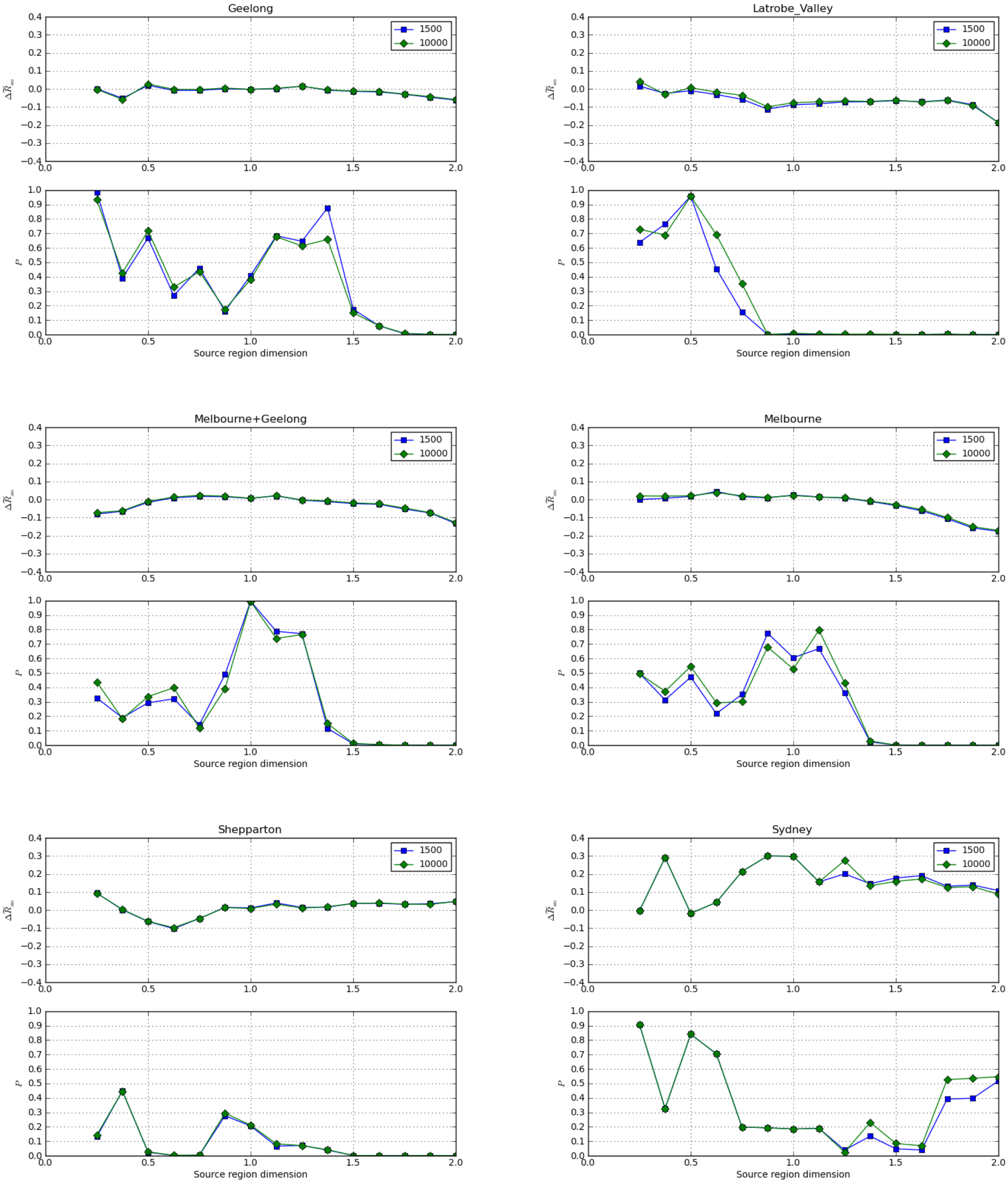

Figure A.11: As for figure A.6, but for the statistic $\Delta\widetilde{R}_{sn}$ (continued).